

Kinetics and Mechanism of Ozone Decomposition and
Oxidation of Ethanol on Manganese Oxide Catalysts

Wei Li

Dissertation submitted to the Faculty of the
Virginia Polytechnic Institute and State University
in partial fulfillment of the requirements for the degree of

DOCTOR OF PHILOSOPHY

in

Materials Engineering and Science

Dr. S. Ted Oyama, Chair

Dr. Robert J. Bodnar

Dr. David F. Cox

Dr. Seshu Desu

Dr. Gerald V. Gibbs

Dr. Joseph S. Merola

May 28, 1998

Blacksburg, Virginia

Keywords: Ozone, Kinetics, Mechanism, Decomposition, Ethanol Oxidation, Raman
Spectroscopy, Manganese Oxides

Copyright 1998, Wei Li

Kinetics and Mechanism of Ozone Decomposition and Oxidation of Ethanol on Manganese Oxide Catalysts

Wei Li

(Abstract)

Understanding and establishing reaction mechanisms is an important area in heterogeneous catalysis. This dissertation describes the use of *in situ* laser Raman spectroscopy combined with kinetic measurements and dynamic experiments to determine the mechanism of catalytic reactions. Two cases involving ozone reactions on manganese oxide catalysts were treated. Manganese oxide was chosen because it is the most active of the transition metal oxides for ozone decomposition and because it is a well-known catalyst for complete oxidation reactions.

The first case studied was that of the ozone decomposition reaction on a supported manganese oxide catalyst. An adsorbed species with a Raman signal at 884 cm^{-1} was observed and assigned to a peroxide species based on results of *in situ* Raman spectroscopy, ^{18}O isotopic substitution measurements, and *ab initio* MO calculations. The reaction pathway of ozone decomposition was elucidated with carefully designed isotopic experiments. The reaction sequence was found to involve two irreversible, kinetically significant steps: 1) dissociative adsorption of ozone to form a peroxide species and an atomic oxygen species, and 2) desorption of the peroxide intermediate. The kinetic behavior of the peroxide species and the overall decomposition reaction were investigated to test the validity of the proposed sequence. The transient kinetics were found to be consistent with the steady state kinetics, and both were well represented by the two-step sequence, indicating that the proposed reaction sequence accurately described the mechanism of decomposition. The surface was found to be non-uniform, with activation energies that varied linearly with coverage. At zero surface coverage the activation energy for ozone adsorption was found to be 6.2 kJ mol^{-1} , while that for desorption of the peroxide species was found to be 69.0 kJ mol^{-1} .

The second case investigated was that of ethanol oxidation using ozone on alumina and silica supported manganese oxide catalysts. Ethanol was found to react with ozone at lower temperatures than with oxygen, and also with a lower activation energy. The reaction kinetics was found to be well described by a power law equation with the reaction orders on ozone and ethanol being 0.89 and 0.81 respectively. The oxidation reactivity was found to be closely related to that of ozone decomposition, suggesting an important role of ozone decomposition in the reaction mechanism. *In situ* laser Raman spectroscopic studies showed the existence of adsorbed ethoxide species on the catalyst surface under reaction conditions, however, at a much lower concentration than when oxygen alone was used as the oxidant. Transient experiments provided direct evidence that surface peroxide (an adsorbed species due to ozone) and surface ethoxide (an adsorbed species due to ethanol) reacted with each other on the catalyst surface.

Acknowledgements

During the last four years, I have been fortunate to work with the Environmental Catalysis and Materials Laboratory in the Department of Chemical Engineering at Virginia Polytechnic Institute and State University. The collaborative and friendly environment of the group has greatly contributed to my professional growth both in studies and research. I would thank all the group members, in particular, Balamurugan Dhandapani, Weimin Zhang, Todd St. Clair, Rakesh Radhakrishanan, Anil Prahbu, Paul Clark, Sasangan Ramanathan, Tim Hendricks, Patrick Bolton, and Viviane Schwartz, for their helpful and stimulating discussions.

I would like to express my deep gratitude and thankfulness to my advisor and committee chair, Dr. S. Ted Oyama. Since my very first days at Virginia Tech, he has been a source of guidance, support and inspiration. No matter what kind of problem was discussed, his advice and encouragement always provided new perspectives. The expertise that he shared with me will certainly remain a tremendous resource for my academic career. I am very thankful for everything he has done for me.

Also, I am deeply indebted to the other members of my committee: Dr. Robert J. Bodnar, Dr. David F. Cox, Dr. Seshu Desu, Dr. Gerald V. Gibbs, and Dr. Joseph S. Merola. Their expertise and assistance played an important role in the progress of my research. I appreciate all their time and effort. In particular, I am grateful to Dr. Gibbs for introducing me to the field of theoretical calculations and also helping me with the calculations work in this dissertation. This area is certainly going to be a field of my future research interest.

Financial support for this research project was provided by the Director, Division of Chemical and Thermal Systems of the National Science Foundation, under Grant CTS-9712047.

This work would not be accomplished without the two most precious persons in my life. Their everyday patience, love, and understanding are the driving force for all my achievements. Expressing my deepest love to my son Yuping and my wife Wenye, I dedicate this work to them.

Table of Content

Chapter 1. Background.....	1
1.1 Introduction.....	1
1.2. Literature Review	2
1.2.1. General Properties of Ozone'	2
1.2.2. Ozone Adsorption	2
1.2.3. Ozone Decomposition.....	4
1.2.4. Ozone as an Oxidant	6
1.3. Objectives and Approach of This work.....	9
1.3.1. Objectives.....	9
1.3.2. Approach of This Work	11
Chapter 2. <i>In Situ</i> Laser Raman Studies of Ozone Decomposition.....	13
2.1. Introduction.....	13
2.2. Experimental Section and Computational Details.....	15
2.2.1. Catalyst Preparation	15
2.2.2. In Situ Laser Raman Spectroscopy.....	15
2.2.3. Calculation Details.....	17
2.3. Results.....	18
2.3.1. Raman Spectra of Adsorbed Species	18
2.3.2. Isotopic Substitution	19
2.3.3. Ab Initio Calculations of Model Mn Compounds	22
2.3.4. Temperature Programmed Desorption (TPD) of Ozone.....	25
2.4. Discussion	26
2.4.1. Raman Spectra of the Adsorbed Species.....	26
2.4.2. Assignment of the Adsorbed Species.....	27
2.4.2.1. Isotopic Substitution Experiments	27
2.4.2.2. <i>Ab Initio</i> Calculations of Model Mn Compounds.....	29
2.4.2.3. Manganese Peroxide Complexes	29

2.4.3. Reaction Pathways	30
2.5. Conclusions	32
Chapter 3. Kinetic Studies of Ozone Decomposition	33
3.1. Introduction	33
3.2. Experimental Section	34
3.3. Results	35
3.3.1. Effect of Laser	35
3.3.2. Steady State Kinetics	35
3.3.3. Transient Kinetics	38
3.4. Discussion	41
3.4.1. Steady State Kinetics	41
3.4.1.1. Uniform Surface Kinetic Analysis	42
3.4.1.2. Non-Uniform Surface Kinetic Analysis	43
3.4.2. Transient Kinetics	47
3.5. Conclusions	52
Chapter 4. Ethanol Oxidation Using Ozone	54
4.1. INTRODUCTION	54
4.2. EXPERIMENTAL	55
4.2.1. Catalyst Preparation and Characterization	55
4.2.2. In Situ Laser Raman Spectroscopy	55
4.3. RESULTS	57
4.3.1. Catalyst Characterization	57
4.3.2. Ethanol Oxidation Reactivity	58
4.3.3. In Situ Laser Raman Spectroscopic Studies	61
4.3.4. Ozone Decomposition	62
4.3.5. Kinetic Measurements	64
4.4. DISCUSSION	64
4.4.1. Reaction Stoichiometry	64

4.4.2. In Situ Laser Raman Spectroscopic Studies.....	65
4.4.3. Role of Ozone Decomposition.....	66
4.5. CONCLUSIONS	67
Chapter 5. Recommendations for Future Work	68
Appendix A. <i>Ab Initio</i> MO Calculation Results	71
a.1. Output File for the model compound $\text{Mn}(\text{O}_2)(\text{OH})_4^+$	71
Appendix B. Entropy Calculation for the Peroxide Species	87
B.1. Translational Entropy.....	87
B.2. Rotational Entropy.....	87
Appendix C. Steady State and Transient Kinetic Results for Ozone Decomposition	89
Appendix D. Least Square Fitting of the Steady State Ozone Decomposition Kinetics Using the Non-Uniform surface Treatment.....	97
Appendix E. Kinetic Data for Ethanol Oxidation Using Ozone	102
Appendix F. Least Square Fitting Of Ethanol Oxidation Kinetic Data	106
F.1. Fitting Procedure.....	106
Results	111
Vita	112

List of Figures

Figure 1.1. Resonance Structures of Ozone	2
Figure 2.1. Schematic of set-up for the <i>in situ</i> laser Raman experiments.....	16
Figure 2.2. Schematic of the set-up for the isotopic substitution experiments.....	17
Figure 2.3. <i>In situ</i> Raman spectra of the catalyst sample	19
Figure 2.4. <i>In situ</i> Raman spectra of the catalyst sample at various temperatures in a 2 mol% ozone/oxygen mixture.....	20
Figure 2.5. <i>In situ</i> Raman spectra of unexchanged sample after ozone adsorption.....	21
Figure 2.6. <i>In situ</i> Raman spectra of ¹⁸ O-exchanged sample after ozone adsorption.....	22
Figure 2.7. <i>In situ</i> Raman spectra of the catalyst sample in a mixture of ¹⁶ O ₃ / ¹⁶ O ₂ and ¹⁸ O ₃ / ¹⁸ O ₂	23
Figure 2.8. <i>In situ</i> Raman spectra of the catalyst sample after a sequential adsorption of ozone isotopes	24
Figure 2.9. Optimized structure of manganese model compounds.....	25
Figure 2.10. TPD profiles of O ₂ signals after O ₂ and O ₃ adsorption.....	27
Figure 3.1. Effects of laser power and sample spin rate on the Raman signal intensity of the observed peroxide species.....	38
Figure 3.2. Effects of temperature and ozone partial pressure on ozone decomposition rate.	39
Figure 3.3. Reaction isotherms of the ozone decomposition reaction measured using <i>in situ</i> laser Raman spectroscopy	40
Figure 3.4. Clausius-Clapeyron plots of the coverage data.....	41
Figure 3.5. Dependence of isosteric heat of reaction on the surface coverage.....	42
Figure 3.6. A typical set of Raman signals for a transient adsorption experiment (inset) and the corresponding adsorption curve.....	42
Figure 3.7. (a) Effect of temperature on the transient adsorption curve. (b) Effect of ozone partial pressure on the transient adsorption curve.	44
Figure 3.8. Effect of temperature on the transient desorption curve.....	45
Figure 3.9. Plots of reaction rate versus surface coverage	47
Figure 3.10. Plots of surface coverage versus the logarithm of ozone partial pressure.....	49

Figure 3.11. Calculation of adsorption and desorption rates from the transient results.....	52
Figure 3.12. Transient adsorption and desorption rates versus surface coverage.....	53
Figure 3.13. Arrhenius plots of k_d values calculated from the steady state and transient desorption results.....	56
Figure 3.14. Comparison of measured steady state reaction rates (symbols) with the calculated curves (solid lines) using the kinetic parameters derived from the transient desorption data.....	57
Figure 3.15. Comparison of measured transient desorption curves (symbols) with the calculated curves from the steady state kinetic parameters (solid lines).....	58
Figure 4.1. Schematic of the <i>in situ</i> laser Raman system for ethanol oxidation.....	62
Figure 4.2. XRD patterns of the supported MnO ₂ catalysts and the supports.....	64
Figure 4.3. Ethanol oxidation reactivity using O ₃ or O ₂ on 10% MnO ₂ /Al ₂ O ₃	65
Figure 4.4. Ethanol oxidation reactivity using O ₃ or O ₂ on 10% MnO ₂ /SiO ₂	66
Figure 4.5. Converted ozone to ethanol ratio on the supported MnO ₂ catalysts	67
Figure 4.6. Arrhenius plots of the turnover rate of ethanol oxidation on MnO ₂ /Al ₂ O ₃	67
Figure 4.7. Raman spectra of 10% MnO ₂ /Al ₂ O ₃ sample under various conditions (a. oxygen; b. ozone; c. ethanol; d. ethanol and ozone).....	68
Figure 4.8. Transient experiment Raman spectra on 10% MnO ₂ /Al ₂ O ₃	69
Figure 4.9. Ozone decomposition reactivity on supported MnO ₂ catalysts	70
Figure 4.10. Arrhenius plots of turnover rate of ozone decomposition on MnO ₂ /Al ₂ O ₃	71
Figure 5.1. Proposed catalytic cycle of ozone decomposition on a catalyst with manganese pairs as active centers	77

List of Tables

Table 1.1. Reported Catalytic Oxidation Reactions Using Ozone as an Oxidant	6
Table 2.1. Calculated Vibrational Frequencies of ^{18}O -substituted $\text{Mn}(\text{OH})_4(\text{O}_2)^+$	25
Table 2.2. Calculated Vibrational Frequencies of ^{18}O -substituted $\text{MnO}_3(\text{OH})$	26
Table 2.3. Isotopic Shifts ($\text{O}^{18}/\text{O}^{16}$) of Various Species.....	30
Table 3.1. Kinetic Parameters of the Non-Uniform Surface Analysis.....	49
Table 3.2. Comparison of the Steady-State Coverage Obtained from Transient and Steady-State Experiments	55
Table C.1. Transient Data of the Ozone Decomposition Reaction.....	97
Table C.2. Steady State Kinetic Data of the Ozone Decomposition Reaction.....	102
Table F.1. Calculation Details for the Least Square Fitting of the Ethanol Oxidation Kinetic Data.....	116
Table G.1. An example Data Set for Ozone Decomposition.....	118

CHAPTER 1. BACKGROUND

1.1 INTRODUCTION

One of the most fundamental and probably most challenging issues in heterogeneous catalysis is the establishment of reaction mechanisms. It is an essential step towards the ultimate goal of rational design of catalysts¹, yet, its implementation requires thorough knowledge of the reaction system, including information on the elementary steps at molecular level. Often knowledge of the global reaction kinetics is necessary, but not sufficient to pinpoint a mechanism. In this dissertation an investigation of catalytic mechanism, which combines *in situ* spectroscopic experiments (both qualitative and quantitative) with steady state and transient kinetic measurements, will be described. Application will be made on ozone reactions on manganese oxide. An example of this approach for the ozone decomposition will be presented in Chapters 2 and 3. Chapter 2 will cover the identification of reaction intermediates using *in situ* laser Raman spectroscopy, isotopic substitution, and theoretical calculations, while Chapter 3 will describe elucidation of the reaction sequence from measurements of steady state and transient kinetics. Chapter 4 will present a mechanistic study of another ozone reaction, oxidation of ethanol, using *in situ* laser Raman spectroscopy and kinetic measurements. Some recommendations for future work will be discussed in Chapter 5.

In this chapter a summary of the existing literature on catalytic ozone reactions will be given with emphasis placed on studies involving kinetics and mechanisms. This is not intended as an exhaustive collection of research results, rather, it is meant to describe the state of the art of research work in this area, and to point out the motivations for this work.

This chapter is organized as follows. First, a brief background on the general properties of ozone will be presented. Second, work on ozone adsorption and decomposition reaction will be reviewed. Third, experimental results on using ozone as an oxidant will be surveyed.

¹ Burwell, R. L. in *Catalysis: Science and Technology*, Anderson, J. R. and Boudart, M. (Eds), 9, 1-85, Springer, Berlin, **1991**.

Finally, the motivations and objectives of this dissertation will be addressed and our approach in this work will be discussed.

1.2. LITERATURE REVIEW

1.2.1. General Properties of Ozone^{2,3}

Ozone is the triatomic allotrope of oxygen. It is diamagnetic with C_{2v} symmetry and has a low dipole moment of $1.77 \times 10^{-30} \text{ C}\cdot\text{m}$ (0.53 D). It has a bent structure with a bond angle of $116^\circ 49'$ and equal oxygen-oxygen bond distances of 0.128 nm. This bond length is intermediate between that of a single and double oxygen bond, corresponding to a bond order of 1.7. The structure of ozone can be viewed as a hybrid of resonance structures (Figure 1.1). In (1) and (4) there is a positively charged terminal oxygen with only six electrons, which accounts for the electrophilic nature of ozone. Hence the active site for electrophilic attack by ozone will be at one of the terminal oxygen atoms rather than the center oxygen atom.

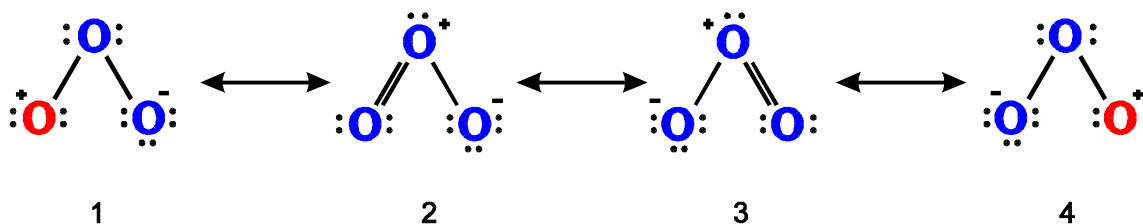


Figure 1.1. Resonance Structures of Ozone

1.2.2. Ozone Adsorption

Investigations on ozone adsorption have been very limited and can basically be separated into two groups: studies on matrix-isolated ozone species mainly by Andrews and co-workers⁴⁻⁷, and studies on low temperature ozone adsorption on oxides by Lavalley and co-workers⁸⁻¹¹.

² Wojtowicz, J. A., "Ozone", in *Kirk-Othmer, Encyclopedia Chem.-Technol.* 4th Ed. John Wiley, **1996**, Vol. 17, p. 953.

³ Ullmann's Encyclopedia of Industrial Chemistry, **1991**, Vol. A18, 349.

⁴ Spiker, R. C.; Andrews, L. *J. Chem. Phys.* **1973**, 59, 1851-1862.

The work by Andrews and coworkers concentrated on identification and characterization of the species formed from matrix-isolation reactions between ozone and alkali and alkali earth metals. The infrared and resonance Raman spectra of the matrix reaction products of ozone with various metals were very similar. The infrared spectra showed very intense bands near 800 cm^{-1} and weaker bands near 600 cm^{-1} which were assigned to the ν_3 and ν_2 bands of the ozonide ion O_3^- according to their oxygen isotopic shifts⁴. The ozonide species was proposed to be symmetrically bound to the metal cations in a C_{2v} structure. The resonance Raman spectra of the matrix reaction products consisted of a strong fundamental near 1010 cm^{-1} for the alkali metals⁵ (1020 cm^{-1} for the alkali earth metals⁷) and a regular progression of overtones with decreasing intensity. This fundamental was assigned to ν_1 of the ozonide ion in the M^+O_3^- species. Similar results were also reported on polycrystalline KO_3 and CsO_3 samples^{12,13}.

Lavalley and coworkers studied ozone adsorption at 77 K on a series of oxides using Fourier-transform infrared (FT-IR) spectroscopy⁸⁻¹¹. On SiO_2 ⁸, TiO_2 ⁹, Al_2O_3 , ZrO_2 , MgO , and CeO_2 ¹⁰, ozone was found to form hydrogen bonds with the surface OH groups via one of the terminal oxygen atoms. The authors proposed that the ozone molecule acted as a Lewis base, adsorbing on weaker Lewis acid sites to form a coordination complex and decomposing on the stronger sites of TiO_2 , Al_2O_3 , or ZnO to form atomic oxygen. This interpretation was also supported by the experimental results that preadsorbed acetonitrile or pyridine considerably decreased the amount of strongly bonded O_3 species and significantly inhibited ozone decomposition.

⁵ Spiker, R. C.; Andrews, L. *J. Chem. Phys.* **1973**, *59*, 1863-1871.

⁶ Andrews, L.; Spiker, R. C. *J. Phys. Chem.* **1972**, *57*, 51.

⁷ Ault, B.; Andrews, L. *J. Mol. Spectrosc.* **1977**, *62*, 437-445.

⁸ Bulanin, K. M.; Alexeev, A. V.; Bystrov, D. S.; Lavalley, J. C.; Tsyganenko, A. A. *J. Phys. Chem.* **1994**, *98*, 5100-5103.

⁹ Bulanin, K. M.; Lavalley, J. C.; Tsyganenko, A. A. *J. Phys. Chem.* **1995**, *99*, 10294-10298.

¹⁰ Bulanin, K. M.; Lavalley, J. C.; Tsyganenko, A. A. *Coll. Surf.* **1995**, *101*, 153-158.

¹¹ Bulanin, K. M.; Lavalley, J. C.; Tsyganenko, A. A. *J. Phys. Chem.* **1997**, *101*, 2917-2922.

¹² Karalin, A. I.; Rosolovsky, V. Y.; Tokareva, C. A.; Vol'nov, I. I. *Dokl. Akad. Nauk SSSR Ser. Fiz. Khim.* **1972**, *206*, 641.

¹³ Bates, J. B.; Brooler, M. H.; Boyd, G. E. *Chem. Phys. Lett.* **1972**, *76*, 3208.

However, this interpretation of ozone as a Lewis base is in conflict with the common belief that ozone is in fact a Lewis acid owing to its strong electrophilic nature. It can also be argued that ozone actually acts as a Lewis acid and the hydroxyl groups on the oxide surfaces act as Lewis bases. The fact that ozone interacts with the hydroxyl group through one of its terminal oxygen atoms is also in agreement with the discussion earlier on its resonance structure, in support of the interpretation that ozone acts as a Lewis acid. Evidently more experimental evidence is needed to ascertain the nature of the interaction between ozone and oxide surfaces.

Recently the same authors also reported a study on CaO^{11} , in which they observed a signal at 812 cm^{-1} in addition to the signals of the molecularly adsorbed ozone. This signal was assigned to an ozonide (O_3^-) species following isotopic substitution experiments. This observation clearly demonstrates that ozone acts as a Lewis acid causing electron transfer from OH groups to ozone.

A significant drawback of the above-mentioned studies is that they were carried out at very low temperatures while commercially interesting reactions (ozone decomposition or oxidation reactions using ozone as an oxidant) occur at room temperature and above. It is therefore unlikely that the same species observed at low temperatures will exist and participate under “real” reaction conditions. In fact it was reported that the ozonide species formed at low temperatures ($< 77\text{ K}$) disappeared quickly at elevated temperatures. Hence it is imperative that identification and characterization of the adsorbed species of ozone should be carried out *in situ* to accurately describe the species formed and the way it interacts with solid surfaces.

1.2.3. Ozone Decomposition

Ozone is thermodynamically unstable and spontaneously decomposes to diatomic oxygen. The standard free energy of reaction is $\Delta G_{298}^0 = -163\text{ kJ mol}^{-1}(\text{O}_3)$. However, the thermal decomposition is kinetically slow at temperatures up to 523 K^2 , resulting in a need for catalysts to decompose it at lower temperatures.

The problem of catalytic ozone decomposition is important because ozone is commonly found or generated in human environments (aircraft cabins, offices with photocopiers, laser

printers, or sterilizers), and because it is extremely toxic. According to EPA's new Air Standards, the threshold level for allowable exposure during an 8 h time period is 0.08 ppm¹⁴. Ozone is also receiving attention as a replacement for chlorine in the paper and pulp industry and in municipal water purification. In all instances where ozone is generated or used in office or industrial applications there is a need to destroy it after use. A large number of patents have been devoted to designing catalyst filters for ozone decomposition, and the catalysts used have been recently reviewed¹⁵.

However, kinetic and mechanistic studies of ozone decomposition on catalysts have been scarce. A study on a manganese oxide catalyst reported a reaction order of 0.68 for ozone, and zero order for oxygen and H₂O¹⁶. A reaction mechanism involving a negatively charged diatomic oxygen intermediate was proposed. A study on TiO₂ also found a zero order dependency on H₂O. However, other studies on MnO₂ found a first order dependence on ozone³⁷. Hence a thorough study of its kinetics is necessary.

Attempts were made to observe reaction intermediates of ozone decomposition spectroscopically, in particular, using electron paramagnetic spectroscopy (EPR). On a silver oxide catalyst¹⁷, Imamura, *et al.* suggested that negatively charged oxygen species were formed upon the introduction of ozone. Although a superoxide species was detected at 75 K by EPR, its role in the ozone decomposition reaction was not clearly determined. Naydenov, *et al.*¹⁸ identified an O₃⁻ species on a CeO₂ surface using EPR, however, they found that this species was not involved in the reaction. It was suggested that a highly reactive atomic oxygen species (probably O[·]) might be the intermediate. The use of EPR limits the implementation of *in situ* methods and also excludes the detection of diamagnetic species such as O₂²⁻. Obviously research work in this area should attempt to use spectroscopic techniques that can be carried out *in situ* and that can detect as many species as possible.

¹⁴ *Chem. Eng. News* **1997**, April 14.

¹⁵ Dhandapani, B.; Oyama, S. T. *Appl. Catal. B* **1997**, *11*, 129-166.

¹⁶ Dhandapani, B.; Oyama, S. T. *Chem. Lett.* **1995**, 413-414.

¹⁷ Imamura, S.; Ikebata, M.; Ito, T.; Ogita, T. *Ind. Eng. Chem. Res.* **1991**, *30*, 217.

¹⁸ Naydenov, A.; Stoyanova, R.; Mehandjiev, D. *J. Molec. Catal. A.* **1995**, *98*, 9.

1.2.4. Ozone as an Oxidant

Ozone is a powerful oxidant, and has been widely used in organic synthesis^{19,20}. An extensive literature exists on ozone reactions with organic molecules in the gas phase^{21,22}, and liquid phase²³. However, much less is known about the oxidizing ability of ozone towards organic molecules on solid surfaces. Recent interest in catalytic removal of volatile organic compounds (VOCs) has triggered considerable effort on employing ozone as the oxidant and it has emerged as a promising alternative because of advances in ozone generation equipment and catalyst development. However, up to now the research effort has been mostly limited to catalyst screening and process development with little work having been carried out on mechanism. The following table summarizes some of the results.

Table 1.1. Reported catalytic oxidation reactions using ozone as an oxidant

Substrates	Catalysts	Reaction Conditions	Products	Ref.
CO	CeO ₂	278 – 313 K, 4 l h ⁻¹ , CO: 7.91 × 10 ⁻² – 1.56 × 10 ⁻¹ mol m ⁻³	CO ₂	24
Methane	MgO, Li/MgO	473 – 573 K, 5 mole % ozone in oxygen	H ₂ , CO, and CO ₂	25
Acrylonitrile, methanol, styrene, toluene, 1,2-	Ba-CuO- Cr ₂ O ₃ /Al ₂ O ₃	373 – 773 K, up to 2000 ppm VOCs,	Not specified	32

¹⁹ Bailey, P. S. *Ozonation in Organic Chemistry*, Vol. I, Academic Press, New York, 1978.

²⁰ Bailey, P. S. *Ozonation in Organic Chemistry*, Vol. II, Academic Press, New York, 1982.

²¹ Briner, E. *Adv. Chem. Ser.* **1958**, 21, 184.

²² Bailey, P. S. *Chem. Rev.* **1958**, 58, 925.

²³ Oehschlaeger, H. F. Proc. 2nd Intl. Symposium on Ozone for Water and Wastewater Treatment, Rice, R. G. (ed.), Cleveland, **1983**, 20.

²⁴ (a) A. Naydenov, D. Mehandjiev *CR Bulg. Acad. Sci.*, **1993**, Tome 46, Vol. 6, 49-52. (b) A. Naydenov, R. Stoyanova, D. Mehandjiev *J. Mol. Catal. A* **1995**, 98, 9-14.

²⁵ (a) Hutchings, G. J.; Scurrell, M. S.; Woodhouse, J. R. *Appl. Catal.* **1988**, 38, 157-165. (b) Hutchings, G. J.; Scurrell, M. S.; Woodhouse, J. R. *Catal. Today*, **1988**, 415-419.

dichloroethane				
n-heptane, n-octane	3 Co ₃ O ₄ : 1 MnO ₂	393 – 493 K	CO ₂	35
Ethanol, n-propanol, isopropanol	γ-Al ₂ O ₃ , SiO ₂	293 – 363 K	Aldehydes, ketones, and CO ₂	34
Acetone, benzene, cyclohexane, styrene, toluene	Barium promoted copper- chromite	Room temperature, 250 – 1700 ppm	Not specified	36
Styrene, toluene, acetone, dichloromethane, benzene, carbon tetrachloride, tetrachloroethylene, p-chlorotoluene	Pt/Al ₂ O ₃ , Pd/Al ₂ O ₃ , Ba-CuO- Cr ₂ O ₃ /Al ₂ O ₃ , Fe ₂ O ₃ /Al ₂ O ₃	Ozone: 1 – 2 % (w/w), VOCs: 250 – 2000 ppm, Contact time = 0.2 s, 373 – 873 K	Essentially carbon oxides	26
Benzene	MnO ₂	283 – 353 K	CO, CO ₂	37
Oxalic acid	MnO ₂	283 – 308 K, Aqueous solution, pH = 3.2 – 7.0	Not reported	27
Alkylbenzenes	Cobalt acetate	378 K, [O ₃] ₀ = 7 × 10 ⁻⁵ – 1 × 10 ⁻³ mol l ⁻¹ , [A] ₀ = 10 ⁻³ – 10 ⁻² mol l ⁻¹	Carboxylic acids	28

²⁶ Gervasini, A.; Bianchi, C. L.; Ragaini, V. in *Environmental Catalysis*, J.N. Armor (ed.), ACS Symp. Ser. 552; ACS: Washington, DC, **1994**, 352.

²⁷ Andreozzi, R.; Insola, A.; Caprio, V.; Marotta, R.; Tufano, V. *Appl. Catal. A* **1996**, 138, 75-81.

²⁸ (a) Galstyan, G. A.; Yakobi, V. A.; Tarasenko, A. B.; Galstyan, T. M. *Petroleum Chem. USSR (Eng. Transl.)* **1975**, 15, 146-150. (b) Galstyan, G. A.; Yakobi, V. A.; Tarasenko, A. B.; Galstyan, T. M. *Petroleum Chem. USSR (Eng. Transl.)* **1975**, 15, 146-150.

p-Nitrotoluene	Cobalt acetate	373 K, $[O_3]_0 = 1.4$ vol. %, $[A]_0 = 0.5$ mol l ⁻¹	p-nitrobenzoic acid	29
Cyclohexane, 1,2-dimethyl-cyclohexane, 2-methylbutane	FeCl ₃	Aqueous solution	Alcohols, ketones	30

Since ozone has a much stronger oxidizing ability than oxygen, lower reaction temperatures can be expected when it is used as the oxidant³¹⁻³⁷. In agreement with this reasoning, most of the studies report higher reactivities at low reaction temperatures (Table 1.1). Hutchings and coworkers²⁵ found ozone to be more active and selective than oxygen for methane oxidation at temperatures ≤ 400 °C. Hydrogen, carbon monoxide, and carbon dioxide were the only products observed. However, at higher temperatures there was essentially no difference between ozone and oxygen due to the rapid decomposition of ozone in the gas phase.

Only scarce work on the reaction kinetics and mechanism has been reported. There is general agreement that the addition of ozone decreases the activation energy of oxidation reactions. The kinetics of complete oxidation of benzene by ozone on MnO₂ was investigated by Naydenov and Mehandjiev³⁷. They found that the activation energy for benzene oxidation with ozone (30 kJ mol⁻¹) was much lower than that with oxygen (88 kJ mol⁻¹), but was

²⁹ Galstyan, G. A.; Yakobi, V. A.; Dvortsevoi, M. M.; Galstyan, T. M. *J. Appl. Chem. USSR (Eng. Transl.)* **1978**, *51*, 123-126.

³⁰ Hellman, T. M.; Hamilton, G. A. *J. Amer. Chem. Soc.* **1974**, *96*(5), 1530-1535.

³¹ Gervasini, A.; Vezzoli, G. C.; Ragaini, V. *Catal. Today* **1996**, *29*, 449.

³² Gervasini, A.; Bianchi, C.L.; Ragaini, V. in *Environmental Catalysis*, J.N. Armor (ed.), ACS Symp. Ser. 552; ACS: Washington, DC, **1994**, 352.

³³ Li, W.; Oyama, S.T. in *Heterogeneous Hydrocarbon Oxidation*, B.K. Warren and S.T. Oyama (eds.), ACS Symp. Ser. 638; ACS: Washington, DC, **1996**, 364.

³⁴ Klimova, M. N.; Tarunin, B. I.; Aleksandrov, Yu. A. *Kinet. Katal.* **1988**, *26*, 1143.

³⁵ Hauffe, K.; Ishikawa, Y. *Chem. Ing. Techn.* **1974**, *5*, 1035.

³⁶ Ragaini, V.; Bianchi, C.L.; Forcella, G.; Gervasini, A. in *Trends in Ecological Physical Chemistry*, Bonati, L. (eds.) Elsevier: Amsterdam, **1993**, 275.

³⁷ Naydenov, A.; Mehandjiev, D. *Appl. Catal. A* **1993**, *97*, 17.

similar to that of ozone decomposition (32 kJ mol^{-1}). It was concluded that the rate determining step for benzene oxidation by ozone was ozone decomposition. The reaction orders on benzene and ozone were found to be 1.0 and 0.4 respectively. Klimova *et al.*³⁴ studied the oxidation of lower aliphatic alcohols by ozone over silica and alumina. It was determined that for the oxidation of 1 mole of the alcohols about 1 mole of ozone or less was consumed. By varying the reactor volume while keeping a constant surface area of the catalyst it was demonstrated that the reaction proceeded primarily on the catalyst surface.

Spectroscopic study of ozone oxidation reactions has been rare, and no work has been done under reaction conditions. A recent work³⁸ used FTIR to study the interaction of ozone with phenol adsorbed on silica and ceria. It was found that the reactivity of ozone depended on the adsorption mode of phenol on oxide surfaces, and the intermediate of phenol oxidation was identified as aldehyde or carboxylic acid. However, again the study was carried out at temperatures much lower than reaction temperatures (77 – 177 K), hence its relevance to the “real” reaction is doubtful.

1.3. OBJECTIVES AND APPROACH OF THIS WORK

As summarized in the proceeding sections, mechanistic and kinetic studies of ozone reactions on solid surfaces are lacking, in strong contrast with the vast amount of work carried out on ozone reactions in the gas phase³⁹ and liquid phase. The motivation for this work is to fill this gap.

1.3.1. Objectives

The overall goal of this work is to understand the chemistry of ozone on manganese oxide catalysts. Specific objectives are as follows:

1. Evaluate metal oxide catalysts for ozone reactions, including ozone decomposition and ozone oxidation of ethanol.
2. Establish the kinetics of ozone reactions on a supported manganese oxide catalyst.

³⁸ Mariey, L.; Lamotte, J.; J.C. Lavalley, Tsyganenko, N. M.; Tsyganenko, A. A. *Catal. Lett.* **1996**, *41*, 209-211.

³⁹ Atkinson, R.; Carter, W. P. L. *Chem. Rev.* **1984**, *84*, 437-470.

3. Identify adsorption and reaction intermediates using *in situ* laser Raman spectroscopy, and investigate their behavior.
4. Combine the kinetic and spectroscopic information to derive the mechanism of the reactions on the catalyst surfaces.

In this dissertation we will address the following questions about the chemistry of ozone on manganese oxide surfaces.

1. What is the active oxygen species? Is the active species an atomic oxygen species, a molecular oxygen species, or an ozonide species? The identification of active oxygen species plays a critical role in understanding the activity and selectivity of oxidation reactions^{40,41}. A combination of kinetic measurements, isotopic substitution, and *in-situ* laser Raman spectroscopy will be used to identify the active oxygen species for ozone decomposition and oxidation reactions.
2. What is the relationship between ozone decomposition and ozone oxidation reactions? It has been suggested that in gas phase reactions, ozone first decomposes to generate active atomic species, which subsequently react with organic substrate molecules⁴². It is possible that this reaction pathway is also operating on solid surfaces except that ozone dissociatively adsorbs on the catalyst surface to form the active species. Insights on the relationship between oxidation reactions and the ozone decomposition reaction can be obtained by comparing the rates of these reactions.
3. Are chain reactions involved in the reaction pathway? By monitoring the inlet and outlet concentrations of the organic compound as well as ozone, the converted organic compound to ozone ratio can be calculated. A ratio larger than the reaction stoichiometry implies a chain reaction mechanism.

The emphasis will be on identification and characterization of the reaction intermediates of ozone reactions and elucidation of reaction mechanisms. The unique feature of this work is

⁴⁰ Che, M.; Tench, A. J. *Adv. Catal.* **1982**, *31*, 77.

⁴¹ Che, M.; Tench, A. J. *Adv. Catal.* **1983**, *32*, 1.

⁴² Kleimenov, N. A.; Nalbandian, A. B. *Proc. Acad. Sci. (USSR)* **1958**, *122*, 635.

that *all the measurements were carried out under reaction conditions*, providing an accurate description of the mechanism on the “real” surface.

1.3.2. Approach of This Work

In this dissertation a method for establishing a reaction mechanism, and demonstrate its application to ozone reactions is presented. The approach starts with *in situ* laser Raman spectroscopic study of reaction intermediates. Isotopic substitution measurements and *ab initio* MO calculations are used to identify the reaction intermediates, and isotope jump experiments are applied to gain insights on the reaction pathways. Then the steady state kinetics of the global reaction are measured. At this stage, a reaction sequence can be proposed that not only is consistent with the *in situ* spectroscopic results but also can describe the global kinetics. One important criteria here is that all the kinetic parameters obtained should be physically realistic, *i.e.* all the activation energies should be positive and the preexponential factors should have values that are within the range predicted by transition state theory. A conventional mechanistic study will stop here and claim that the mechanism has been established. However, this is actually not enough because it is commonly found that more than one reaction sequence can describe the global kinetics. Hence more information is needed to pinpoint the mechanism. First, quantitative information on the surface coverage of the reaction intermediates should be obtained from *in situ* spectroscopy measurements and the coverage data should be described using *the same kinetic parameters* used to fit the global kinetics. Second, dynamic experiments such as transient adsorption and desorption measurements should be carried out. These serve as an independent check for the reaction sequence and the transient results must be in agreement with the steady state results. If self-consistency is observed after all these steps, a reaction mechanism can be said to be established. In chapters 2 and 3, the application of this approach will be demonstrated to the ozone decomposition reaction on a supported manganese oxide catalyst.

Reaction of organic substrates with ozone was carried out using ethanol as a representative of volatile organic compounds (VOCs). These compounds have been receiving

increasing attention recently because their harmful effects on human health^{43,44}. The kinetics of the reaction will be determined and *in situ* laser Raman spectroscopy will be applied to observe and identify the reaction intermediates, thereby to shed light on the reaction mechanism. By studying the interaction of ethanol with ozone on manganese oxide surfaces, a better understanding will be obtained about the oxidizing behavior of ozone and will provide insights on designing efficient and economical processes to catalytically eliminate VOCs.

⁴³ Heck, R. M.; Farrauto, R. J. “*Catalytic Air Pollution Control: Commercial Technology*”, Chapter 9, Van Nostrand Reinhold, **1995**.

⁴⁴ Chu, W.; Windawi, H. *Chem. Eng. Prog.* March, **1996**, 37.

CHAPTER 2. *IN SITU* LASER RAMAN STUDIES OF OZONE DECOMPOSITION

2.1. INTRODUCTION

The observation, identification, and characterization of reaction intermediates are essential steps in understanding and establishing a reaction mechanism. However, its implementation for heterogeneous catalytic reactions is not an easy task, especially under reaction conditions.

Several groups have attempted to identify the reaction intermediates of the ozone decomposition reaction. On a silver oxide catalyst¹, Imamura, *et al.* suggested that negatively charged oxygen species were formed upon the introduction of ozone. Although a superoxide species was detected at 75 K using electron paramagnetic spectroscopy (EPR), its role in the ozone decomposition reaction was not clearly determined. Naydenov, *et al.*² identified an O_3^- species on a CeO_2 surface using EPR, however, they found that this species was not involved in the reaction. It was suggested that a highly reactive atomic oxygen species (probably O^\cdot) might be the intermediate. However, prior to this work no direct observation of intermediates under reaction conditions has been accomplished using spectroscopic techniques.

There have been numerous studies of adsorbed oxygen species on oxides due to their key role in oxidation reactions^{3,4}. EPR is a powerful technique for studying such species⁵, yet it has several limitations. For example, diamagnetic species such as O_2^{2-} , O^{2-} are not EPR active, signals on paramagnetic oxides are usually too broad to resolve due to spin coupling, and also *in situ* EPR measurements are difficult to implement⁶ and give low signals at high temperatures. Infrared spectroscopy (IR) is another useful technique that has been widely used to study adsorbed species⁷. However, most oxide catalyst supports, *i.e.* alumina and silica, are very

¹ Imamura, S.; Ikebata, M.; Ito, T.; Ogita, T. *Ind. Eng. Chem. Res.* **1991**, *30*, 217.

² Naydenov, A.; Stoyanova, R.; Mehandjiev, D. *J. Molec. Catal. A.* **1995**, *98*, 9.

³ Che, M.; Tench, A. J. *Adv. Catal.* **1983**, *32*, 1.

⁴ Che, M.; Tench, A. J. *Adv. Catal.* **1982**, *31*, 77.

⁵ Lunsford, J. H. *Catal. Rev.* **1973**, *8(1)*, 135.

⁶ Che, M.; Giamello, E. in *Catalyst Characterization: Physical Techniques for Solid Matyerials*, Imelik, B.; Vedrine, J. C. (Eds.), Plenum: New York, **1994**.

⁷ Davydov, A. A. *Infrared Spectroscopy of Adsorbed Species on the Surface of Transition Metal Oxides*, Wiley: New York, **1984**.

strong absorbers in the mid and low infrared range (1000 - 100 cm^{-1}) where the vibrations of metal-oxygen bonds occur. Hence information on adsorbed species in that range is almost impossible to obtain. In contrast, Raman spectroscopy is uniquely suited for the characterization of supported oxide catalysts because the weak scattering by the catalyst supports gives little interference. In recent years advances in Raman instrumentation have significantly improved the throughput of Raman spectrometers, allowing studies of low concentration adsorbed species. Recent work from this group has demonstrated that *in situ* laser Raman spectroscopy is an excellent tool to study surface intermediates at reaction conditions⁸. In the present work this technique is applied to the ozone decomposition reaction to directly observe and identify adsorbed intermediates, thereby gaining insights of the elementary steps of the reaction. A supported manganese oxide catalyst was chosen in this study because previous work has found that easily reducible transition metal oxides, manganese oxide in particular, are good catalysts for ozone decomposition⁹.

Theoretical calculations using *ab initio* methods have undergone considerable progress in the last decade owing to improvements in computational algorithms and advances in computer hardware. It is now possible, though still challenging, to obtain reliable vibrational frequencies even for compounds involving transition metals¹⁰, with a fraction of the effort needed just a few years ago. Furthermore, the combination of experimental and theoretical approaches has been shown to be particularly powerful toward understanding and establishing reaction mechanisms¹¹. In this chapter, *ab initio* calculation results on two model manganese compounds are reported to help identify the reaction intermediate observed during the ozone decomposition reaction.

⁸ (a) Zhang, W.; Oyama, S. T. *J. Phys. Chem.* **1996**, *100*, 10759. (b) Zhang, W.; Oyama, S. T. *J. Am. Chem. Soc.* **1996**, *118*, 7173.

⁹ Dhandapani, B.; Oyama, S. T. *Chem. Lett.* **1995**, 413-414.

¹⁰ (a) Scott, A.; Radom, L. *J. Phys. Chem.* **1996**, *100*, 16502-16513. (b) Head, J. D. *Int. J. Quantum Chem.* **1997**, *65*, 827-838.

¹¹ (a) Lee, D. G.; Moylan, C. R.; Hayashi, T.; Brauman, J. I. *J. Amer. Chem. Soc.* **1987**, *109*, 3003-3010. (b) Nakai, H.; Ohmori, Y.; Nakatsuji, H. *J. Phys. Chem.* **1995**, *99*, 8550-8555.

2.2. EXPERIMENTAL SECTION AND COMPUTATIONAL DETAILS

2.2.1. Catalyst Preparation

The 10 wt% $\text{MnO}_2/\text{Al}_2\text{O}_3$ used for this study was prepared by the incipient wetness impregnation method. Manganese acetate rather than nitrate was used as the precursor because it has been shown to result in a higher dispersion of manganese oxide on Al_2O_3 ¹². $\text{Mn}(\text{CH}_3\text{CO}_2)_2 \cdot 4\text{H}_2\text{O}$ (Aldrich, > 99.99%; 2.819 g) was dissolved in 9.6 cm³ of distilled water, and the obtained solution was slowly added to 9.70 g of $\gamma\text{-Al}_2\text{O}_3$ (Degussa, Aluminum Oxide C) while stirring. The sample was dried at 423 K and calcined at 773 K for 3 h. X-ray diffraction measurements did not show any features of manganese oxide, indicating that it was well dispersed on the Al_2O_3 support. This agrees with the results of Kapteijn *et al.*¹², who showed that monolayer dispersion of manganese oxide on Al_2O_3 could be achieved for concentration up to 15 wt%, using manganese acetate as the precursor.

2.2.2. In Situ Laser Raman Spectroscopy

The schematic of the *in situ* laser Raman apparatus shows the major components of the system (Figure 2.1). The excitation source was an Ar ion laser (Lexel, 95) providing light with a wavelength of 514.5 nm and a power of 100 mW at the sample. A highly efficient holographic interference filter (Kaiser, Super Notch Plus) was used to remove the Rayleigh line allowing the use of a single-stage monochromator (Spex, 500M) rather than the conventionally used triple monochromator. A charge coupled device (CCD, Spex, Spectrum One) cooled with liquid nitrogen was used as the detector. This set-up offered a much higher throughput and allowed the observation and investigation of low concentration reaction intermediates. A specially designed *in situ* Raman cell enabled the spectrum to be acquired under conditions of controlled temperature and pressure. The catalyst was pressed into a thin wafer about 1 mm thick with a diameter of 15 mm, and was held by a stainless steel cap on a ceramic rod, which was spun at 1000 rpm to avoid sample overheating. The temperature of the sample was measured by a thermocouple installed in a well 3 mm from the sample wafer. Prior to the Raman spectroscopic measurements, the sample was pretreated in flowing oxygen at 773 K for 3 h. The Raman

¹² Kapteijn, F.; Langeveld, A. D.; Moulijn, J. A.; Andreini, A.; Vuurman, M. A.; Turek, A. M.; Jehng, J. M.; Wachs, I. E. *J. Catal.* **1994**, *150*, 94.

spectroscopic measurements were carried out at room temperature (ca. 300 K) and atmospheric pressure unless specified. The Raman spectrometer had a resolution of about 6 cm^{-1} . For the isotope substitution experiments, a specially designed set-up was used (Figure 2.2). Two gas containers were used to store $^{16}\text{O}_2$ (Airco, > 99.6%) and $^{18}\text{O}_2$ (Isotec, > 99 atom %) from which ozone was generated by discharging a Tesla coil. The produced ozone/oxygen mixture (^{18}O and/or ^{16}O) could be introduced into the Raman cell separately or together. The Raman cell as well as the gas containers were evacuated prior to the gas dosing. In other experiments, ozone was produced by passing $^{16}\text{O}_2$ through a high voltage silent discharge ozone generator (OREC, V5-0).

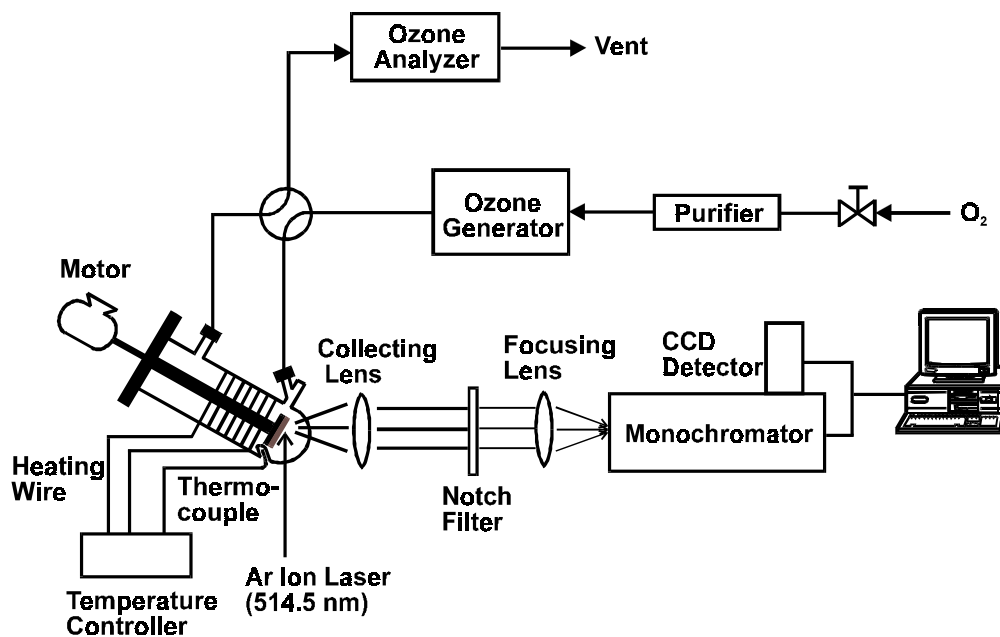


Figure 2.1. Schematic of the experimental set-up for the *in situ* laser Raman experiments.

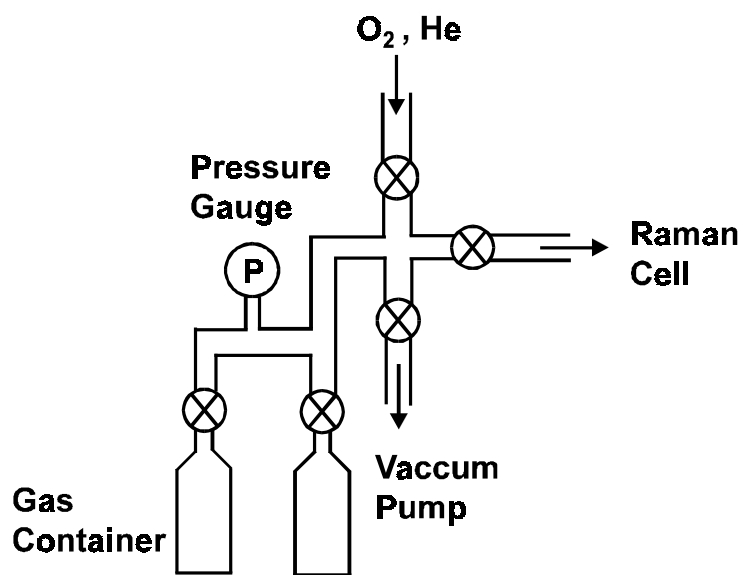


Figure 2.2. Schematic of the set-up for the isotopic substitution experiments.

2.2.3. Calculation Details

All calculations were performed using a GAUSSIAN 94 program¹³. The geometry optimization of manganese model compounds $Mn(OH)_4(O_2)^+$ and MnO_3OH was carried out using the Hartree-Fock method and a 6-311G triple zeta basis set with all electrons treated explicitly. Attempts were also made to add polarized and diffuse functions to the calculation of $Mn(OH)_4(O_2)^+$, however, that resulted in a collapse of the complex. The vibrational frequencies of the compounds were computed by determining the second derivatives of the energy. The raw calculated frequency values at the Hartree-Fock level contain known systematic errors due to the neglect of electron correlation, resulting in overestimates of about 10% – 12%. Hence it is common to scale the predicted frequencies by an empirical factor of 0.8929¹⁴. All the frequencies reported here are scaled by this factor. The oxidation state of manganese in the

¹³ Frisch, M. J.; Trucks, G. W.; Schlegel, H. B.; Gill, P. M. W.; Johnson, B. G.; Robb, M. A.; Cheeseman, J. R.; Keith, T. A.; Peterson, G. A.; Montgomery, J. A.; Raghavachari, K.; Al-Laham, M. A.; Zakrzewski, V. G.; Ortiz, J. V.; Foresman, J. B.; Cioslowski, J.; Stefanov, B. R.; Nanayakkara, A.; Challacombe, M.; Peng, C. Y.; Ayala, P. Y.; Chen, W.; Wong, M. W.; Andres, J. L.; Replogle, E. S.; Gomperts, R.; Martin, R. L.; Fox, D. J.; Binkley, J. S.; Defrees, D. J.; Baker, J.; Stewart, J. P.; Head-Gordon, M.; Gonzalez, C.; Pople, J. A. *GAUSSIAN 94* (revision C.2), Gaussian: Pittsburgh, 1995.

model compounds was chosen to be +7 due to the likelihood that high valent compounds would be found in the presence of the strongly oxidizing ozone¹⁵.

2.3. RESULTS

2.3.1. Raman Spectra of Adsorbed Species

The Raman spectra of the catalyst sample were compared under oxygen and an ozone/oxygen mixture at room temperature (Figure 2.3). The spectrum under pure oxygen (Figure 2.3a) exhibited a peak at 654 cm⁻¹. When the catalyst sample was exposed to an ozone/oxygen mixture, two changes in its Raman spectrum occurred (Figure 2.3b). A sharp new peak at 884 cm⁻¹ was observed, while the peak at 654 cm⁻¹ decreased in intensity and broadened. The peak at 884 cm⁻¹ was accompanied by two very weak peaks at 930 cm⁻¹ and 954 cm⁻¹ (combination bands). The appearance of the new peak was found to be reversible, i.e. the peak disappeared after ozone was purged. However, the intensity decrease of the 654 cm⁻¹ peak was not reversed upon removal of ozone and could only be restored by subsequent treatment in oxygen at an elevated temperature (773 K). An interesting feature of the new signal at 884 cm⁻¹ was that in addition to the fundamental vibration mode the first and second overtones were also visible at 1754 and 2618 cm⁻¹ (not shown), respectively. It should be pointed out that ozone continuously underwent decomposition in the course of these measurements. The kinetics will be treated in depth in chapter 3.

The effect of temperature on the *in situ* Raman spectrum was also studied. The intensity of the signal at 884 cm⁻¹ decreased significantly with increasing temperature (Figure 2.4), and the signal eventually disappeared at ~ 423 K. Meanwhile a new peak at 580 cm⁻¹ increased in intensity with increasing temperature up to 423 K then decreased slightly in intensity with further increases in temperature. A very weak signal at ca. 1020 cm⁻¹ also appeared at higher temperatures (above 373 K).

¹⁴ (a) Pople, J. A.; Krishnan, R.; Schlegel, H. B.; DeFrees, D.; Binkley, J. S.; Frisch, M. J.; Whiteside, R. F.; Hout, R. F.; Hehre, W. J. *Int. J. Quantum Chem., Symp.* **1981**, *15*, 269. (b) Cundari, T.; Raby, P. *J. Phys. Chem. A* **1997**, *101*, 5783-5788.

¹⁵ *Gmelins Handbook of Inorganic Chemistry Mn C1*, pp. 300, 1973.

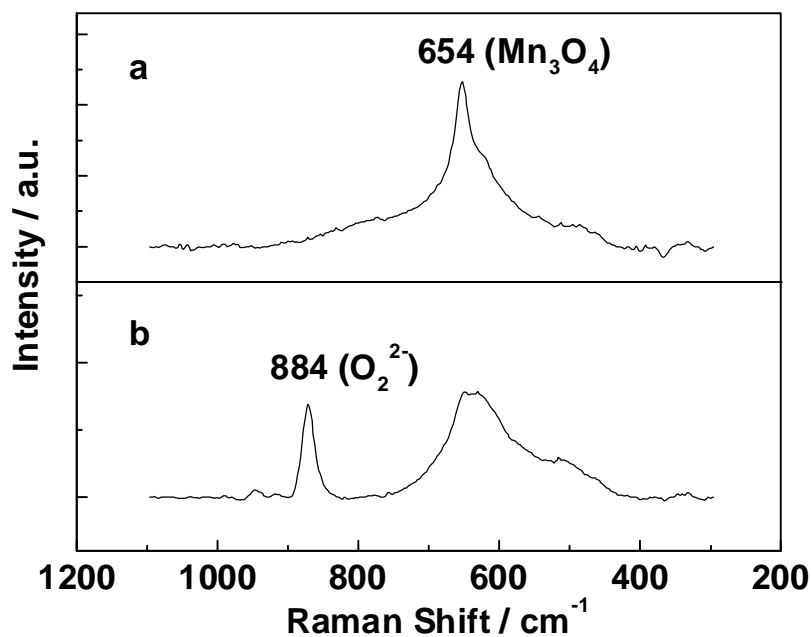


Figure 2.3. *In situ* Raman spectra of the catalyst sample. (a) in oxygen; (b) in a 2 mol% ozone/oxygen mixture. Spectral acquisition conditions: Laser power = 100 mW, resolution = 6 cm⁻¹, exposure time = 30 s, and 60 scans.

2.3.2. Isotopic Substitution

When ozone was generated using ¹⁸O₂ rather than ¹⁶O₂, the signal at 884 cm⁻¹ shifted to 834 cm⁻¹, and the first overtone at 1746 cm⁻¹ also shifted to 1670 cm⁻¹ (Figure 2.5). The ratio of $\nu(^{18}\text{O})/\nu(^{16}\text{O})$ was calculated to be 0.946. The peak at 1556 cm⁻¹ can be assigned to gas phase ¹⁶O₂, while the peak at 1468 cm⁻¹ can be assigned to gas phase ¹⁸O₂¹⁶.

To explore the origin of oxygen in the adsorbed species, *in situ* Raman spectra of the sample were also measured after the surface was exchanged with ¹⁸O₂. The ¹⁸O-exchanged catalyst surface was obtained by repeated cycles of reduction in H₂ at 623 K for 1 h followed by oxidation in ¹⁸O₂ at 623 K for 1 h. The reduction and oxidation temperature was determined from a temperature programmed reduction (TPR) profile of the catalyst sample, and was chosen to be the temperature just below that when the bulk sample began to be reduced. The Raman spectrum of the ¹⁸O-exchanged surface showed no difference compared to that of the

¹⁶ Selig, H., Claassen, H. H. *Israel J. Chem.* **1968**, 6, 499-500.

unexchanged surface. The Raman spectra with $^{16}\text{O}_3$ and $^{18}\text{O}_3$ also exhibited no differences with those on the unexchanged surface (Figure 2.6).

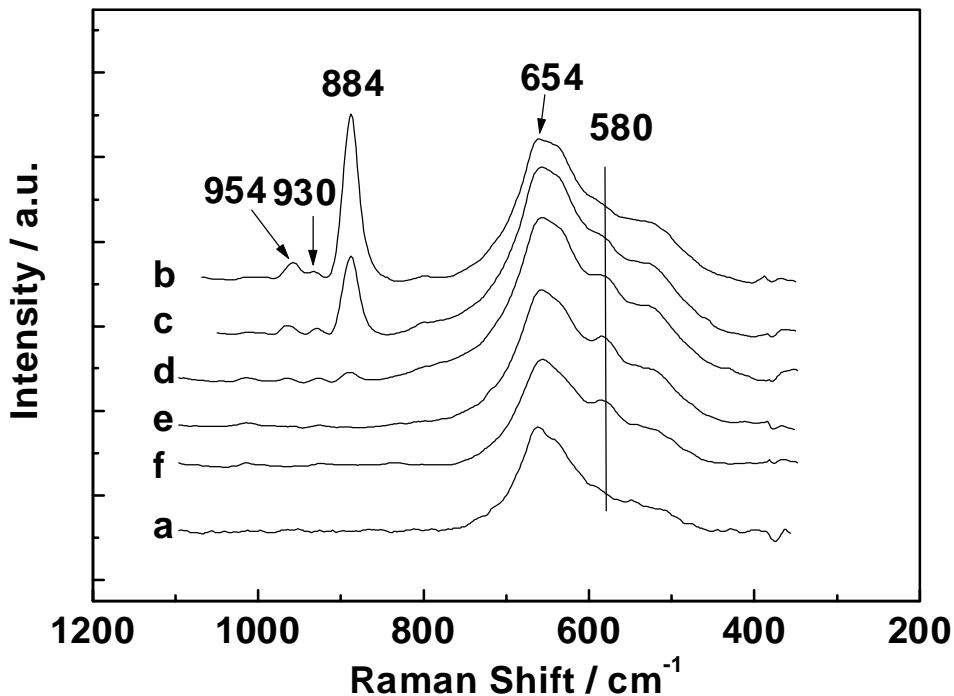


Figure 2.4. *In situ* Raman spectra of the catalyst sample in a 2 mol% ozone/oxygen mixture (except a) at various temperatures. (a) 293 K in pure oxygen; (b) 293 K; (c) 323 K; (d) 373 K; (e) 423 K; (f) 473 K. Spectral acquisition conditions: Laser power = 100 mW, resolution = 6 cm^{-1} , exposure time = 30 s, and 60 scans.

When a mixture of $^{16}\text{O}_3$ and $^{18}\text{O}_3$ without mixed isotopes ($^{16}\text{O}_2^{18}\text{O}$, $^{16}\text{O}^{18}\text{O}_2$) was decomposed, three peaks were observed at 886 cm^{-1} , 860 cm^{-1} , and 836 cm^{-1} (Figure 2.7). The mixture was formed by mixing $^{16}\text{O}_3/^{16}\text{O}_2$ and $^{18}\text{O}_3/^{18}\text{O}_2$ which were separately prepared by discharging a Tesla coil in $^{16}\text{O}_2$ and $^{18}\text{O}_2$, respectively (Figure 2.2).

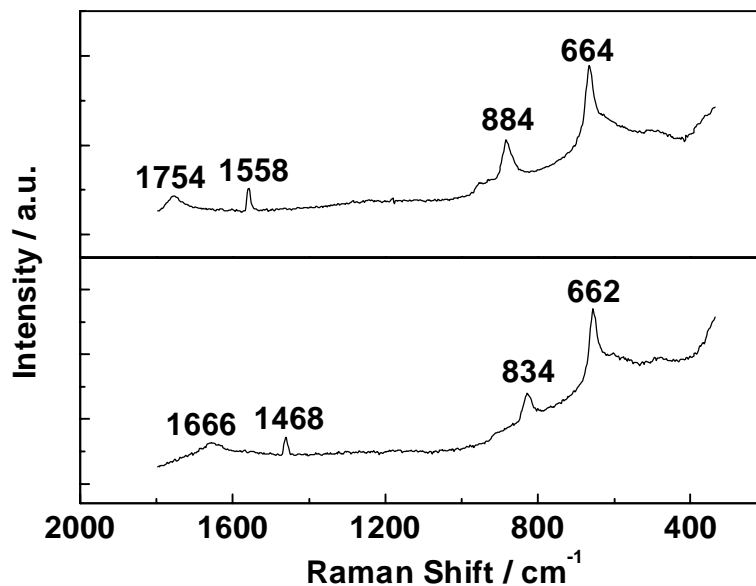


Figure 2.5. *In situ* Raman spectra of unexchanged sample after ozone adsorption. (a) $^{16}\text{O}_3/^{16}\text{O}_2$; (b) $^{18}\text{O}_3/^{18}\text{O}_2$. Spectral acquisition conditions: Laser power = 100 mW, resolution = 6 cm^{-1} , and exposure time = 30 s.

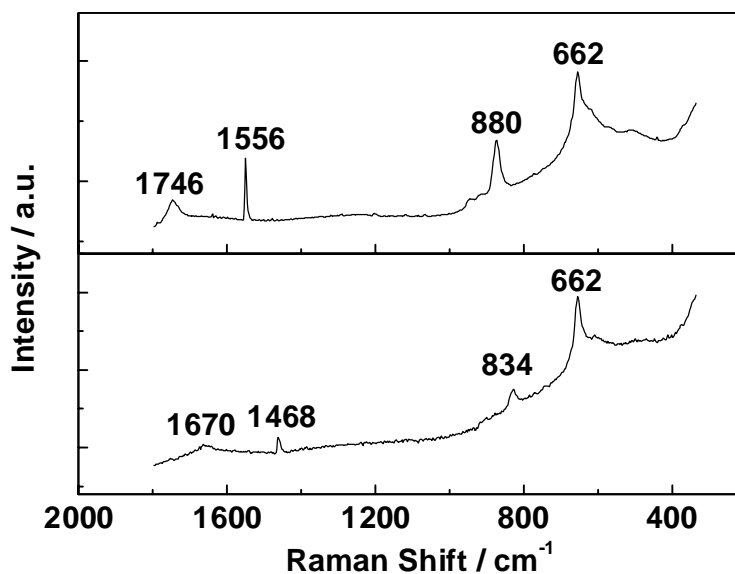


Figure 2.6. *In situ* Raman spectra of ^{18}O -exchanged sample after ozone adsorption. (a) $^{16}\text{O}_3/^{16}\text{O}_2$; (b) $^{18}\text{O}_3/^{18}\text{O}_2$. Spectral acquisition conditions: Laser power = 100 mW, resolution = 6 cm^{-1} , and exposure time = 30 s.

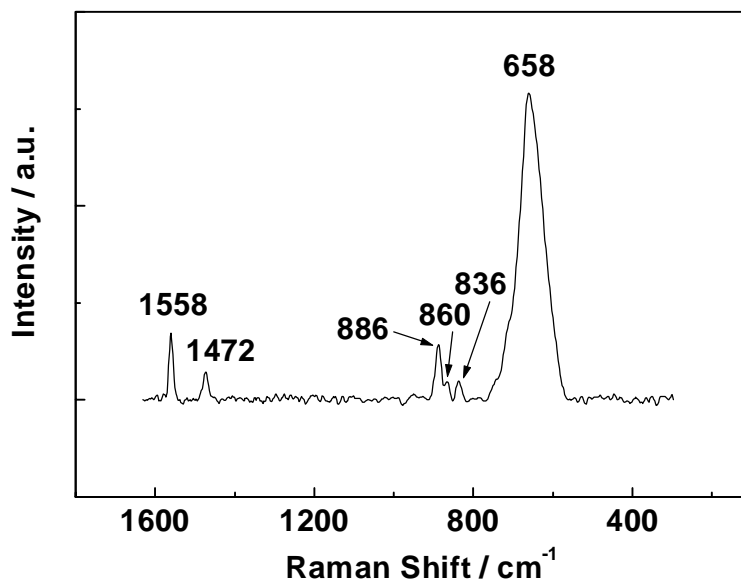


Figure 2.7. *In situ* Raman spectra of the catalyst sample in a mixture of $^{16}\text{O}_3/^{16}\text{O}_2$ and $^{18}\text{O}_3/^{18}\text{O}_2$. Spectral acquisition conditions: Laser power = 100 mW, resolution = 6 cm^{-1} , and exposure time = 30 s.

Raman measurements were also carried out in a sequential way. The catalyst sample was first exposed to an $^{18}\text{O}_3/^{18}\text{O}_2$ mixture. Then after a brief purging by helium, an $^{16}\text{O}_3/^{16}\text{O}_2$ mixture was introduced. The resulting Raman spectrum (Figure 2.8) exhibited only two peaks at 856 cm^{-1} and 882 cm^{-1} .

2.3.3. *Ab Initio* Calculations of Model Mn Compounds

Model calculations were completed on MnO_3OH and $\text{Mn}(\text{OH})_4(\text{O}_2)^+$ for reasons to be discussed later. The optimized geometries are shown in Figure 2.9. The optimized structure of MnO_3OH has C_s point symmetry while that of $\text{Mn}(\text{OH})_4(\text{O}_2)^+$ has C_{2v} symmetry. The details of the calculation output are given in Appendix A.

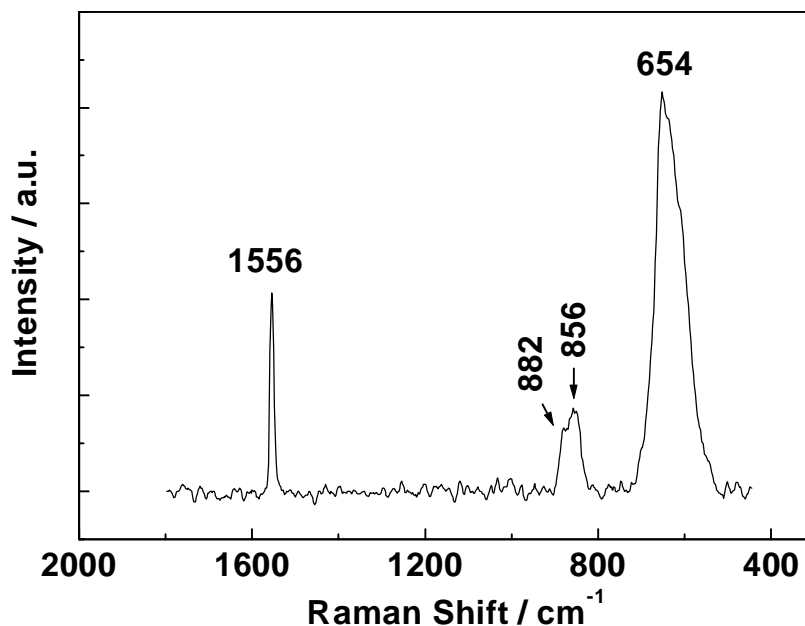


Figure 2.8. *In situ* Raman spectra of the catalyst sample after a sequential adsorption of ozone. The catalyst sample was first exposed to an $^{18}\text{O}_3/^{18}\text{O}_2$ mixture. Then after a brief purging by helium, an $^{16}\text{O}_3/^{16}\text{O}_2$ mixture was introduced. Spectral acquisition conditions: Laser power = 100 mW, resolution = 6 cm^{-1} , and exposure time = 30 s.

The GAUSSIAN program also calculates the peak intensity of infrared and Raman spectra, though only the order of intensity rather than the absolute values is reliable. We will only consider the vibrational frequencies with a significant Raman intensity. Both complexes have Raman signals ($\text{Mn}(\text{OH})_4(\text{O}_2)^+$ 899 cm^{-1} , and MnO_3OH 859 cm^{-1}) positioned close to the observed signal of the adsorbed species, suggesting that criteria other than the frequency value need to be used to distinguish between the two model complexes. Vibrational frequencies of isotopically substituted complexes of $\text{Mn}(\text{OH})_4(\text{O}_2)^+$ (Table 2.1) and MnO_3OH (Table 2.2) were also calculated to determine the isotope shift of these two Raman signals. The O-O stretching in $\text{Mn}(\text{OH})_4(\text{O}_2)^+$ exhibited an isotopic shift of 47 cm^{-1} , corresponding to a $\nu(^{18}\text{O})/\nu(^{16}\text{O})$ value of 0.948, while in MnO_3OH a $\nu(^{18}\text{O})/\nu(^{16}\text{O})$ value of 0.969 was obtained. It was also found that the frequency value of the O-O stretching mode in $\text{Mn}(\text{OH})_4(\text{O}_2)^+$ did not change when the oxygen

atoms in the hydroxyl groups were replaced with ^{18}O , suggesting that this vibrational mode is highly localized.

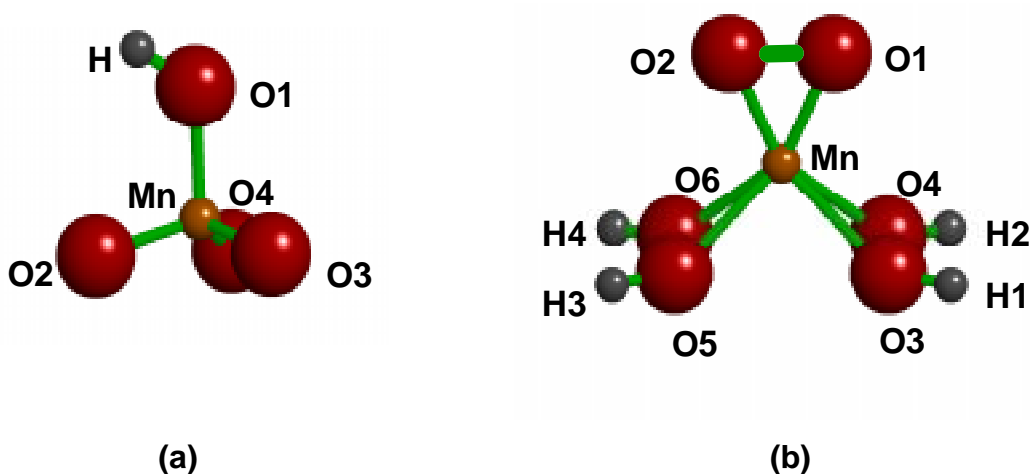


Figure 2.9. Optimized structure of manganese model compounds. (a) MnO_3OH , C_s symmetry. Selected bond lengths and angles: Mn-O1 0.176 nm, Mn-O2 0.156 nm, O1-Mn-O2 105.4°, O2-Mn-O3 111.7°. (b) $\text{Mn}(\text{O}_2)(\text{OH})_4^+$, C_{2v} symmetry. Selected bond lengths and angles: Mn-O1 0.176 nm, Mn-O3 0.212 nm, O1-O2 0.146 nm, O3-O4 0.144 nm, O3-O5 0.302 nm, O1-Mn-O2 49.3°.

Table 2.1. Calculated Vibrational Frequencies of ^{18}O -substituted $\text{Mn}(\text{OH})_4(\text{O}_2)^+$

$\text{Mn}(^{16}\text{O}_2)(^{16}\text{OH})_4^+$	899 cm^{-1}
$\text{Mn}(^{18}\text{O}_2)(^{16}\text{OH})_4^+$	852 cm^{-1}
$\text{Mn}(^{16}\text{O}^{18}\text{O})(^{16}\text{OH})_4^+$	876 cm^{-1}
$\text{Mn}(^{16}\text{O}_2)(^{18}\text{OH})_4^+$	899 cm^{-1}

An unusual feature in the optimized structure of $\text{Mn}(\text{OH})_4(\text{O}_2)^+$ is that the two neighboring oxygen atoms in the hydroxyl groups are very close (0.1437 nm) to one another, suggesting that there are interactions between the hydroxyl groups. The reason for this is unknown.

Table 2.2. Calculated Vibrational Frequencies of ^{18}O -substituted $\text{MnO}_3(\text{OH})$

$\text{Mn}^{16}\text{O}_3^{16}\text{OH}$	859*, 938, 1020 cm^{-1}
$\text{Mn}^{18}\text{O}^{16}\text{O}_2^{16}\text{OH}$	855, 915, 1002 cm^{-1}
$\text{Mn}^{16}\text{O}^{18}\text{O}_2^{16}\text{OH}$	852, 901, 976 cm^{-1}
$\text{Mn}^{18}\text{O}_3^{16}\text{OH}$	832*, 901, 969 cm^{-1}

2.3.4. Temperature Programmed Desorption (TPD) of Ozone

Temperature programmed desorption (TPD) of O_2 was carried out after ozone adsorption to characterize the adsorbed species on the catalyst surface. After passing an ozone/oxygen mixture through the catalyst bed, the sample was briefly purged with He, and its temperature was increased using a linear temperature program (0.17 K s^{-1}) while the mass spectrometry (MS) signals of $m/e = 48$ (O_3) and 32 (O_2) were monitored. O_2 was the only desorption product observed. The desorption curve after O_3 adsorption showed two extra peaks at 406 K and 532 K in addition to those peaks at 618 K and 807 K observed after O_2 adsorption (Figure 2.10). The peaks at higher temperatures are probably due to the release of the lattice oxygen of manganese oxides, while the two new peaks at lower temperatures are the desorption products of adsorbed species of ozone.

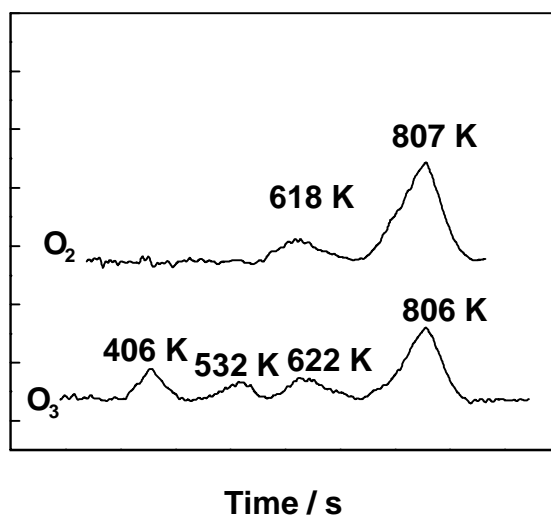


Figure 2.10. TPD profiles of O_2 signals after O_2 and O_3 adsorption.

2.4. DISCUSSION

2.4.1. Raman Spectra of the Adsorbed Species

Due to the dark color of the manganese sample (deep brown), the Raman spectra should be considered mainly as indicative of near surface phases. The peak at 654 cm^{-1} can be ascribed to Mn_3O_4 ¹². However, this observation does not rule out the presence of other phases because MnO_2 is Raman inactive, while Mn_2O_3 and MnO show only very weak Raman signals. The intensity decrease of the Mn_3O_4 signal upon exposure to ozone indicates that the dispersed manganese oxide is partially oxidized by ozone. Also this oxidation seems to be irreversible since the peak intensity is not recovered even after ozone is purged.

The new signal at 884 cm^{-1} suggests that a new species has been formed on the catalyst surface during the ozone decomposition reaction. The possibility that this signal is due to a gas phase species is ruled out with blank experiments in the absence of the catalyst. This is the first case of direct spectroscopic detection of an adsorbed species during ozone decomposition. The signal at 884 cm^{-1} can be assigned to an adsorbed peroxide species as discussed in detail shortly. The fact that its overtones were also observed suggests that this signal could be resonance enhanced. This is not unusual since resonance Raman spectra of several manganese oxo compounds¹⁷ (MnO_4^- , MnO_3F , $\text{Mn}(\text{TPP})\text{O}_2$, $\text{Mn}(\text{TTP})\text{O}_2$, etc.) have been reported.

The new signals at 580 cm^{-1} and 1020 cm^{-1} are probably related to atomic oxygen species (Figure 2.4). However, they are not detectable at low temperatures, being only measurable at temperatures above 373 K. This suggests a higher thermal stability of the atomic oxygen species compared to molecular oxygen species. The reason they are not observable at lower temperatures will be discussed later. We are interested in the lower temperature range where catalytic ozone decomposition dominates, not in the higher temperature region where gas phase decomposition becomes significant. These signals are not associated with the most abundant reaction intermediate (*mari*) of the reaction but a byproduct of the ozone dissociative adsorption as will be discussed later.

¹⁷ (a) Weselucha-Birczynska, A.; Proniewicz, L. M.; Bajdor, K.; Nakamoto, K. *J. Raman Spectrosc.* **1991**, *22*, 315-319. (b) Kiefer, W.; Bernstein, H. J. *Chem. Phys. Lett.* **1971**, *8(5)*, 381-383. (c) Czernuszewicz, R. S.; Su, Y. O.; Stern, M. K.; Macor, K. A.; Kim, D. Groves, J. T.; Spiro, T. G. *J. Amer. Chem. Soc.* **1988**, *110*, 4158-4165. (d) Nick, R. J.; Ray, G. B.; Fish, K. M.; Spiro, T. G.; Groves, J. T. *J. Amer. Chem. Soc.* **1991**, *113(5)*, 1838-1840.

2.4.2. Assignment of the Adsorbed Species

Definitive identification of an adsorbed species is almost always a difficult task, but results using more than one technique can improve the reliability of the assignment. For this observed adsorbed species, we combine vibrational frequency measurements of the unsubstituted and ^{18}O -substituted species with *ab initio* calculations to select from several possible candidates.

The characteristic vibrational frequencies of adsorbed oxygen species have been summarized in a review³. Several species, including Mn=O, Mn-O-Mn, and O_2^{2-} , can be considered as possibilities. Also a recent study on MnO_3F ¹⁸ reported its Raman spectrum with a signal at 886 cm^{-1} . Since F was not present in our system, it was replaced by OH and calculations were carried out on the compound MnO_3OH , a model compound in which the Mn=O vibration was found not to change with the substitution of F with OH.

Although peroxide and Mn-O-Mn species have similar frequencies⁴, the thermal stability of the peroxide species is usually much lower than that of the Mn-O-Mn species¹⁹. The observed adsorbed species was found to disappear when the temperature was raised to *ca.* 423 K, suggesting that the observed signal is more likely to be due to a molecularly adsorbed oxygen rather than the Mn-O-Mn group.

Ozonide (O_3^-) species have also been reported for ozone adsorption on oxide surfaces²⁰ as well as in matrix isolation reactions of ozone with alkali and alkali earth metals²¹. The signals of the ozonide species were usually in the range of 800-900 cm^{-1} , but those measurements were carried out at very low temperatures (< 100 K), and it has been observed that these adsorbed ozonide species quickly disappeared with increasing temperature²⁰. Hence the observed species is unlikely to be due to an ozonide species.

2.4.2.1. Isotopic Substitution Experiments

The isotope shifts of the observed species and those of the several possible candidates are listed in Table 2.3. The shift is expressed as the ratio of the vibrational frequency of the ^{18}O substituted species and that of the unsubstituted species $\nu(^{18}\text{O})/\nu(^{16}\text{O})$. Since more than one

¹⁸ Varetto, E. L. *J. Raman Spectrosc.* **1991**, 22(5), 307-309.

¹⁹ Onishi, T. in *Dynamic Processes on Solid Surfaces*, ed. Tamaru, K., Plenum: New York, 1994, pp. 237-259.

²⁰ Bulanin, K. M.; Lavalley, J. C.; Tsyganenko, A. A. *J. Phys. Chem. B* **1997**, 101, 2917-2922.

oxygen atom is present in some species, the shift caused by ^{18}O substitution of one, two, and three oxygen atoms are listed in columns 2, 3, 4, respectively. For $\text{Mn}=\text{O}$ and O_2^{2-} species, a harmonic diatomic model is assumed. The isotope shift of the observed species (0.946) is very close to that of a peroxide species (0.943), indicating that the observed species can be assigned to a peroxide species.

Table 2.3. Isotopic Shifts ($\text{O}^{18}/\text{O}^{16}$) of Various Species

	^{18}O Substitution		
	Single	Double	Triple
Mn=O	0.956		
O-O	0.972	0.943	
MnO ₃ OH	0.976	0.964	0.955
Observed	0.946		

Peroxide species have been reported on various oxide catalysts. Onishi, *et al.* identified a peroxide species with a vibrational frequency of 883 cm^{-1} on a partially reduced CeO_2 surface using FT-IR²². Lunsford, *et al.* carried out an *in situ* Raman study on oxidative coupling catalysts²³, in which a surface peroxide species with a Raman signal at 863 cm^{-1} was observed and its role in methane activation was discussed. Lunsford *et al.*²⁴ and Bell *et al.*²⁵ also detected surface peroxide species on Ba/MgO catalysts. The spectrum of the peroxide species was characterized by a major line at 842 cm^{-1} , with minor peaks at 829 and 821 cm^{-1} . Also for ozone decomposition, a negatively charged species was suggested as the reaction intermediate^{1,9}, in agreement with the present work.

²¹ (a) Spiker, R. C.; Andrews, L. *J. Chem. Phys.* **1973**, *59*, 1851-1862. (b) Andrews, L.; Spiker, R. C. *J. Chem. Phys.* **1973**, *59*, 1863-1871. (c) Jacox, M. E.; Milligan, D. E. *J. Molec. Spectrosc.* **1972**, *43*, 148-167.

²² Li, C.; Domen, K.; Maruya, K.; Onishi, T. *J. Am. Chem. Soc.* **1989**, *111*, 7683.

²³ Mestl, G.; Knozinger, H.; Lunsford, J. H. *Bunsenges. Phys. Chem.* **1993**, *97*(3), 319.

²⁴ Lunsford, J. H.; Yang, X.; Haller, K.; Mestl, L. G.; Knozinger, H. *J. Phys. Chem.* **1993**, *97*, 13810.

²⁵ Su, S. C.; Bell, A. T. *Catal. Lett.* **1996**, *36*, 15.

2.4.2.2. *Ab Initio* Calculations of Model Mn Compounds

Ab initio calculations on several manganese model compounds indicate that the used methodology is able to generate reliable geometry and vibrational frequencies of manganese compounds. It was found that a peroxide complex $\text{Mn}(\text{OH})_4(\text{O}_2)^+$ can serve as an appropriate model for the observed adsorbed species. Both the calculated vibrational frequency (899 cm^{-1}) and isotope shift $\nu(^{18}\text{O})/\nu(^{16}\text{O})$ value (0.948) are in excellent agreement with the experimental values (884 cm^{-1} and 0.946). This strengthens our assignment of this adsorbed species as a peroxide complex.

For MnO_3OH , the Raman signal lies in the range where the adsorbed species was observed, but the isotopic shift (0.969) does not match. In addition it is very unlikely that all three terminal oxygens will have originated from the ozone molecule. If there is partial mixing with surface ^{16}O , the isotopic shift will be further apart from the observed value.

2.4.2.3. Manganese Peroxide Complexes

Manganese dioxygen complexes have attracted considerable interest due to their suggested roles in important enzymatic reactions such as superoxide dismutation and photosynthesis reactions²⁶. Four manganese peroxide compounds have been structurally determined and characterized: a monomeric side-on Mn(III) porphyrin compound $\text{Mn}^{\text{III}}(\text{TPP})(\text{O}_2)^{-27}$, a binuclear (μ -peroxo)dimanganese(IV) complex $[\text{L}_2\text{Mn}_2(\mu\text{-O})_2(\mu\text{-O}_2)](\text{ClO}_4)_2$ ($\text{L} = 1,4,7\text{-trimethyl-1,4,7-triazacyclononane}$), a trinuclear ($\mu_3\text{-oxo}$, μ -peroxo) Mn(III) complex²⁸, and a monomeric side-on peroxo manganese(III) complex $\text{Mn}(\text{O}_2)(3,5\text{-iPr}_2\text{pzH})(\text{HB}(3,5\text{-iPr}_2\text{pz})_3)^{29}$. In all these complexes the peroxo species adopts a side-on geometry with O-O distances, from 0.142 – 0.146 nm, consistent with that of the peroxide model $\text{Mn}(\text{OH})_4(\text{O}_2)^+$. It should be noted that the highest oxidation state of manganese in these complexes is +4 in contrast to +7 in the model compound. No information is available in the literature for the dependence of O-O bond length

²⁶ Pecoraro, V. L.; Baldwin, M. J.; Gelasco, A. *Chem. Rev.* **1994**, *94*, 807-826.

²⁷ VanAtta, R. B.; Strouse, C. E.; Hanson, L. K.; Valentine, J. S. *J. Amer. Chem. Soc.* **1987**, *109*, 1425-1434.

²⁸ Bhula, R.; Gainsford, G. J.; Weatherburn, D. C. *J. Amer. Chem. Soc.* **1988**, *110*, 7550-7552.

²⁹ Kitajima, N.; Komatsuzaki, H.; Hikichi, S.; Osawa, M.; Moro-oka, Y. *J. Amer. Chem. Soc.* **1994**, *116*, 11596-11597.

on the oxidation state of manganese due to the limited number of structurally characterized manganese peroxide compounds. However, the bond length of Mn-O was found not to be affected by the oxidation state of manganese³⁰. The vibrational frequencies of the O-O stretching in these complexes vary from 812 cm⁻¹ to 990 cm⁻¹, also in agreement with those observed and calculated for the peroxide species in this work. As mentioned earlier, the oxidation state of manganese was chosen to be +7 due to the extremely strong oxidizing ability of ozone. It is well known that manganese compounds in such higher oxidation states are usually unstable and decompose to release oxygen¹⁷. This suggests that the optimized geometry of the peroxide species probably corresponds to a local minimum with a very shallow potential well. This is in agreement with the characteristics of the observed adsorbed species. This adsorbed species can only be observed in the presence of ozone, and gradually disappears when ozone is removed.

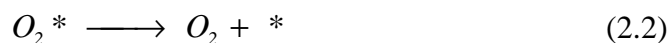
2.4.3. Reaction Pathways

From the results of this investigation it can be deduced that ozone adsorbs to form a peroxide intermediate. The experiment in which the surface was preexchanged with ¹⁸O demonstrated that no change in the vibrational frequency occurred (Figure 2.6). Thus, it can be concluded that both atoms of the peroxide species must come from ozone. The chemisorption is likely to be a dissociative process:



Here the symbol * represents a surface site. The observed higher thermal stability of the atomic oxygen than the molecularly adsorbed species has been reported before¹⁹. When ozone is removed from the gas phase the intensity of the surface peroxide signal decreases gradually with time. This suggests that a second step in the ozone decomposition reaction is therefore a slow desorption of the peroxide species to form gaseous oxygen.

³⁰ Palenik, G. J. *Inorg. Chem.* **1997**, *36*, 4888-4890.



The fate of the atomic oxygen species can be deduced from the isotopic substitution experiments. When a mixture of $^{16}O_3$ and $^{18}O_3$ without ozone of mixed isotopes ($^{16}O_2^{18}O$, $^{16}O^{18}O_2$) was decomposed, three peaks corresponding to the peroxide species ($^{16}O_2$, $^{16}O^{18}O$, and $^{18}O_2$) were observed (Figure 2.7), indicating that the atomic oxygen species must be transformed to the peroxide species. Two processes can accomplish this:



Since only Raman signals due to $^{16}O^{18}O^{2-}$ and $^{16}O_2^{2-}$ species were observed after sequential introduction of $^{16}O_3$ after $^{18}O_3$, a bimolecular surface reaction is ruled out (Figure 2.8). Hence a Rideal-Eley type reaction of another gaseous ozone molecule with a surface atomic oxygen to form an adsorbed peroxide species and a gaseous oxygen molecule is probably the dominating process. This process is expected to be very fast from the simultaneous appearance of the mixed isotopes in the peroxide species when the sample was exposed to a mixture of $^{16}O_3$ and $^{18}O_3$. This also explains the absence of the atomic oxygen species at lower temperatures since they are rapidly transformed to the peroxide species. However, at higher temperatures (> 373 K), gas phase decomposition of ozone becomes significant, resulting in a much lower ozone concentration in the gas phase. Hence the rate of transformation of the atomic species to the peroxide species decreases, rendering the appearance of the signal of the atomic species in the Raman spectra.

In summary ozone adsorbs dissociatively on the catalyst surface to form a peroxide and an atomic oxygen species. The atomic species reacts quickly with another gaseous ozone to form another peroxide species and a gas phase oxygen molecule. The adsorbed peroxide species is the *mar*, and it desorbs to form a gas phase oxygen molecule. This mechanism explains why transition oxides, like manganese oxides which have easily accessible multiple oxidation states, are good catalysts for ozone decomposition. The mechanism consists mainly of redox steps: adsorption of ozone on the catalyst and desorption of the adsorbed intermediates. At steady

state, the rates of these steps are equal. Consequently, the faster the catalyst undergoes oxidation and reduction, the faster will be the rate of the decomposition reaction.

2.5. CONCLUSIONS

The critical steps occurring and species formed during ozone decomposition were investigated using laser Raman spectroscopy on a supported manganese oxide catalyst. An adsorbed species with a Raman signal at 884 cm^{-1} was observed during reaction, and this species was assigned to a peroxide species by using a combination of *in situ* Raman spectroscopy and ^{18}O isotopic substitution. The observed isotope shift $\nu(^{18}\text{O})/\nu(^{16}\text{O})$ value of this adsorbed species was 0.946, in excellent agreement with the ratio expected for a peroxide species (0.943). Theoretical calculations using a Hartree-Fock method confirmed this assignment, and $\text{Mn}(\text{OH})_4(\text{O}_2)^+$ was found to be a good model compound for the adsorbed species.

The reaction steps in ozone decomposition were elucidated with carefully designed experiments using isotopic substitution. The decomposition involved the dissociative adsorption of ozone to form a peroxide species and an atomic oxygen species, the reaction of the atomic species with gaseous ozone molecule to form an adsorbed peroxide species and gas phase oxygen, and the desorption of the peroxide intermediate. This reaction sequence will be treated in the next chapter using transient and steady state kinetic measurements of the ozone decomposition reaction and the adsorbed peroxide intermediate.

CHAPTER 3. KINETIC STUDIES OF OZONE DECOMPOSITION

3.1. INTRODUCTION

This chapter reports an in-depth kinetic study of ozone decomposition on manganese oxide, the most active of the transition metal oxides for this reaction. The work includes determination of the steady state and transient kinetics, measurement of the surface coverage during reaction by *in situ* laser Raman spectroscopy, and analysis of the results using uniform and non-uniform surface treatments.

Observation and identification of adsorbed species under reaction conditions is an essential step in establishing reaction mechanisms. However, all observed species do not necessarily play an important role in the catalytic cycle¹. In fact, it has been reported that in some cases the most abundant species on the catalyst surfaces are merely inert spectators that do not participate in the reaction². To ascertain the role of an adsorbed species in a catalytic cycle, its steady state and transient kinetic behavior has to be determined and shown to be consistent with the overall kinetics of the reaction¹.

As reported in Chapter 2, an adsorbed species was observed on a manganese oxide catalyst during the ozone decomposition reaction, and was identified as a peroxide species using a combination of *in situ* laser Raman spectroscopy with isotopic substitution and *ab initio* MO calculations. The objective of this work is to investigate the steady state and transient kinetics of this species and the overall decomposition reaction to establish its role in the reaction sequence.

It is commonly believed that the relationship between kinetic data and mechanism model is unidirectional³, in the sense that a mechanism can be used to derive a rate expression, but kinetic data alone cannot be used to establish a mechanism. Usually more than one model can give a reasonably good fit to kinetic data. As discussed in Chapter 1, transient adsorption and desorption measurements in combination with surface coverage data can provide the additional

¹ Tamaru, K. *Dynamic Heterogeneous Catalysis*; Academic Press: London, 1978.

² (a) Noto, Y.; Fukuda, K.; Onishi, T.; Tamaru, K. *Trans. Faraday Soc.* **1967**, *63*, 2300. (b) Ekerdt, J. G.; Bell, A. T. *J. Catal.* **1978**, *48*, 111. (c) Yamasaki, H.; Kobori, Y.; Naito, S.; Onishi, T.; Tamaru, K. *J. Chem. Soc., Faraday Trans. 1* **1981**, *77*, 2913. (d) Galuszka, J.; Chang, J. R.; Amenomiya, Y. *Proc. 7th Int. Cong. Catal.* **1981**, 529. (e) Zhang, W.; Oyama, S. T. *J. Amer. Chem. Soc.* **1996**, *118*, 7173-7177.

information needed to pinpoint a reaction mechanism¹. It will be shown by the techniques discussed here that the ozone decomposition reaction proceeds by two kinetically significant steps, the adsorption of ozone to form a peroxide intermediate and the desorption of this intermediate to produce molecular oxygen.

3.2. EXPERIMENTAL SECTION

Details of the experimental setup have been presented in Chapter 2. Briefly, the kinetic measurements were carried out on a 10 wt% MnO₂/Al₂O₃ sample prepared by the incipient wetness impregnation method. Its surface area was measured to be 87 m² g⁻¹ using the BET method. The sample (0.20 g) was pressed into a wafer of 1mm in thickness and 15 mm in diameter, and was spun at 1000 rpm to avoid sample overheating. Prior to all measurements the sample was pretreated in flowing oxygen at 773 K for 3 h. Ozone was produced by passing filtered oxygen (Airco, > 99.6%) through a high voltage silent discharge ozone generator (OREC, V5-0). The mixture of ozone and oxygen with a controlled partial pressure of ozone could be introduced into an *in situ* Raman cell at various temperatures. The volume of the cell was small (< 25 cm³), permitting rapid gas phase changes (< 1.5 s) in transient experiments. An UV absorption type ozone analyzer (IN-USA, AFX-H1) was used to measure the concentrations of ozone. The reaction temperature was varied from 281 K to 340 K, and the ozone partial pressure was changed from 4.7 Pa to 2.1 kPa. The flow rate of the ozone/oxygen mixture was set at 744 μmol s⁻¹ (1000 cm³ min⁻¹). The steady state rate was determined by monitoring ozone concentrations at the inlet and outlet of the Raman cell and the turnover rate was calculated using an active center concentration of 160 μmol, based upon estimates of the dispersion of the catalyst from X-ray diffraction (~70%).

³ (a) Dumesic, J. A.; Rudd, D. F.; Aparicio, L. M.; Rekoske, J. E.; Trevino, A. A. *The Microkinetics of Heterogeneous Catalysis*; American Chemical Society: Washington, DC, 1993; pp. 24. (b) Burwell, R. L. *Catalysis: Sci. & Technol.* **1991**, *9*, 1-85.

3.3. RESULTS

3.3.1. Effect of Laser

In order to investigate the behavior of the peroxide species quantitatively, it is essential to ascertain that the laser beam will not influence its concentration or the reaction kinetics. The ozone decomposition activity was compared at conditions with and without the laser on, and it was found that the laser did not affect the decomposition rate under the reaction conditions employed here. This is likely due to the high flow rate of the ozone/oxygen mixture, and the fast spin rate of the sample. The effect of laser power on the coverage of the peroxide species (*i.e.* Raman signal intensity) was also investigated. Raman spectra of the adsorbed species were acquired at different laser powers, while the total detector exposure (\propto laser power \times exposure time) was fixed by adjusting the exposure time. When the sample was spun at 800 rpm, the peak intensity dropped gradually with increasing laser power (Figure 3.1a). As will be seen, the peak intensity is directly related to the coverage. This indicated that under this condition the laser radiation caused a decrease in the concentration of the surface species, probably due to the heating of the sample. However, when the spin rate was increased to 1000 rpm (Figure 3.1b), the peak area stayed constant with increasing laser power. Hence at this spin rate, the effect of the laser on the surface species was negligible. All the kinetic data reported hereafter were obtained using this spin rate.

3.3.2. Steady State Kinetics

The effects of reaction temperature and ozone partial pressure on the decomposition rate and surface coverage of the peroxide species were examined under steady state conditions. The steady state rate was found to increase with increasing ozone partial pressure and increasing temperature (Figure 3.2), as expected. The reaction order on ozone partial pressure was found to be slightly smaller than 1 (0.94) independent of temperature.

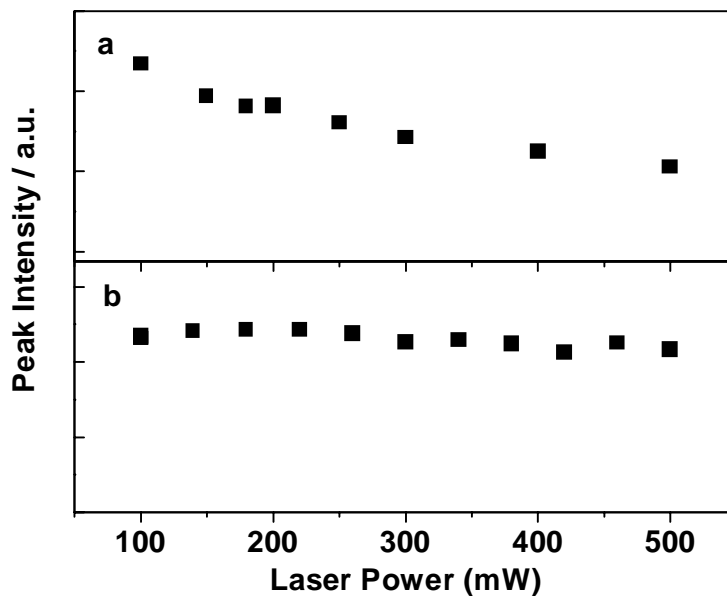


Figure 3.1. Effects of laser power (at the laser source) and sample spin rate on the Raman signal intensity of the observed peroxide species. $T = 300\text{ K}$, 2 mol% ozone in oxygen ($1000\text{ cm}^3\text{ min}^{-1}$), slid width = $50\text{ }\mu\text{m}$ (resolution = $\sim 6\text{ cm}^{-1}$). (a) sample spin rate = 800 rpm; (b) sample spin rate = 1000 rpm.

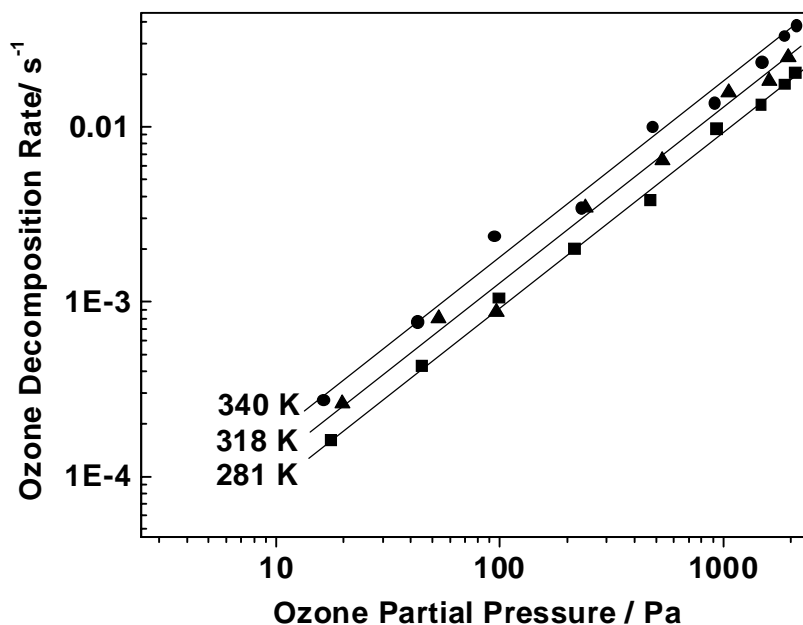


Figure 3.2. Effects of temperature and ozone partial pressure on ozone decomposition rate. Reactant flow rate = $1000\text{ cm}^3\text{ min}^{-1}$.

The surface coverage, θ , of the peroxide intermediate under reaction conditions was determined by integrating the peak intensity of the signal at 884 cm^{-1} in the Raman spectra and normalizing to the peak intensity at the lowest temperatures and highest ozone pressures, where saturation occurred. The surface coverage was determined at various reaction conditions and plotted as reaction isotherms (Figure 3.3). As expected for an adsorbed species, its surface coverage increased with increasing ozone partial pressure and decreased with increasing temperature.

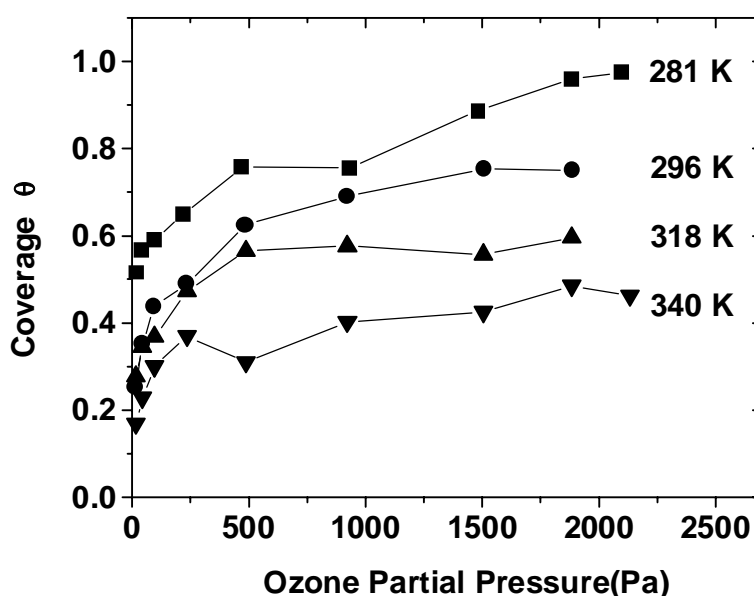


Figure 3.3. Reaction isotherms of the ozone decomposition reaction measured using *in situ* laser Raman spectroscopy. Spectral acquisition conditions: laser power = 100 mW, resolution = 6 cm^{-1} , exposure = 30 s, and 60 scans.

The Clausius-Clapeyron plot of the coverage data can be obtained by taking horizontal slices at fixed surface coverage of the peroxide intermediate (Figure 3.4). The slopes of the lines yield the differential or isosteric heat of reaction.

$$\Delta H = R \left(\frac{d \ln P}{d(1/T)} \right)_{\theta} \quad (3.1)$$

The isosteric heat of reaction was found to increase with coverage (Figure 3.5):

$$\Delta H / \text{kJ mol}^{-1} = -22 - 89\theta \quad (3.2)$$

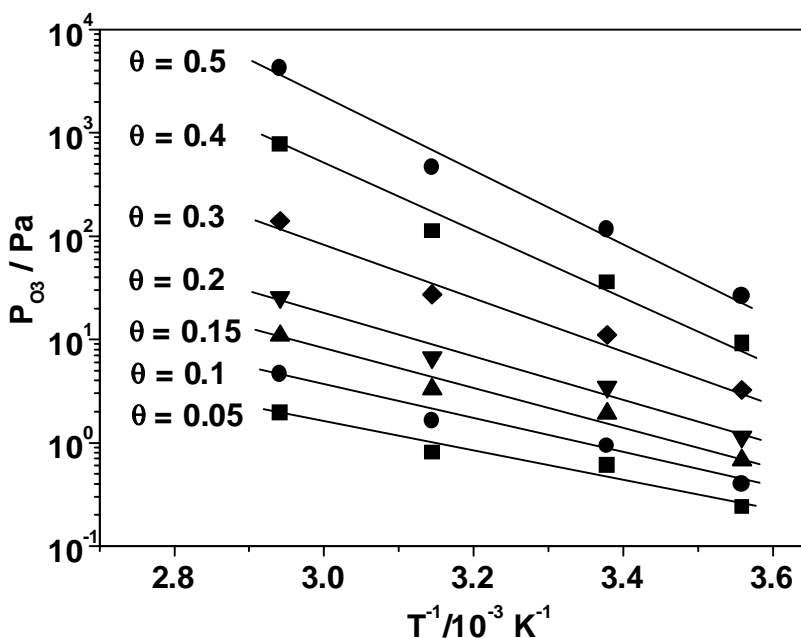


Figure 3.4. Clausius-Clapeyron plots of the coverage data obtained by taking horizontal slices at fixed surface coverage of the peroxide intermediate.

3.3.3. Transient Kinetics

To further gather information on the kinetic behavior of the adsorbed peroxide species, transient experiments were carried out to study the adsorption and desorption of this species separately. The transient adsorption experiments were initiated with a bare surface with no adsorbed peroxide species. Ozone was introduced suddenly and the Raman spectra were acquired at successive time intervals (~30s). The peak areas were integrated, and the coverages were calculated and plotted versus the elapsed time. Figure 3.6 presents a typical set of Raman signals for a transient adsorption experiment (inset) and the corresponding adsorption curve. Figure 3.7 shows the adsorption curves at various temperatures and ozone partial pressures. As expected, the adsorption process is faster at higher temperatures (Figure 3.7a) and at higher

ozone partial pressures (Figure 3.7b). Also the final coverage is higher for higher ozone partial pressures, in agreement with the steady state results.

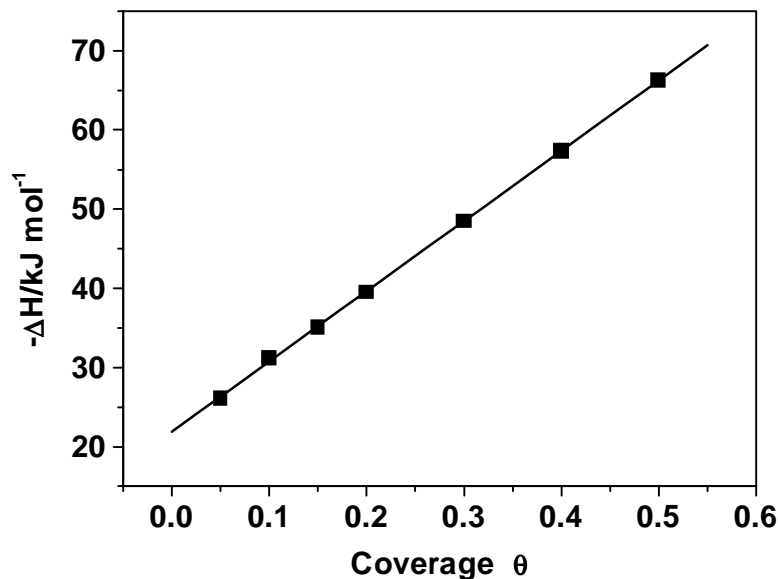


Figure 3.5. Dependence of isosteric heat of reaction on the surface coverage obtained from the slope of the Clausius-Clapeyron plots.

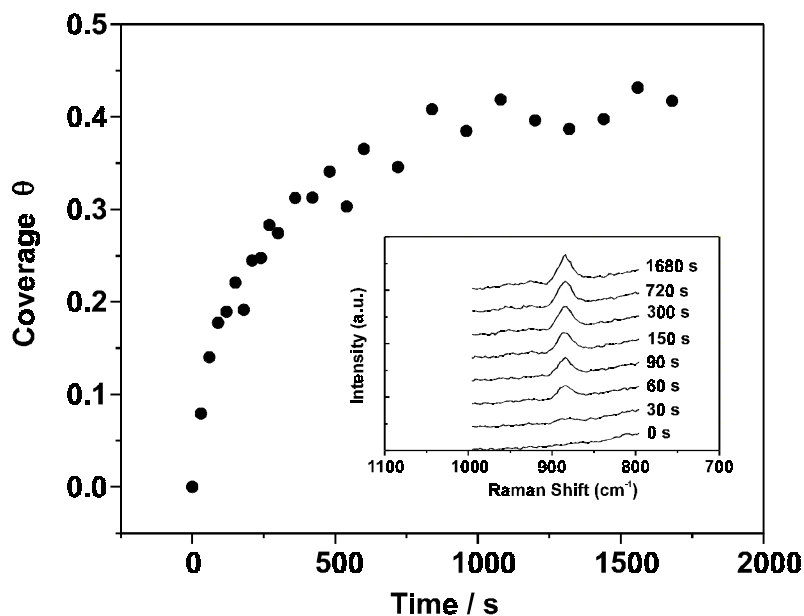


Figure 3.6. A typical set of Raman signals for a transient adsorption experiment (inset) and the corresponding adsorption curve. Laser power = 100 mW, resolution = 6 cm^{-1} , exposure = 20 s.

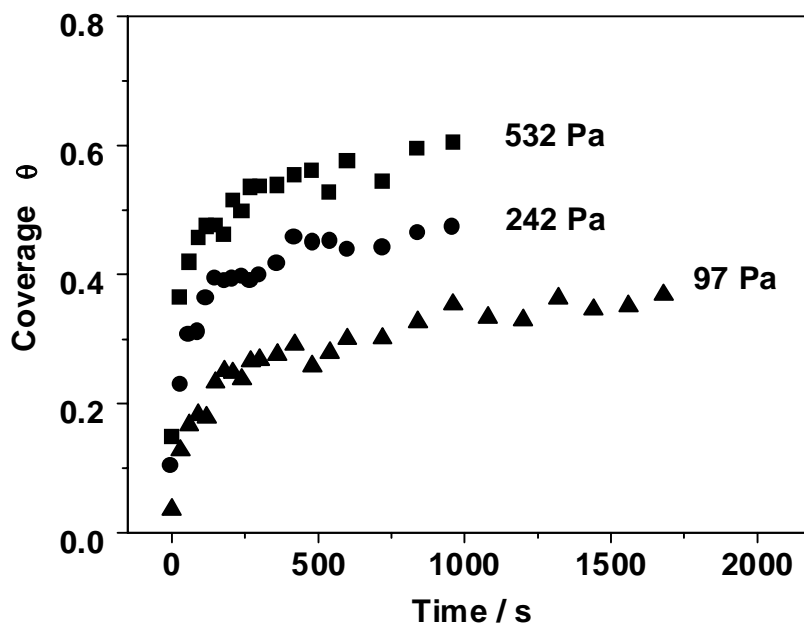
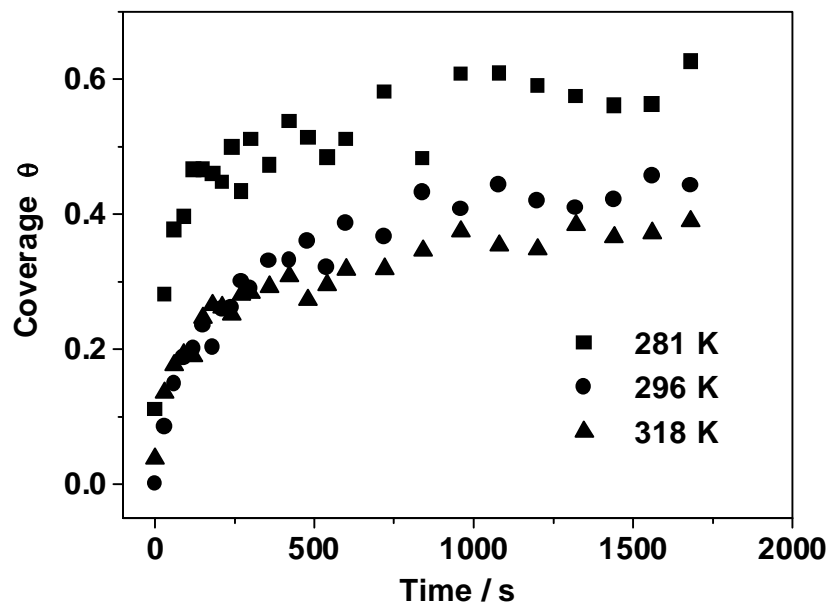


Figure 3.7. (a) Effect of temperature on the transient adsorption curve. Ozone partial pressure = 120 Pa, and spectral acquisition conditions are the same as in Figure 3.6. (b) Effect of ozone partial pressure on the transient adsorption curve. Temperature = 318 K, and spectral acquisition conditions are the same as in Figure 3.6.

The transient desorption experiments were carried out in a similar way as the adsorption measurements, except that the starting surface was preadsorbed with the peroxide species and the ozone was suddenly removed from the stream. Figure 3.8 shows the coverage versus time curves during desorption experiments at various temperatures. Again as expected, the desorption process is faster at higher temperatures.

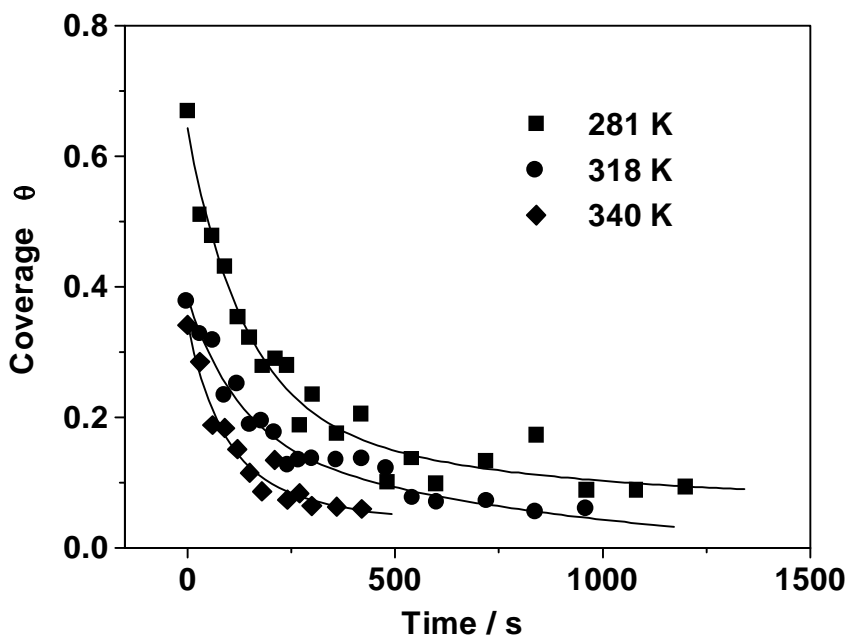


Figure 3.8. Effect of temperature on the transient desorption curve. Spectral acquisition conditions are the same as in Figure 3.6. The solid lines are fitted curves using $\theta = -\frac{1}{h} \ln(hk_d^0(t - t_0))$.

3.4. DISCUSSION

3.4.1. Steady State Kinetics

In chapter 2, a reaction sequence (Scheme 3.1) was proposed consisting of two kinetically significant steps: ozone adsorption to form a peroxide species (step 1), and desorption of the peroxide species to produce molecular oxygen (step 3). Both steps were taken to be irreversible. Evidence that the first step is irreversible is the absence of observed ozone at all conditions including temperature programmed desorption experiments, with only molecular oxygen

detected by mass spectrometry. Proof that the second step is irreversible are the observations that there was no oxygen partial pressure effect on the rate of decomposition⁴ and that the peroxide species was not detected when oxygen alone was present in the gas phase. If the adsorption of oxygen to form the peroxide intermediate were possible, then increasing its partial pressure would have increased the surface coverage and retarded the rate of adsorption of ozone, and consequently the rate of the overall reaction. This was not observed, and both steps can be considered to be substantially irreversible from a kinetic standpoint. It is recognized that no elementary step is completely irreversible.



Scheme 3.1. Proposed ozone decomposition mechanism

The first step also produces an atomically adsorbed oxygen species. Electron spin resonance experiments suggest that this is an O^- ion⁵. This atomic oxygen was found to react with a gaseous ozone molecule through a Rideal-Eley type reaction in a fast step to produce a peroxide species and gas phase molecular oxygen. The behavior of this atomic species is not kinetically significant, as it is produced as a byproduct in step 1, and is thereafter rapidly consumed in step 2. Therefore the reaction mechanism can be reduced to a two-step sequence, in which only the first and third steps are kinetically meaningful. This two-step sequence is checked against the kinetic results assuming both uniform and non-uniform surface models to fit the steady state decomposition data.

3.4.1.1. Uniform Surface Kinetic Analysis

If the surface of the catalyst were uniform, the reaction rate for ozone decomposition would have been given by $r = k_d\theta$, and would have been expected to be proportional to the surface coverage (θ) of the peroxide species. However, it can be clearly seen that this is not the case as

⁴ Dhandapani, B.; Oyama, S. T. *Chem. Lett.* **1995**, 413-414.

⁵ Oyama, S. T., unpublished results.

the rate is highly non-linear in coverage (Figure 3.9). Also the isosteric heat of reaction obtained from the Clausius-Clapeyron plot of the coverage data changes with coverage (Figure 3.5) indicating that a non-uniform surface treatment should be utilized.

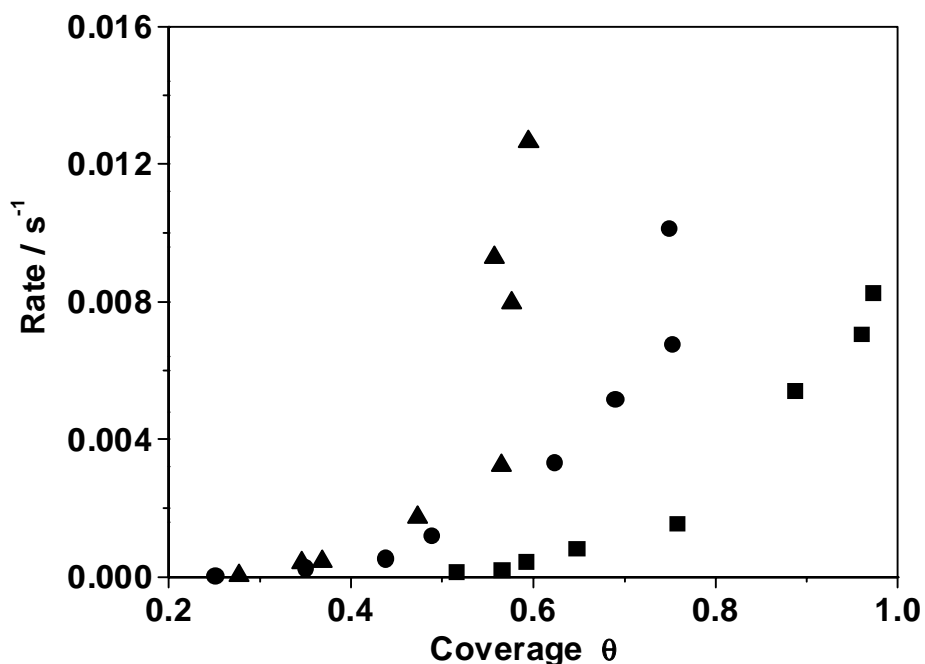


Figure 3.9. Plots of reaction rate versus surface coverage. A linear relationship is expected for the uniform surface model.

3.4.1.2. Non-Uniform Surface Kinetic Analysis

A non-uniform surface is a surface that has catalytic sites of different affinities for the reactant and/or the products⁶. The classic case of a non-uniform surface is that of an Fe catalyst for ammonia synthesis⁷. Details of the derivation of non-uniform surface kinetics can be found elsewhere⁸. In summary, for a surface with an activation energy for adsorption that increases linearly with coverage, i.e. $E_a = E_a^0 + gRT\theta$, the adsorption rate can be shown to be:

⁶ Boudart, M.; Djega-Mariadassou, G. *Kinetics of Heterogeneous Catalytic Reactions*; Princeton University Press: Princeton, N. J., 1984.

⁷ Brunauer, S.; Love, K. S.; Keenan, R. G. *J. Amer. Chem. Soc.* **1942**, *64*, 751.

⁸ (a) Langmuir, *J. Amer. Chem. Soc.* **1932**, *54*, 2798. (b) Kubokawa, Y. *Bull. Chem. Soc. Japan* **1960**, *33(6)*, 734. (d) Kubokawa, Y. *Bull. Chem. Soc. Japan* **1960**, *33(9)*, 1226. (e) Boudart, M.; Egawa, C.; Oyama, S. T.; Tamaru, K. *J. Chim. Phys.* **1981**, *78(11/12)*, 987.

$r_a = k_a^0(O_3) e^{-g\theta}$. This is known as the Elovich equation⁹. Here k_a^0 is the adsorption rate constant at zero coverage, and g is the proportionality constant for linear dependence of activation energy with coverage. Similarly, if the activation energy for desorption decreases linearly with coverage $E_d = E_d^0 - hRT\theta$, the desorption rate can be expressed as: $r_d = k_d^0 e^{h\theta}$, where k_d^0 is the desorption rate constant at zero coverage, and h is the proportionality constant for linear dependence of desorption activation energy with coverage. This is known as the Langmuir equation first derived for desorption from tungsten filaments⁸. At steady state, the rate is $r_{ss} = r_a = r_d$, from which the steady state coverage can be obtained. The rate, r_{ss} , is then derived by substituting the coverage into either of the two rate equations. In summary, this yields:

$$\theta_{ss} = \frac{1}{g+h} \ln \left[\frac{k_a^0(O_3)}{k_d^0} \right] \quad (3.3)$$

$$r_{ss} = k_d^0 \left[\left(\frac{k_a^0}{k_d^0} \right) (O_3) \right]^{\frac{h}{g+h}} \quad (3.4)$$

Scheme 3.2. Formulation of the steady state coverage and rate using a non-uniform surface model

From these expressions it follows that the steady state coverage should depend linearly on the logarithm of the ozone partial pressure, while the decomposition rate should depend on a fractional power $\left(\frac{h}{g+h} < 1 \right)$ of the ozone partial pressure. The experimental data were found to be well described by these expressions (Figs. 2, 10). It was also confirmed that the exponent in the power rate law expression did not vary with temperature (Figure 3.2). Also the decomposition rate increased only slowly with temperature. This is due to the small apparent activation energy for this reaction. The values of the parameters in the rate expression (Table 3.1) were obtained by carrying out a least square fitting of the steady state surface coverage and rate data using the equations in Scheme 2 (see Appendix D) and using $k_a^0 = A_a \exp(-E_a^0/RT)$

⁹ Aharoni, C.; Tomkins, F. C. *Advan. Catal.* **1970**, *21*, 1.

and $k_d^0 = A_d \exp(-E_d^0/RT)$. The exponent $\frac{h}{g+h}$ had a value of 0.94 in agreement with the experimental results.

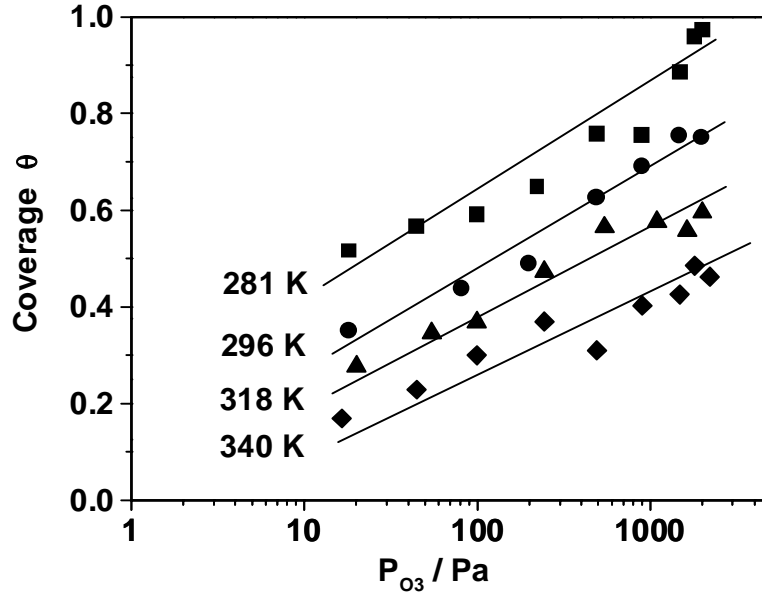


Figure 3.10. Plots for the surface coverage versus the logarithm of ozone partial pressure. A linear relationship is expected for the non-uniform surface case.

Table 3.1. Kinetic parameters of the non-uniform surface model

$g = 0.75$	$h = 11.8$
$k_a^0 / \text{cm}^3 \text{s}^{-1} = 3.1 \times 10^{-18} \exp\left(-\frac{6.2 \text{ kJ mol}^{-1}}{RT}\right)$	
$k_d^0 / \text{s}^{-1} = 1.6 \times 10^7 \exp\left(-\frac{69.0 \text{ kJ mol}^{-1}}{RT}\right)$	

Note that the proportionality constant for linear dependence of adsorption activation energy with coverage, g , was very small (0.75) compared to that of desorption, h (11.8). This indicates that the activation energy for adsorption does not change significantly with coverage, while the activation energy for desorption is strongly dependent on the surface coverage. Meanwhile the

activation energy at zero coverage E_a^0 was calculated to be 6.2 kJ mol^{-1} , suggesting that ozone adsorption on the catalyst surface is essentially not activated. This is consistent with the strong oxidizing nature of ozone. On the other hand, desorption of the adsorbed species was found to have an activation energy E_d^0 of 69.0 kJ mol^{-1} at zero coverage and the activation energy decreased considerably with increasing coverage. The obtained preexponential factor for adsorption A_a^0 ($3.1 \times 10^{-18} \text{ cm}^3 \text{ s}^{-1}$) was close to the values predicted by transition state theory¹⁰ ($10^{-10} - 10^{-17} \text{ cm}^3 \text{ s}^{-1}$). However, the obtained preexponential factor for desorption A_d^0 ($1.6 \times 10^7 \text{ s}^{-1}$) was significantly smaller than the predicted values ($10^{13} - 10^{17} \text{ s}^{-1}$). Since the preexponential factor can be expressed as $A = \frac{kT}{h} \exp(\Delta S^\ddagger/R)$, the value of ΔS_d^\ddagger was calculated to be $-107 \text{ J mol}^{-1} \text{ K}^{-1}$. The loss of entropy indicates that some degrees of freedom present in the reactants have been lost at the transition state. The calculated entropy change is in good agreement with the estimated value for two-dimensional translational motion of the peroxide species on the surface ($104 \text{ J mol}^{-1} \text{ K}^{-1}$, see Appendix B). It is possible that the adsorbed peroxide intermediate has free lateral two-dimensional translational motion, but loses it at the transition state, which must have motion perpendicular to the surface.

The obtained kinetic parameters are also in agreement with the observation that the isosteric heat of reaction increases with coverage (Figure 3.5). Note that this is opposite to the isosteric heat of adsorption for a non-uniform surface, which decreases with coverage. The reason for this is that the heat of reaction is the difference between the heat of ozone adsorption and the heat of peroxide desorption. The activation energy for ozone adsorption was found to be essentially independent of coverage, while the activation energy for peroxide desorption was found to increase significantly with coverage. According to the Polanyi-Horiuti relationship, the heat of reaction bears a proportionality to the activation energy of the reaction. Hence the heat of adsorption can be deduced to be almost independent of the coverage while the heat of desorption increases significantly with coverage. The net result is that the isosteric heat of reaction increases with coverage, as characteristic of a non-uniform surface.

¹⁰ (a) van Santen, R. A.; Niemantsverdriet, J. W. *Chemical Kinetics and Catalysis*, Plenum, New York, 1995. (b) Zhdanov, V. P.; Pavlicek, J.; Knor, Z. *Catal. Rev.-Sci. Eng.* **1989**, 30, 501.

To understand the origin of the non-uniformity of the surface, the uniqueness of manganese oxides should be considered. It is well known that manganese exists in several stable oxidation states (+2, +3, +4, +7)¹¹. A recent study of Al₂O₃-supported manganese oxide using electron spin resonance and diffuse reflectance spectroscopy¹² reported that the manganese species were present as a mixture of Mn²⁺, Mn³⁺, and Mn⁴⁺. The observation of Mn₃O₄ by Raman spectroscopy (Chapter 2) confirms that surface manganese on the catalyst is in mixed valence state compounds of Mn²⁺ and Mn³⁺. Hence, not only may the surface structure of the manganese oxides be different, but also the manganese species in various oxidation states can be expected to have different affinities to ozone, resulting in a kinetically and/or thermodynamically non-uniform surface.

3.4.2. Transient Kinetics

To unambiguously identify a surface species as a reaction intermediate rather than a passive spectator, it is essential to carry out dynamic measurements of the species and to relate its kinetic behavior to the overall steady state kinetics.

To calculate the adsorption and desorption rates from the transient data, a method first developed by Tamaru and coworkers is used¹³. The adsorption and desorption rates can be obtained by respectively differentiating the adsorption and desorption curves (Figs. 3.7, 3.8). An example of such a procedure is given at 318 K (Figure 3.11). For the desorption curves (since there is no readsorption), the rate of desorption is given directly from the slope of the θ versus t

plot, $r_2 = -\frac{d\theta}{dt}$. However, for the adsorption curves, the slope gives the net adsorption rate

$\frac{d\theta}{dt} = r_1 - r_2$ since O₂ is desorbing at the same time as adsorption is occurring. The absolute rate of adsorption, r_1 is then given by the slope of the adsorption plot plus the value of the desorption

rate $r_1 = \frac{d\theta}{dt} + r_2$. The latter is measured independently as just described, and taken at the same

value of coverage as the adsorption rate. These equations allow independent calculation of the

¹¹ Cotton, F. A.; Wilkinson, G. *Advanced Inorganic Chemistry*, 5th ed. Wiley: New York, 1988.

¹² Kijlstra, W. S.; Poels, E. K.; Bliëk, A.; Weckhuysen, B. M.; Schoonheydt, R. A. *J. Phys. Chem. B.* **1997**, *101*, 309.

¹³ H. Shindo, C. Egawa, T. Onishi, and K. Tamaru *J. Chem. Soc. Faraday I*, **1980**, *76*, 280.

rates of the two elementary steps. The results are shown in Figure 3.12. The adsorption curves are the three data sets that decrease with coverage, which as expected, attain higher values with increasing pressure. The desorption points, on the other hand, do not depend on pressure and increase with coverage.

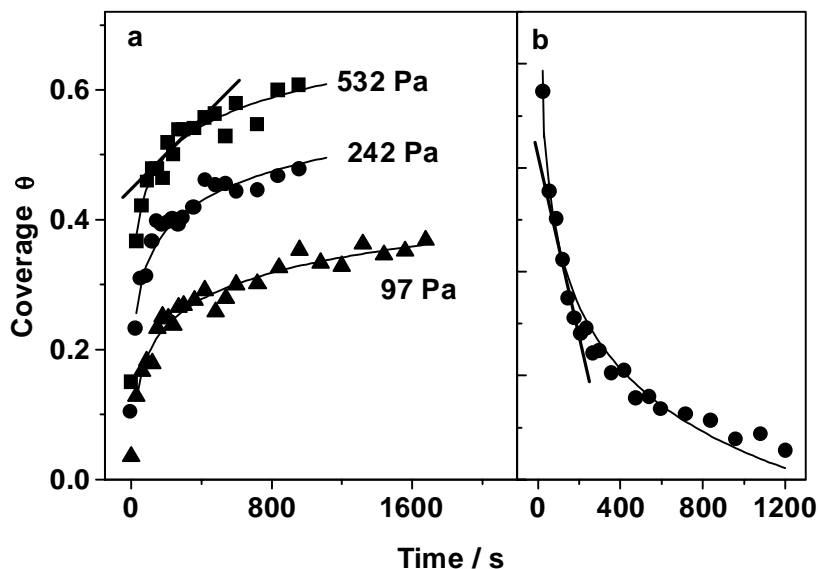


Figure 3.11. Calculation of adsorption and desorption rates from the transient results. (a) adsorption curves; (b) desorption curves. $T = 318 \text{ K}$, reactant flow rate = $1000 \text{ cm}^3 \text{ min}^{-1}$, response time $< 3 \text{ s}$. Spectral acquisition conditions: Laser power = 100 mW , resolution = 6 cm^{-1} , exposure = 20 s . The adsorption and desorption rates can be calculated from the slope of the curves as shown.

At steady state the rate of adsorption equals to the rate of desorption, and the steady-state points can be obtained at the intersections of the adsorption and desorption curves (Figure 3.12). Hence the intersections between the adsorption and desorption curves give the surface coverages at steady state conditions. The so-obtained steady state coverages at 318 K were compared with those measured in the steady state experiments (Table 3.2), and an excellent agreement was obtained. This result demonstrates that the transient kinetic data are consistent with the steady state data and are in support of the proposed reaction sequence. A further confirmation can be obtained if the surface reaction rate calculated using the transient data agrees with the measured steady state rate of overall reaction.

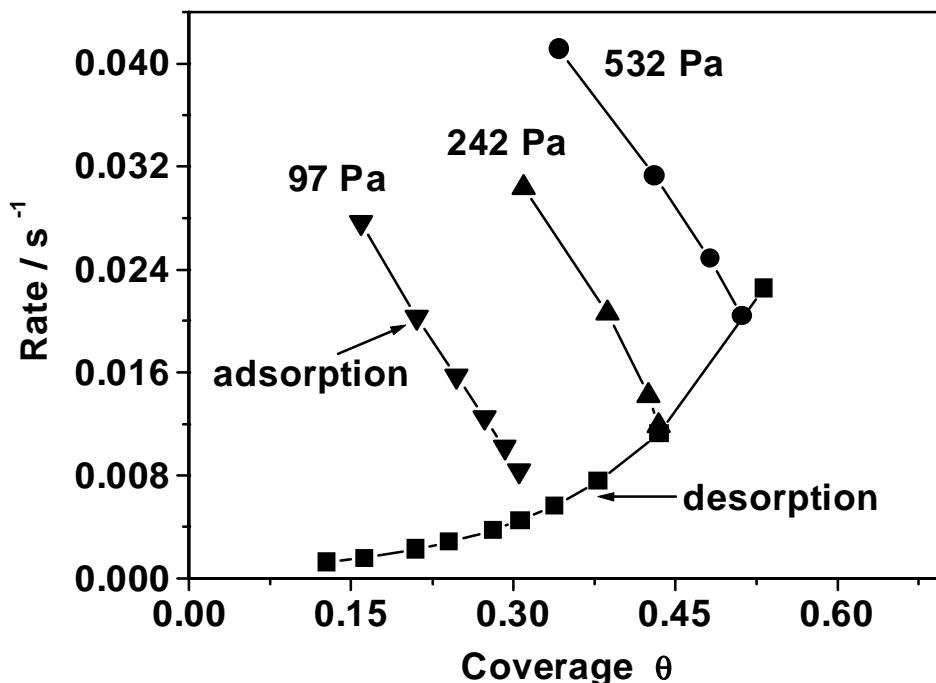


Figure 3.12. Transient adsorption and desorption rates versus surface coverage. Conditions are the same as in Figure 12. The desorption rate (squares) is independent of the pressure and increases with surface coverage. The adsorption curves are the three data sets (circles, up triangles, and down triangles) that decrease with coverage and which rise to higher values as the pressure increases. The intersections of the curves correspond to the steady state coverages.

If the proposed sequence accurately describes the reaction mechanism, the results obtained from the transient experiments should be consistent with those measured at steady state conditions. That is: the kinetic parameters derived from the transient results should be able to describe the steady state data, and vice versa.

Table 3.2. Comparison of the Steady-State Coverage Obtained from Transient and Steady-State Experiments: T = 318 K

<i>O₃</i> Pressure / Pa	97		242		532	
Method	TR	SS	TR	SS	TR	SS
Steady State Coverage	0.34	0.35	0.45	0.44	0.56	0.58

According to the non-uniform surface analysis, the rate of adsorption can be expressed as $r_a = k_a^0(O_3) e^{-g\theta}$, and the rate of desorption can be written as $r_d = k_d^0 e^{h\theta}$. For the desorption curve (since there is no readsorption), the rate of desorption is given directly from the slope of the θ vs. t plot, $r_d = -d\theta/dt$. Because $r_d = k_d^0 \exp(h\theta)$, by integration it is obtained that

$$\theta = -\frac{1}{h} \ln(hk_d^0(t - t_0)) \quad (3.5)$$

Where $t_0 = 1/(hk_d^0 e^{h\theta_0})$ and θ_0 is the initial coverage. By curve fitting the transient desorption data (Figure 3.8) using Eq. 3.5, values of h and k_d^0 can be determined from the desorption curve. The actual procedure consists of two steps. First, desorption curves at different temperatures were fitted to obtain h values. The obtained h values were averaged to determine a temperature independent value of h since h should not be a function of temperature. The average value of h was calculated to be 9.7, which is close to the value determined from the steady state results ($h = 11.8$). Second, this h value of 9.7 was used to curve fit the desorption data to obtain k_d^0 values at various temperatures. The so-obtained k_d^0 values are shown in the Arrhenius plot along with the k_d^0 values acquired from the steady state results (Figure 3.13). The desorption rate can also be calculated at the steady state coverage and Fig 3.14 shows the calculated desorption rates and the measured overall decomposition rates at steady state coverages. The transient kinetic results exhibit a good agreement with the steady state data, and a new set of kinetic parameters can be obtained through a combined linear regression of k_d^0 values from the steady state and transient results.

A further confirmation can be obtained if the kinetic parameters obtained from the steady state results (Table 3.1) can be used to predict the transient kinetics. This can be done for the desorption curves whose rate expression can be integrated analytically. As discussed earlier (Eq. 3.5), for the desorption data in the transient curves, $\theta = -\frac{1}{h} \ln(hk_d^0(t - t_0))$. So the transient desorption curve can be calculated using the values of h and k_d^0 derived from the steady state results (Table 3.1), and the results (solid lines) are plotted in Figure 3.15 along with the measured curves (symbols). Clearly the transient desorption kinetics are well described by the kinetic parameters obtained from the steady state results. Since the transient and steady state

data were measured in separate experiments, this serves as an independent check for the validity of the proposed reaction sequence.

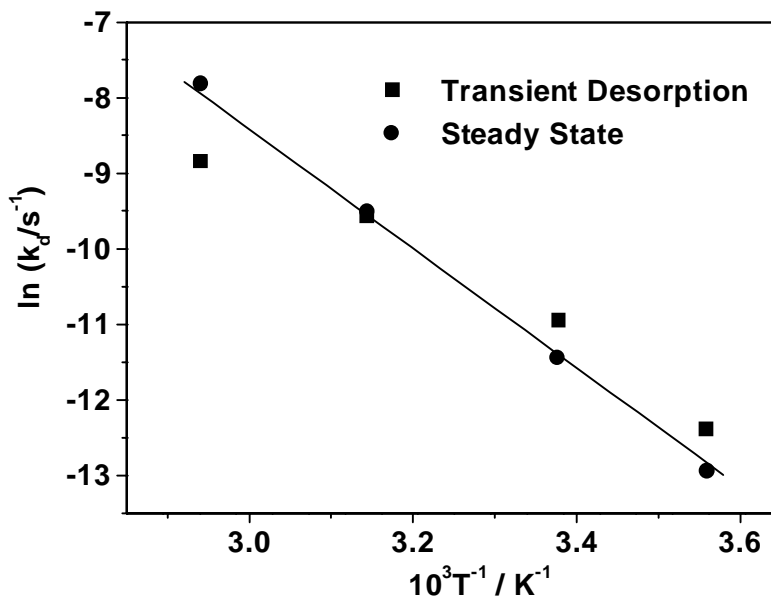


Figure 3.13. Arrhenius plots of k_d values calculated from the steady state and transient desorption results.

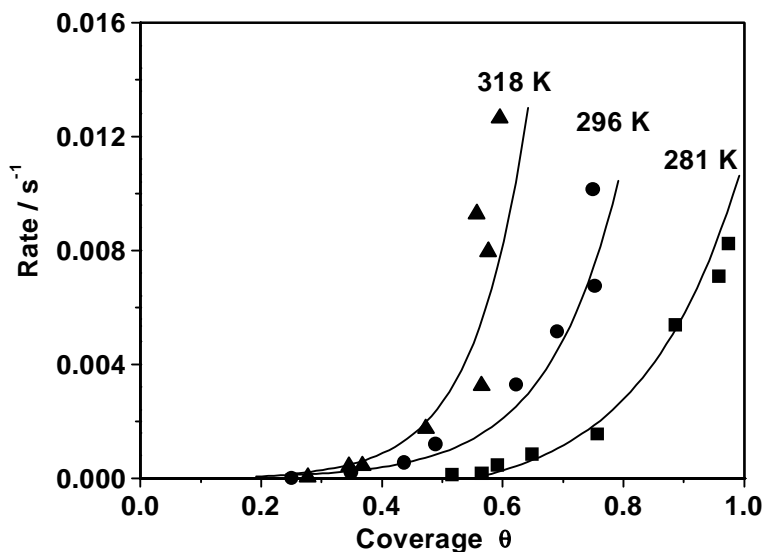


Figure 3.14. Comparison of measured steady state reaction rates (symbols) with the calculated curves (solid lines) using the kinetic parameters derived from the transient desorption data.

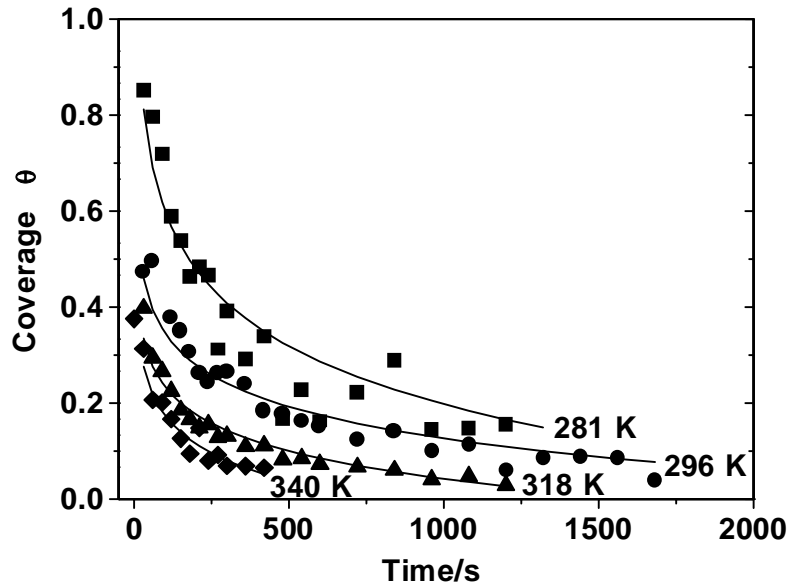


Figure 3.15. Comparison of measured transient desorption curves (symbols) with the calculated curves from the steady state kinetic parameters (solid lines).

3.5. CONCLUSIONS

The steady state and transient kinetics of the ozone decomposition reaction were investigated at temperatures from 281 to 340 K and ozone partial pressures from 4.7 Pa to 2.1 kPa. The reaction proceeded through two kinetically significant and irreversible steps, the adsorption of ozone on the catalyst surface and the desorption of a molecular oxygen (peroxide) species. The steady state kinetics was found to be well described by a non-uniform surface treatment. Ozone adsorption had a low activation energy of 6 kJ mol^{-1} , while the desorption of the peroxide species had an activation energy of 69 kJ mol^{-1} at full surface coverage and increased with decreasing surface coverage. The overall rate of the reaction is given by a balance between the rates of adsorption of ozone and desorption of the peroxide species. Transient adsorption and desorption experiments of the peroxide species, in combination with steady state kinetic measurements, confirms its role as a reaction intermediate in ozone decomposition reaction. The kinetic parameters derived from the transient desorption experiments are in a good agreement with those

obtained from the steady state measurements, indicating that the proposed steps accurately describe the reaction sequence.

CHAPTER 4. ETHANOL OXIDATION USING OZONE

4.1. INTRODUCTION

This chapter presents a mechanistic study of ethanol oxidation using ozone on supported manganese oxide catalysts. Ozone has been attracting increasing attention recently as an alternative oxidant in the oxidation of volatile organic compounds (VOCs) due to its strong oxidizing ability and hence lower reaction temperatures¹⁴⁻²⁰. However, research work in this area has been limited, in particular, fundamental work on the kinetics and reaction mechanism has been scarce.

As expected, ozone was generally found to be effective at enhancing the conversion of VOCs, especially at low temperatures. The kinetics of complete oxidation of benzene by ozone on MnO₂ was investigated by Naydenov and Mehandjiev. They found that the activation energy for benzene oxidation with ozone (30 kJ mol⁻¹) was much lower than that with oxygen (88 kJ mol⁻¹), and was similar to that of ozone decomposition (32 kJ mol⁻¹). It was concluded that the rate determining step for benzene oxidation by ozone was ozone decomposition. Klimova *et al.* studied the oxidation of lower aliphatic alcohols by ozone over silica and alumina. It was found that the main products of the oxidation reactions were: acetaldehyde and carbon dioxide from ethanol, propionaldehyde and carbon dioxide from *n*-propanol, and acetone from isopropanol. It was determined that for the oxidation of 1 mole of the alcohols about 1 mole of ozone or less was consumed. By varying the reactor volume while keeping a constant surface area of the catalyst it was demonstrated that the reaction proceeded primarily on the catalyst surface.

14. Gervasini, A.; Vezzoli, G. C.; Ragaini, V. *Catal. Today* **1996**, 29, 449.

15. Gervasini, A.; Bianchi, C. L.; Ragaini, V. in *Environmental Catalysis*, J.N. Armor (Ed.), *ACS Symp. Ser.* 552; ACS: Washington, DC, **1994**, 352.

16. Li, W.; Oyama, S. T. in *Heterogeneous Hydrocarbon Oxidation*, B.K. Warren and S.T. Oyama (Eds.), *ACS Symp. Ser.* 638; ACS: Washington, DC, **1996**, 364.

17. Klimova, M. N.; Tarunin, B.I.; Aleksandrov, Yu. A. *Kinet. Katal.* **1988**, 26, 1143.

18. Hauffe, K.; Ishikawa, Y. *Chem. Ing. Techn.* **1974**, 5, 1035.

19. Ragaini, V.; Bianchi, C. L.; Forcella, G.; Gervasini, A. in *Trends in Ecological Physical Chemistry*, Bonati, L. (eds.) Elsevier: Amsterdam, **1993**, 275.

20. Naydenov, A.; Mehandjiev, D. *Appl. Catal.* **1993**, A 97, 17.

Spectroscopic study of ozone oxidation reactions has been rare²¹, and no work has been done under reaction conditions.

This chapter reports a comparative study of the ethanol oxidation reaction with an ozone/oxygen mixture or oxygen alone over supported manganese oxide catalysts using *in situ* laser Raman spectroscopy coupled with reactivity measurements. Alumina and silica supported manganese oxide catalysts were chosen because manganese oxide is an excellent catalyst for complete oxidation, while the alumina supported catalyst has a significantly higher activity for ozone decomposition than the silica supported sample.

4.2. EXPERIMENTAL

4.2.1. Catalyst Preparation and Characterization

Alumina and silica supported MnO₂ catalysts were prepared by incipient wetness impregnation of supports (Degussa, Aluminoxide C and Cabosil L-90) using manganese acetate (Aldrich) as the precursor and were calcined in air at 773 K for 3 h prior to use. The crystal phases of MnO₂ in the catalysts were identified using X-ray diffraction (XRD) and their surface areas were determined by N₂ physisorption using the BET method.

4.2.2. In Situ Laser Raman Spectroscopy

The *in situ* laser Raman spectroscopic studies were carried out with a high throughput spectrometer using a Raman sample cell (Figure 4.1), which allowed the spectrum to be acquired under reaction conditions. The catalysts (200 mg) were pressed into thin wafers 15 mm in diameter and about 1 mm in thickness, and were held on a ceramic rod by a stainless steel cap. The rod was spun at 1800 rpm to avoid local overheating by the laser. The temperature was controlled by a programmable temperature controller (Omega, CN2010), and was measured by a thermocouple placed 3 mm away from the sample. The details of the laser Raman spectrometer were described in Chapter 2.

21. Marley, L.; Lamotte, J.; Lavalley, J.C.; Tsyganenko, N.M.; Tsyganenko, A. A. *Catal. Lett.* **1996**, *41*, 209.

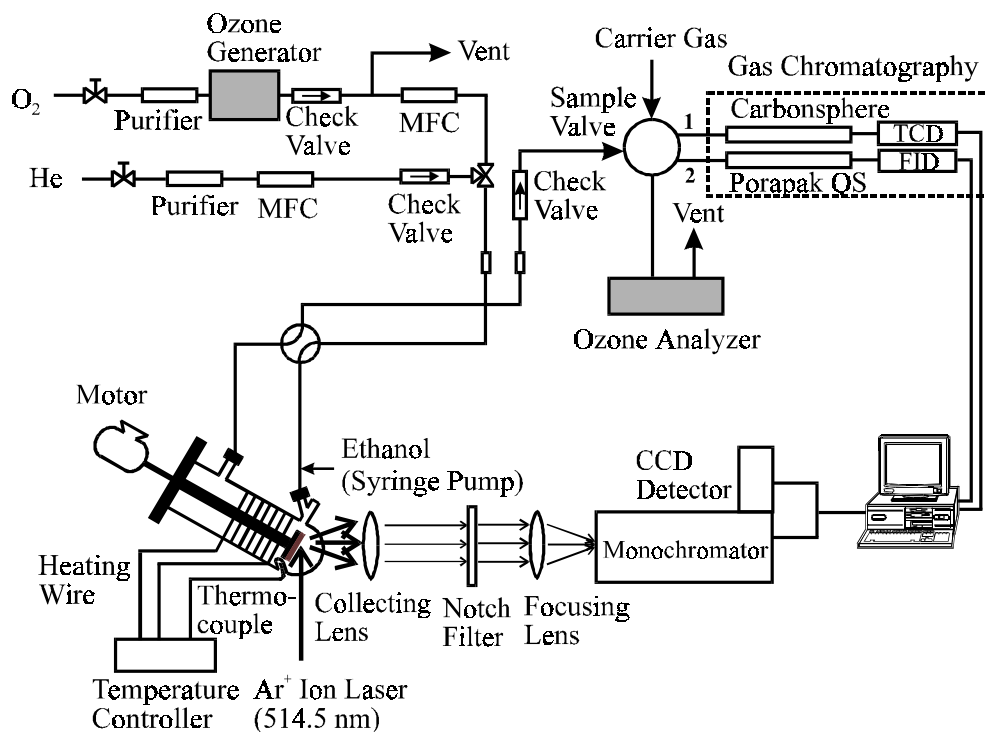


Figure 4.1. Schematic of the *in situ* laser Raman system for ethanol oxidation

Three sets of reactivity tests were performed on the catalysts: ethanol oxidation using an ozone/oxygen mixture, using oxygen alone, and ozone decomposition. The samples were pretreated *in situ* at 773 K in oxygen for 2 h before each set of measurements. The reaction feed for oxidation using an ozone/oxygen mixture contained 7.8 mol% oxygen, 0.16 mol% ozone, 0.8 mol% ethanol with helium as balance, and the total flow rate was $110 \text{ cm}^3 \text{ min}^{-1}$ ($82 \text{ } \mu\text{mol s}^{-1}$). For the oxidation using oxygen alone, the feed composition was essentially the same except that no ozone was used and the total flow rate was kept at $110 \text{ cm}^3 \text{ min}^{-1}$ by increasing the flow rate of oxygen. For ozone decomposition, no ethanol was injected into the stream and the total flow rate was kept at $110 \text{ cm}^3 \text{ min}^{-1}$ by increasing the flow rate of helium. Some bypassing of the gas around the sample likely occurred, but the rate data should be accurate for conversions of 10% or less (differential conditions).

Ozone was produced by passing oxygen (Air Products, Extra Dry, > 99.6%) through a corona-discharge ozone generator (OREC, Model V5-0), and the inlet, and outlet ozone concentrations were measured using a UV absorption ozone monitor (*Safety Caution: Ozone is highly toxic, hence leak checking and purification of the exhaust stream with an ozone*

decomposition filter should be carried out.) The reaction products were analyzed by an on-line gas chromatograph (SRI, 8610C) equipped with thermal conductivity and flame ionization detectors. Separation of O₂, CO, and CO₂ was achieved by a Carbosphere column (Alltech) while separation of organic compounds was carried out with a Porapak QS column (Alltech).

4.3. RESULTS

4.3.1. Catalyst Characterization

Although both alumina and silica supported catalysts had 10 wt% loading of manganese oxide, they exhibited considerably different MnO₂ crystallinity (Figure 4.2). The alumina supported catalyst essentially only had a well-dispersed manganese oxide phase, the silica supported sample showed strong diffraction peaks due to crystalline manganese oxide (β -MnO₂, JCPDS 24-735). The surface area of the alumina and silica supported catalysts was found to be 88 and 75 m² g⁻¹, respectively.

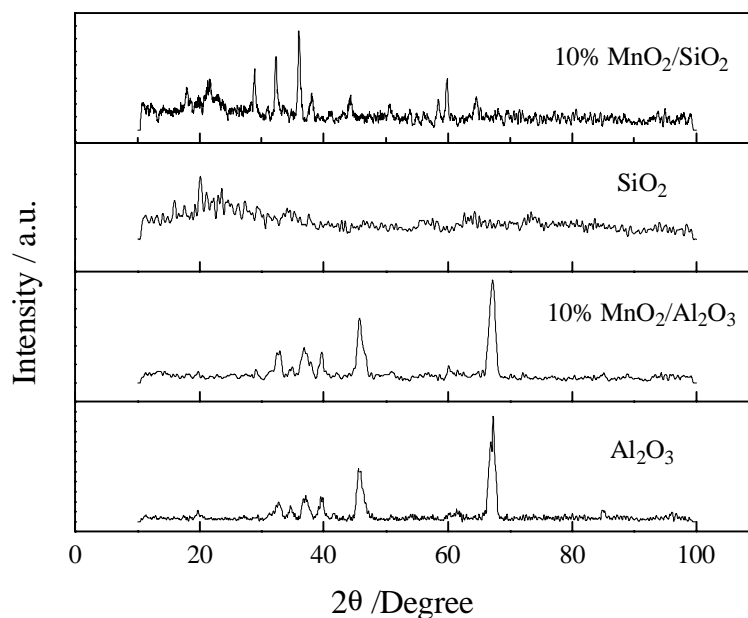


Figure 4.2. XRD patterns of the supported MnO₂ catalysts and the supports

4.3.2. Ethanol Oxidation Reactivity

As expected, ethanol was found to be more reactive with ozone than with oxygen (Figure 4.3), especially at low temperatures. The reactivity difference became less significant at higher temperatures, and eventually disappeared above 500 K. $\text{MnO}_2/\text{SiO}_2$ showed similar behavior (Figure 4.4), however, the reactivity difference between ozone and oxygen was more pronounced in this case, and only disappeared around 530 K. For both catalysts CO_2 and H_2O were the main products, with a small amount of CO produced at higher temperatures (> 450 K), and no organic products were detected.

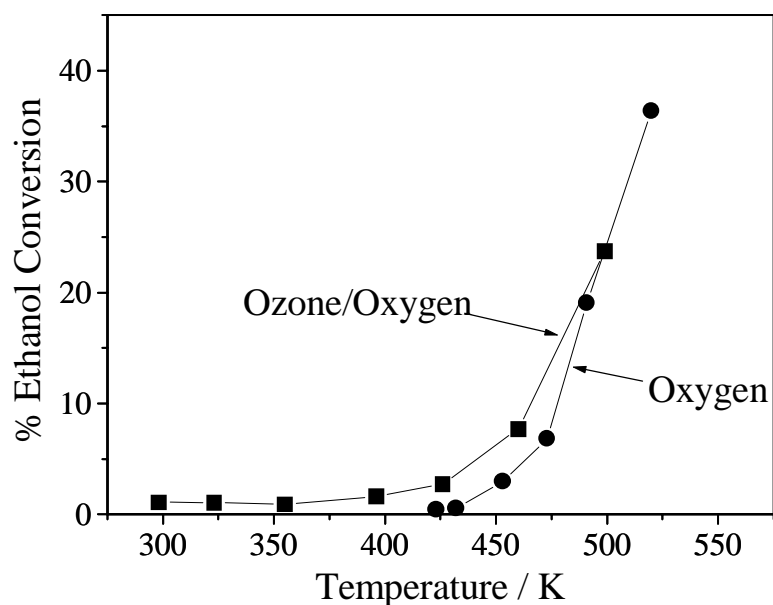


Figure 4.3. Ethanol oxidation reactivity using O_3 or O_2 on $10\% \text{MnO}_2/\text{Al}_2\text{O}_3$

The measurements of inlet and outlet ozone concentrations allowed the calculation of the ratio of converted ozone to converted ethanol (Figure 4.5).

$$\frac{\text{Converted Ozone}}{\text{Converted Ethanol}} = \frac{\% \text{Ozone Conversion} \times \text{Ozone Feed Rate}}{\% \text{Ethanol Conversion} \times \text{Ethanol Feed Rate}} \quad (4.1)$$

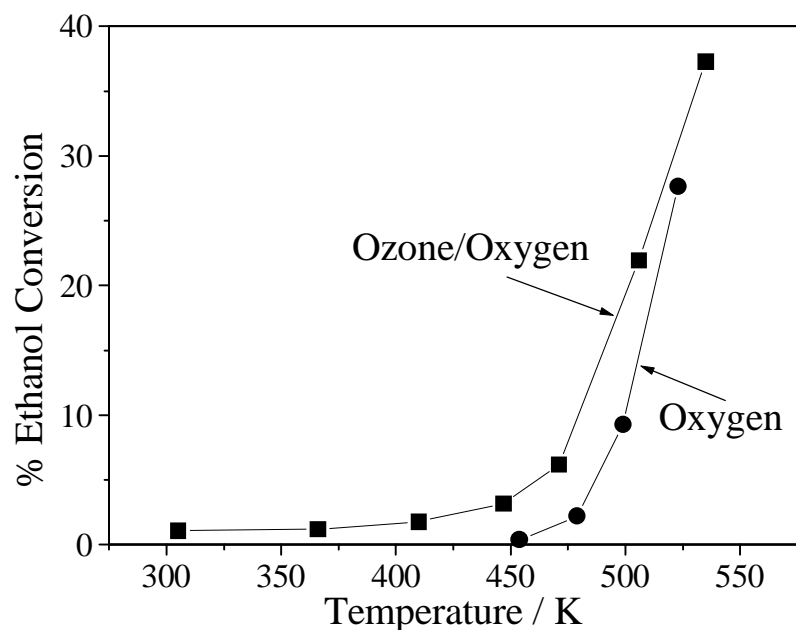


Figure 4.4. Ethanol oxidation reactivity using O_3 or O_2 on 10% MnO_2/SiO_2 .

This ratio were found to decrease from 14 - 10 at 300 K to below unity at > 500 K (not shown). However, the values at higher temperatures could be misleading because the reaction between ethanol and oxygen started to occur (Figure 4.3). The ratio on the silica-supported sample was slightly higher than that on the alumina-supported catalyst.

The reaction turnover rates on MnO_2/Al_2O_3 were calculated based on 70% dispersion of manganese oxide estimated from its X-ray diffraction results. Activation energies of ethanol oxidation using oxygen and an ozone/oxygen mixture were calculated from the Arrhenius plots of the turnover rates (Figure 4.6). The activation energy was much higher (89 kJ mol^{-1}) when oxygen alone was used as the oxidant than when an ozone/oxygen mixture was used. In the latter case the activation energy was only 3.7 kJ mol^{-1} at lower temperatures (< 400 K), and 48 kJ mol^{-1} at higher temperatures (> 400 K).

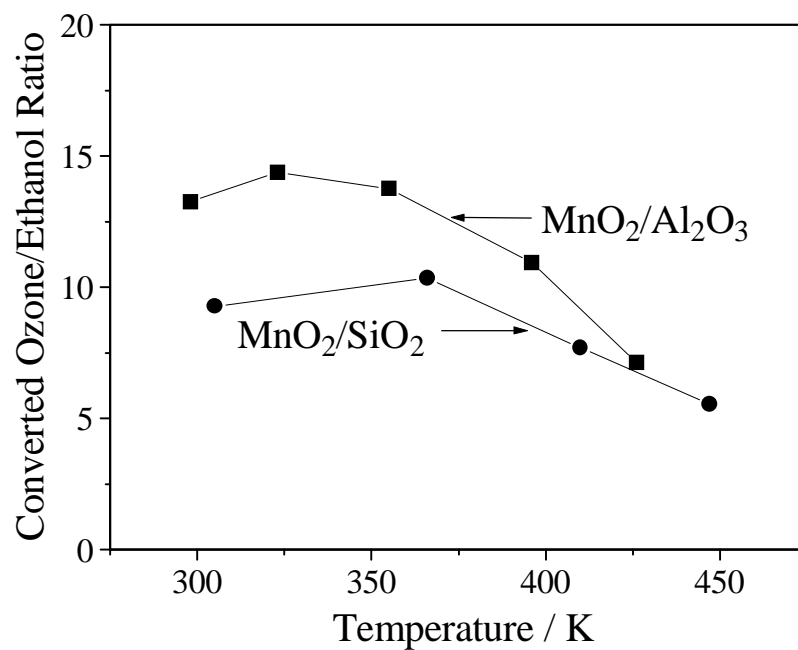


Figure 4.5. Converted ozone to ethanol ratio on the supported MnO₂ catalysts

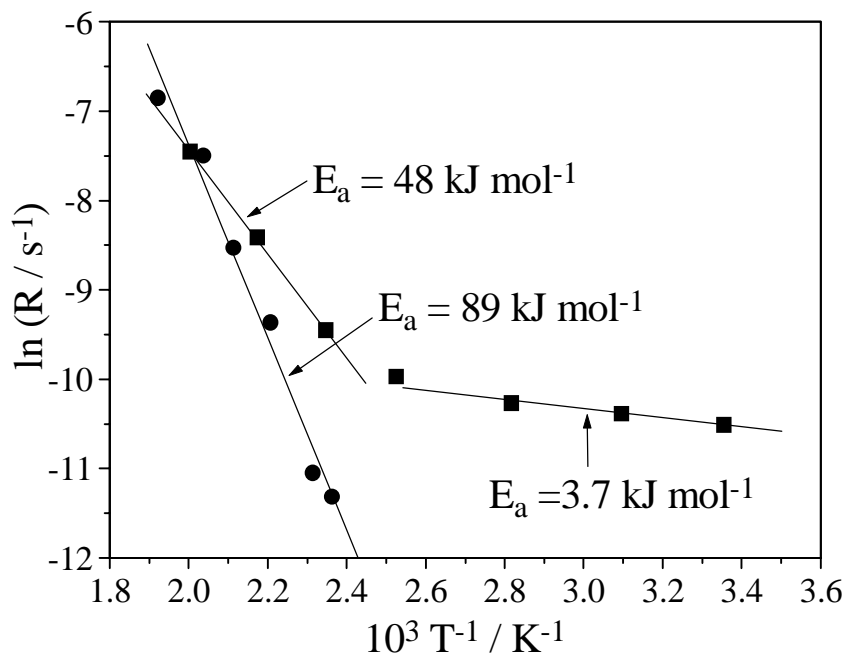


Figure 4.6. Arrhenius plots of the turnover rate of ethanol oxidation on MnO₂/Al₂O₃

4.3.3. In Situ Laser Raman Spectroscopic Studies

The Raman spectra of the catalyst samples were compared under various conditions (Figure 4.7). The spectrum under oxygen exhibited a broad signal peaking at 658 cm^{-1} (Figure 4.7a). With the introduction of ozone without ethanol the 658 cm^{-1} peak shifted to 634 cm^{-1} and a new sharp signal at 884 cm^{-1} appeared (Figure 4.7b). When ethanol was introduced in the absence of ozone, a new species with Raman signals at 878 , 2878 , 2930 , 2970 cm^{-1} was observed which was assigned²² to an adsorbed ethoxide species (Figure 4.7c). When ethanol and ozone were passed over the catalyst together (Figure 4.7d), the intensity of both the new signal at 878 cm^{-1} and the ethoxide species decreased dramatically, and the signal at 658 cm^{-1} shifted to 640 cm^{-1} .

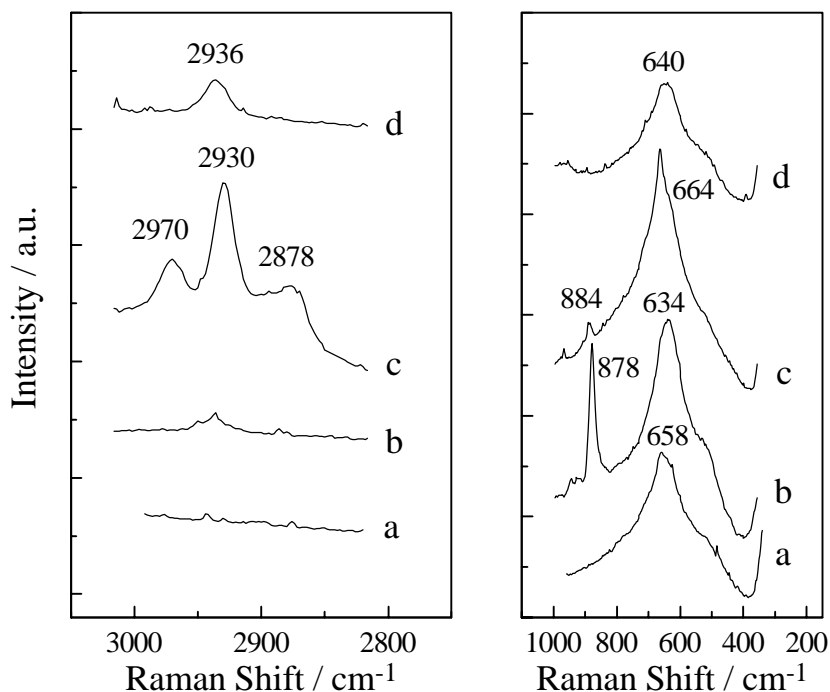


Figure 4.7. Raman spectra of 10% MnO₂/Al₂O₃ sample under various conditions (a. oxygen; b. ozone; c. ethanol; d. ethanol and ozone).

In addition to steady state experiments, transient measurements were also performed on the alumina-supported catalyst to investigate the interaction between the adsorbed species. The transient experiments were carried out by starting with a surface with preadsorbed ethoxide species. Ozone was then suddenly introduced and a set of Raman spectra was acquired at regular

time intervals. The intensity of the 884 cm^{-1} peak increased with time, while the adsorbed ethoxide peaks in the higher wavenumber region ($2800 - 3200\text{ cm}^{-1}$) decreased with time (Figure 4.8).

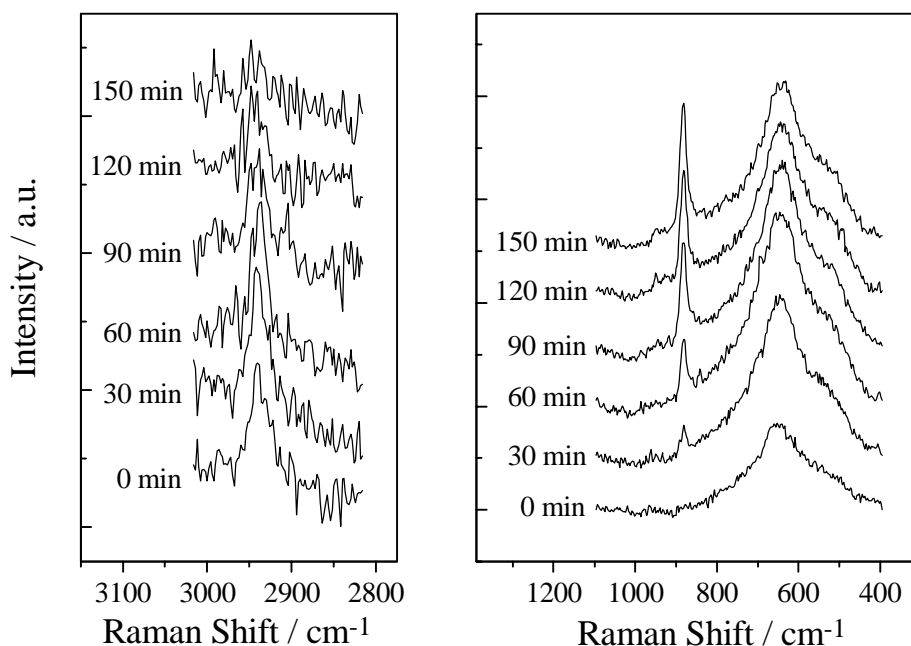


Figure 4.8. Transient experiment Raman spectra on 10% $\text{MnO}_2/\text{Al}_2\text{O}_3$.

4.3.4. Ozone Decomposition

Ozone decomposition reactivity was measured to investigate its role in the ethanol oxidation reaction (Figure 4.9). On $\text{MnO}_2/\text{Al}_2\text{O}_3$, with increasing temperatures ozone conversion increased slowly at temperatures $< 400\text{ K}$, then increased sharply above 400 K , and finally approached 100% around 500 K . While on $\text{MnO}_2/\text{SiO}_2$, ozone conversion was lower at low temperatures ($< 320\text{ K}$), but steadily increased with increasing temperatures, and reached 100% at a similar temperature (500 K) as on $\text{MnO}_2/\text{Al}_2\text{O}_3$. The turnover rates on $\text{MnO}_2/\text{Al}_2\text{O}_3$ were also calculated assuming 70% dispersion of manganese oxide, and the Arrhenius plot showed two kinetic regions (Figure 4.10). The lower temperature region, which was dominated by the catalytic decomposition on MnO_2 , gave an activation energy of 3.2 kJ mol^{-1} , while the higher temperature

²². Zhang, W.; Oyama, S.T. *J. Phys. Chem.* **1995**, *99*, 19468.

region which was dominated by the gas phase decomposition gave an activation energy of 41 kJ mol⁻¹.

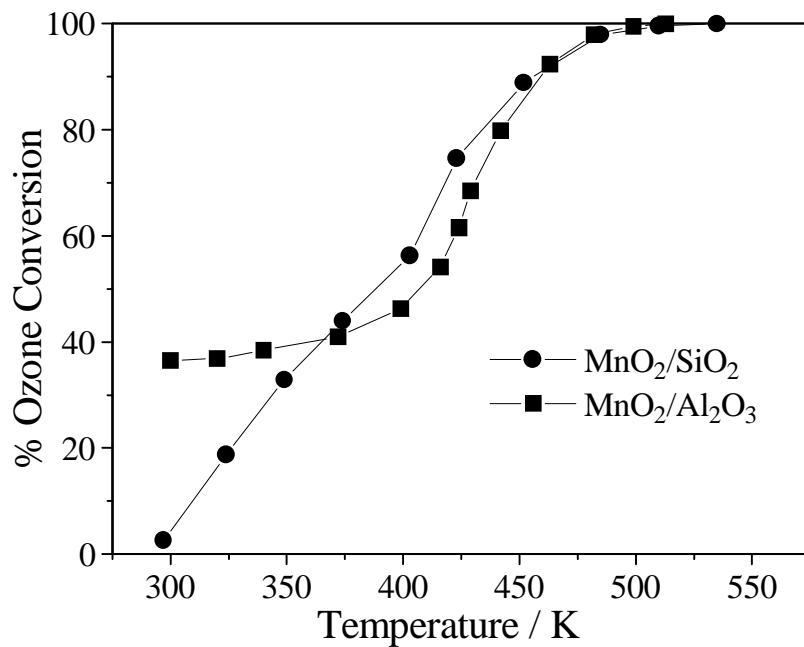


Figure 4.9. Ozone decomposition reactivity on supported MnO₂ catalysts

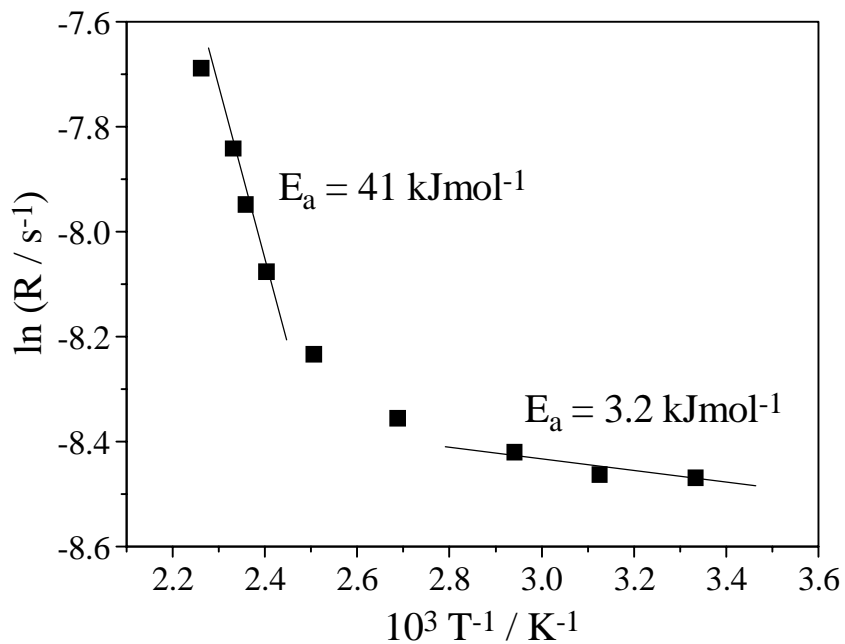


Figure 4.10. Arrhenius plots of turnover rate of ozone decomposition on MnO₂/Al₂O₃

4.3.5. Kinetic Measurements

The rate of ethanol oxidation using ozone was measured on the alumina-supported manganese oxide catalyst at temperatures from 363 to 453 K and with ozone concentrations varying from 0.05 to 0.20 mol m⁻³ and ethanol concentration varying from 0.25 to 0.73 mol m⁻³. The results are given in Appendix E, and can be described as a power law equation using the least square fitting technique described in details in Appendix F.

The rate of ethanol conversion was found to be well described by a power law equation:

$$r = 6.2 \exp\left(-\frac{11.8\text{kJ mol}^{-1}}{RT}\right) C_{\text{O}_3}^{0.89} C_{\text{C}_2\text{H}_5\text{OH}}^{0.81} \quad (4.2)$$

4.4. DISCUSSION

4.4.1. Reaction Stoichiometry

For most reactions, reaction stoichiometry is easy to determine, however, this is not the case for oxidation reactions using ozone. One reason is that it is not clear whether oxygen is also involved in the reaction as ozone is usually used as an ozone/oxygen mixture. Another reason is that it is uncertain how many oxygen atoms of each ozone molecule contribute to the oxidation reaction. If only ozone is involved in the reaction, the reaction equation can be written as (assuming only CO₂ and H₂O are produced):



However, when each ozone molecule only contributes one oxygen atom while producing an oxygen molecule, the reaction equation becomes:



In addition to these reactions the ozone decomposition reaction may occur independently.



By measuring the inlet and outlet ozone concentrations, the converted ozone to ethanol ratio can be determined, and this ratio may give insight on the reaction stoichiometry. The low value of the ratio at high temperatures (> 400 K) was consistent with a significant involvement of molecular oxygen in the reaction. In other words, ethanol could initially be activated by ozone to form intermediate oxidation products (aldehydes, carboxylic acids, etc.), and these could

subsequently be oxidized by oxygen. At even higher temperatures (> 500 K), the oxidation was likely dominated by oxygen as indicated by the higher activation energy of ethanol oxidation by oxygen compared to that by ozone. This was probably due to the rapid decomposition of ozone. At lower temperatures when the oxygen involvement was probably low, the measured ratios ranged from 10 to 20, which were closer to the stoichiometry of equation 3. The measured ratio on the silica supported catalyst was found to be slightly higher than that on the alumina catalyst, which is consistent with the observation that the silica catalyst was not as active as the alumina sample for ozone decomposition.

In a study of the oxidation of lower aliphatic alcohols by ozone on alumina and silica from 293 and 363 K, it was found that the converted ethanol to ozone ratio was about unity. However, in that study the main oxidation products were acetaldehyde and ketones, while the only products observed on the supported manganese catalysts of this study were carbon dioxide and water.

4.4.2. *In Situ Laser Raman Spectroscopic Studies*

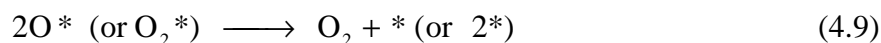
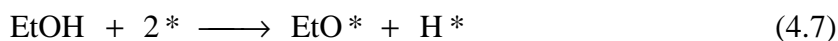
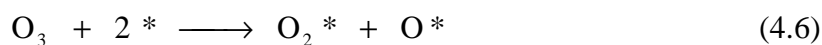
Spectroscopic studies of the interaction between ozone and organic molecules on catalyst surfaces have been very rare. Mariey *et al.* reported a Fourier transform infrared (FTIR) study of ozone interaction with phenol adsorbed on silica and ceria²³. Ozone was found to be reactive toward phenol and carboxylic acids and aldehydes were detected as possible intermediates. However, the study was carried out from 77 to 220 K, which is far from reaction conditions (usually > 300 K) for those surfaces. Recent work from this laboratory has demonstrated that *in situ* laser Raman spectroscopy is an excellent tool to study surface intermediates at reaction conditions^{24,25}. The signal at 654 cm^{-1} under oxygen can be ascribed to Mn_3O_4 , however, this observation does not mean it is the only phase present. Other phases like Mn_2O_3 and MnO show only very weak Raman signals, while MnO_2 is completely Raman inactive. The introduction of ozone formed an adsorbed peroxide species with a Raman signal at 884 cm^{-1} , while the introduction of ethanol generated an adsorbed ethoxide species with Raman signals at 878, 2878, 2930, 2970 cm^{-1} .

²³ Mariey, L.; Lamotte, J.; J.C. Lavalley, Tsyganenko, N. M.; Tsyganenko, A. A. *Catal. Lett.* **1996**, *41*, 209.

²⁴ Zhang, W.; Oyama, S.T. *J. Phys. Chem.* **1996**, *100*, 10759.

²⁵ Zhang, W.; Oyama, S.T. *J. Am. Chem. Soc.* **1996**, *118*, 7173.

Under reaction conditions with the coexistence of ozone and ethanol, the intensities of both these adsorbed species dramatically decreased, indicating that these two species reacted with each other on the catalyst surface. This was also supported by the transient experiment results. When ozone was introduced on a surface preadsorbed with ethoxide species, the intensity of the ethoxide species decreased gradually due to the reaction with ozone (gas phase or adsorbed), and that of the peroxide species increased with time due to the removal of ethoxide species from the surface. However, if the reaction of ethoxide species was mainly due to gas phase ozone, under steady state conditions, the surface should be covered by adsorbed peroxide species. The *in situ* Raman spectra indicated that the reaction of ethoxide species was primarily due to reaction with adsorbed peroxide species because the concentrations of both adsorbed species decreased dramatically in the presence of both ethanol and ozone. Thus, a Langmuir-Hinshelwood type mechanism appears to be operating:



Overall the results are consistent with both ethanol and ozone adsorption being the slow steps in the overall reaction. The surface reaction and desorption steps are fast, and result in a surface that is close to bare.

The kinetics of the reaction was found to be well described by a power law equation (4.2) with the reaction orders of ozone and ethanol between 0 and 1. Both a Langmuir-Hinshelwood treatment and a non-uniform surface treatment give reasonably good fits of the kinetic data.

4.4.3. Role of Ozone Decomposition

As indicated in equation 3, ozone decomposition can be closely associated with the oxidation reaction. It is well accepted that ozone decomposes to produce active oxygen species, which can

activate the organic molecules at lower temperatures. It has also been reported by several groups^{26,27} that at low temperatures the activation energy for oxidation reactions by ozone are similar to that of ozone decomposition, which suggests that the rate determining step for the oxidation reaction is probably ozone decomposition. The results from this study are consistent with that conclusion. In addition, the *in situ* laser Raman spectroscopic study provides direct evidence that surface ethoxide reacted with peroxide species formed by ozone decomposition

4.5. CONCLUSIONS

Ethanol oxidation using ozone was investigated over supported manganese oxide catalysts at temperatures from 300 to 550 K by *in situ* laser Raman spectroscopy coupled with reactivity measurements. Ethanol was found to react with ozone at lower temperatures than with oxygen, and also with a lower activation energy. This is in agreement with the stronger oxidizing ability of ozone compared to oxygen. The oxidation reactivity was found to be closely related to that of ozone decomposition, suggesting an important role of ozone decomposition in the reaction mechanism. *In situ* laser Raman spectroscopic studies provided direct evidence for the reaction between the peroxide (due to ozone) and the ethoxide species (due to ethanol) on the catalyst surfaces.

26. Kleimenov, N. A.; Nalbandian, A. B. *Proceedings of Academy of Science of USSR* **1958**, *122*, 635.

27. Del Rosso, R.; Mazzocchia, C.; Centola, P. *React. Kinet. Catal. Lett.* **1976**, *5*, 245.

CHAPTER 5. RECOMMENDATIONS FOR FUTURE WORK

This dissertation presented a detailed study on the mechanism of ozone reactions on manganese oxide catalysts. For the first time reaction intermediates were observed *in situ* using laser Raman spectroscopy and their roles in the catalytic reactions were determined by steady state and transient kinetic measurements. This work significantly advances our understanding of the ozone reaction mechanism on metal oxide surfaces, and because of the knowledge obtained in this area it will now be possible to postulate some more detailed hypotheses for further studies to verify.

For example, ozone was found to adsorb dissociatively on oxide surfaces to form a peroxide species and an atomic oxygen species. Hence would this imply that the active site for ozone adsorption should be a pair of adjacent metal atoms rather than a single metal site? This hypothesis can be tested by preparing well-defined sample in which all manganese atoms exist as dimers. This type of Mn dimer catalyst was recently prepared¹ by surface grafting of $\text{Mn}_2(\text{CO})_{10}$ on the walls of MCM-41 (mesoporous silica) channels. Characterization of the catalyst using extended X-ray absorption fine structure² (EXAFS) confirmed that manganese existed as dimers via bridging oxygen atoms on the surface. A similar sample can probably be prepared on alumina using the same approach and similar surface manganese species can be expected. Also in comparison, we can prepare a sample having predominantly only single metal sites, which can be accomplished by using a *low loading* of manganese monomer precursor such as manganese acetate used in this dissertation. By using a low loading, it is expected that the manganese species formed on the surface will be predominantly isolated single metal sites. By comparing these two catalysts using both *in situ* laser Raman spectroscopy and kinetic measurements, the nature of the active center for ozone decomposition can be elucidated. If indeed a dimer species is the active center, then we will have a sample with a known number of well-defined active centers. This is significant because understanding of the nature of the active center will shed light on the chemistry occurring during catalytic reactions, and because the number of active centers is an essential

¹ Burch, R.; Cruise, N.; Gleeson, D.; Tsang, S. C. *Chem. Comm.* **1996**, 951-952.

parameter in calculating the turnover rate of a reaction. The catalytic cycle for the decomposition reaction on a dimer catalysts can be proposed as follows:

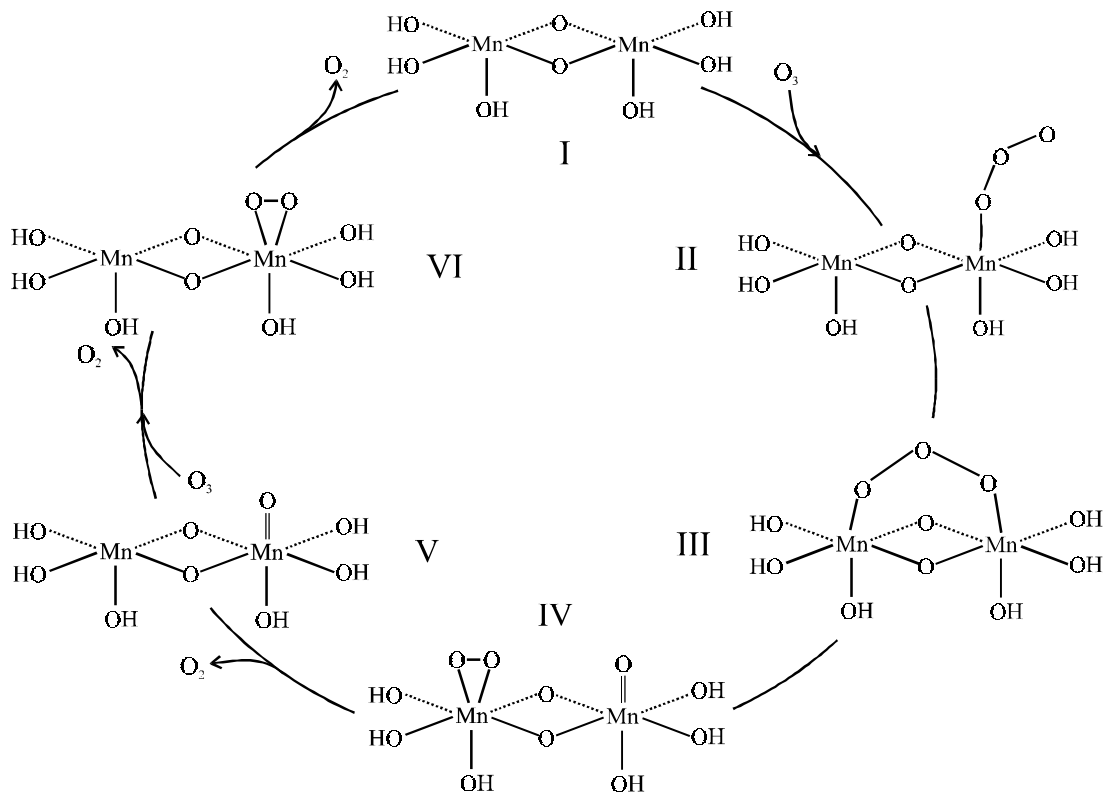


Figure 5.1 Proposed catalytic cycle of ozone decomposition on a manganese dimer catalyst

Since this dimer catalyst has well-defined active sites, it is also possible to model the structure of the active sites and intermediates using first principle calculations, and in this manner the energetics of the reaction can also be calculated. The energetics of the reaction will no doubt give more insights on the reaction pathway and help the rational design of efficient catalysts. Once the geometry and energetics of the reaction intermediates are determined, it is also possible to predict the reaction rate of each step using transition state

² Burch, R.; Cruise, N.; Gleeson, D.; Tsang, S. C. *J. Mater. Chem.* **1998**, *8*,

theory and first-principle calculations. Determination of transition state geometry and the calculation of reaction rate on surfaces are recently emerging as a field of considerable interest³, and several examples have demonstrated that it is certainly feasible. Ozone decomposition on the model dimer catalyst offers an interesting system for this type of approach.

For oxidation reactions of organic substrates, one important question is the rate-determining step (*rds*). Our correlation of the ozone decomposition activity with the oxidation activity suggests that ozone decomposition is the *rds*. However, kinetic studies using ¹⁸O₃ in a recirculation reactor will certainly provide additional evidence. If indeed decomposition of ozone is the *rds* then a first order kinetic isotope effect should be expected. Also silica supported manganese oxide catalysts were found to be much less active for ozone decomposition than alumina supported catalysts, hence the effect of supports on the oxidation reactivities can give further information. Their reactivities for oxidation reactions should be much lower compared to those alumina supported catalysts if ozone decomposition is the *rds*.

³ van Daelen M.A., Li Y.S., Newsam J.M., van Santen R.A. *Chem. Phys. Lett.* **1994**, 226, 100.

APPENDIX A. AB INITIO MO CALCULATION RESULTS

A.1. OUTPUT FILE FOR THE MODEL COMPOUND $\text{Mn}(\text{O}_2)(\text{OH})_4^+$

Copyright (c) 1988,1990,1992,1993,1995 Gaussian, Inc.
All Rights Reserved.

```
*****  
Gaussian 94:  IBM-RS6000-G94RevC.2  5-Aug-1995  
                26-Apr-1998  
*****
```

```
-----  
#P HF/6-311G OPT FREQ TEST  
-----
```

Mn(O2)(OH)4+

Symbolic Z-matrix:

Charge = 1 Multiplicity = 1

Mn	0.	0.	0.28043
O	1.57771	-0.56116	-1.02626
H	2.46961	-0.90754	-1.05225
O	0.56116	-1.57771	-1.02626
H	0.90754	-2.46961	-1.05225
O	-1.57771	0.56116	-1.02626
H	-2.46961	0.90754	-1.05225
O	-0.56116	1.57771	-1.02626
H	-0.90754	2.46961	-1.05225
O	0.51806	-0.51806	1.87742
O	-0.51806	0.51806	1.87742

OPTIMIZATION OUTPUT

Optimization completed.

-- Stationary point found.

```
-----  
!   Optimized Parameters   !  
! (Angstroms and Degrees)  !  
-----
```

! Name	Definition	Value	Derivative Info.	!
! R1	R(2,1)	2.124	-DE/DX = 0.	!
! R2	R(3,2)	0.9572	-DE/DX = 0.	!
! R3	R(4,1)	2.124	-DE/DX = 0.	!
! R4	R(4,2)	1.4376	-DE/DX = 0.	!
! R5	R(5,4)	0.9572	-DE/DX = 0.	!
! R6	R(6,1)	2.124	-DE/DX = 0.	!
! R7	R(7,6)	0.9572	-DE/DX = 0.	!
! R8	R(8,1)	2.124	-DE/DX = 0.	!
! R9	R(8,6)	1.4376	-DE/DX = 0.	!
! R10	R(9,8)	0.9572	-DE/DX = 0.	!
! R11	R(10,1)	1.757	-DE/DX = 0.	!
! R12	R(11,1)	1.757	-DE/DX = 0.	!
! R13	R(11,10)	1.4653	-DE/DX = 0.	!

! A1	A(1,2,3)	143.5582	-DE/DX =	0.	!
! A2	A(2,1,4)	39.561	-DE/DX =	0.	!
! A3	A(1,2,4)	70.2195	-DE/DX =	0.	!
! A4	A(3,2,4)	113.7665	-DE/DX =	0.	!
! A5	A(1,4,2)	70.2195	-DE/DX =	0.	!
! A6	A(1,4,5)	143.5582	-DE/DX =	0.	!
! A7	A(2,4,5)	113.7665	-DE/DX =	0.	!
! A8	A(2,1,6)	104.068	-DE/DX =	0.	!
! A9	A(4,1,6)	90.8034	-DE/DX =	0.	!
! A10	A(1,6,7)	143.5582	-DE/DX =	0.	!
! A11	A(2,1,8)	90.8034	-DE/DX =	0.	!
! A12	A(4,1,8)	104.068	-DE/DX =	0.	!
! A13	A(6,1,8)	39.561	-DE/DX =	0.	!
! A14	A(1,6,8)	70.2195	-DE/DX =	0.	!
! A15	A(7,6,8)	113.7665	-DE/DX =	0.	!
! A16	A(1,8,6)	70.2195	-DE/DX =	0.	!
! A17	A(1,8,9)	143.5582	-DE/DX =	0.	!
! A18	A(6,8,9)	113.7665	-DE/DX =	0.	!
! A19	A(2,1,10)	105.2038	-DE/DX =	0.	!
! A20	A(4,1,10)	105.2038	-DE/DX =	0.	!
! A21	A(6,1,10)	148.8778	-DE/DX =	0.	!
! A22	A(8,1,10)	148.8778	-DE/DX =	0.	!
! A23	A(2,1,11)	148.8778	-DE/DX =	0.	!
! A24	A(4,1,11)	148.8778	-DE/DX =	0.	!
! A25	A(6,1,11)	105.2038	-DE/DX =	0.	!
! A26	A(8,1,11)	105.2038	-DE/DX =	0.	!
! A27	A(10,1,11)	49.2877	-DE/DX =	0.	!
! A28	A(1,10,11)	65.3562	-DE/DX =	0.	!
! A29	A(1,11,10)	65.3562	-DE/DX =	0.	!
! D1	D(3,2,1,4)	-103.5295	-DE/DX =	0.	!
! D2	D(3,2,1,6)	-177.2314	-DE/DX =	0.	!
! D3	D(3,2,1,8)	145.0804	-DE/DX =	0.	!
! D4	D(3,2,1,10)	-7.9206	-DE/DX =	0.	!
! D5	D(3,2,1,11)	23.0299	-DE/DX =	0.	!
! D6	D(4,2,1,6)	-73.7018	-DE/DX =	0.	!
! D7	D(4,2,1,8)	-111.3901	-DE/DX =	0.	!
! D8	D(4,2,1,10)	95.6089	-DE/DX =	0.	!
! D9	D(4,2,1,11)	126.5594	-DE/DX =	0.	!
! D10	D(2,4,1,6)	111.3901	-DE/DX =	0.	!
! D11	D(2,4,1,8)	73.7018	-DE/DX =	0.	!
! D12	D(2,4,1,10)	-95.6089	-DE/DX =	0.	!
! D13	D(2,4,1,11)	-126.5594	-DE/DX =	0.	!
! D14	D(5,4,1,2)	103.5295	-DE/DX =	0.	!
! D15	D(5,4,1,6)	-145.0804	-DE/DX =	0.	!
! D16	D(5,4,1,8)	177.2314	-DE/DX =	0.	!
! D17	D(5,4,1,10)	7.9206	-DE/DX =	0.	!
! D18	D(5,4,1,11)	-23.0299	-DE/DX =	0.	!
! D19	D(1,4,2,3)	140.8734	-DE/DX =	0.	!
! D20	D(5,4,2,1)	-140.8734	-DE/DX =	0.	!
! D21	D(5,4,2,3)	0.	-DE/DX =	0.	!
! D22	D(7,6,1,2)	-177.2314	-DE/DX =	0.	!
! D23	D(7,6,1,4)	145.0804	-DE/DX =	0.	!
! D24	D(7,6,1,8)	-103.5295	-DE/DX =	0.	!
! D25	D(7,6,1,10)	23.0299	-DE/DX =	0.	!

! D26	D(7,6,1,11)	-7.9206	-DE/DX =	0.	!
! D27	D(8,6,1,2)	-73.7018	-DE/DX =	0.	!
! D28	D(8,6,1,4)	-111.3901	-DE/DX =	0.	!
! D29	D(8,6,1,10)	126.5594	-DE/DX =	0.	!
! D30	D(8,6,1,11)	95.6089	-DE/DX =	0.	!
! D31	D(6,8,1,2)	111.3901	-DE/DX =	0.	!
! D32	D(6,8,1,4)	73.7018	-DE/DX =	0.	!
! D33	D(6,8,1,10)	-126.5594	-DE/DX =	0.	!
! D34	D(6,8,1,11)	-95.6089	-DE/DX =	0.	!
! D35	D(9,8,1,2)	-145.0804	-DE/DX =	0.	!
! D36	D(9,8,1,4)	177.2314	-DE/DX =	0.	!
! D37	D(9,8,1,6)	103.5295	-DE/DX =	0.	!
! D38	D(9,8,1,10)	-23.0299	-DE/DX =	0.	!
! D39	D(9,8,1,11)	7.9206	-DE/DX =	0.	!
! D40	D(1,8,6,7)	140.8734	-DE/DX =	0.	!
! D41	D(9,8,6,1)	-140.8734	-DE/DX =	0.	!
! D42	D(9,8,6,7)	0.	-DE/DX =	0.	!
! D43	D(11,10,1,2)	159.4703	-DE/DX =	0.	!
! D44	D(11,10,1,4)	-159.4703	-DE/DX =	0.	!
! D45	D(11,10,1,6)	-40.9007	-DE/DX =	0.	!
! D46	D(11,10,1,8)	40.9007	-DE/DX =	0.	!
! D47	D(10,11,1,2)	-40.9007	-DE/DX =	0.	!
! D48	D(10,11,1,4)	40.9007	-DE/DX =	0.	!
! D49	D(10,11,1,6)	159.4703	-DE/DX =	0.	!
! D50	D(10,11,1,8)	-159.4703	-DE/DX =	0.	!

Test job not archived.

```
1\1\GINC-SPIDER07\FOpt\RHF\6-311G\H4Mn1O6(1+)\WELI3\26-Apr-1998\0\#\#P
HF/6-311G OPT FREQ TEST\Mn(O2)(OH)4+\1,1\Mn,0.,0.,0.280426909\O,-1.
5124101882,-0.7188101055,-1.0262640909\H,-2.3880077874,-1.104552411,-1
.0522470909\O,-1.5124101882,0.7188101055,-1.0262640909\H,-2.3880077874
,1.104552411,-1.0522470909\O,1.5124101882,0.7188101055,-1.0262640909\H
,2.3880077874,1.104552411,-1.0522470909\O,1.5124101882,-0.7188101055,-
1.0262640909\H,2.3880077874,-1.104552411,-1.0522470909\O,-0.7326404071
,0.,1.8774229091\O,0.7326404071,0.,1.8774229091\Version=IBM-RS6000-G9
4RevC.2\State=1-Al\HF=-1600.4488791\RMSD=5.742e-09\RMSF=3.701e-05\Dipo
le=0.,0.,-3.3211807\PG=C02V [C2(Mn1),SGV(O2),X(H4O4)]\@\
```

Change starts when someone sees the next step.

-- William Drayton

Job cpu time: 0 days 0 hours 14 minutes 14.2 seconds.

File lengths (MBytes): RWF= 19 Int= 0 D2E= 0 Chk= 3 Scr= 1

Normal termination of Gaussian 94

FREQUENCY CALCULATION

```
#P Geom=AllCheck Guess=Read Test RHF/6-311G Freq
```

Input orientation:

```
-----
Center      Atomic      Coordinates (Angstroms)
Number      Number          X           Y           Z
-----
```

1	25	.000000	.000000	.280427
2	8	-1.512410	-.718810	-1.026264
3	1	-2.388008	-1.104552	-1.052247
4	8	-1.512410	.718810	-1.026264
5	1	-2.388008	1.104552	-1.052247
6	8	1.512410	.718810	-1.026264
7	1	2.388008	1.104552	-1.052247
8	8	1.512410	-.718810	-1.026264
9	1	2.388008	-1.104552	-1.052247
10	8	-.732640	.000000	1.877423
11	8	.732640	.000000	1.877423

Distance matrix (angstroms):

	1	2	3	4	5
1 Mn	.000000				
2 O	2.124032	.000000			
3 H	2.949345	.957154	.000000		
4 O	2.124032	1.437620	2.022869	.000000	
5 H	2.949345	2.022869	2.209105	.957154	.000000
6 O	2.124032	3.349073	4.305646	3.024820	3.919532
7 H	2.949345	4.305646	5.262173	3.919532	4.776016
8 O	2.124032	3.024820	3.919532	3.349073	4.305646
9 H	2.949345	3.919532	4.776016	4.305646	5.262173
10 O	1.757031	3.091299	3.541644	3.091299	3.541644
11 O	1.757031	3.740099	4.420571	3.740099	4.420571
	6	7	8	9	10
6 O	.000000				
7 H	.957154	.000000			
8 O	1.437620	2.022869	.000000		
9 H	2.022869	2.209105	.957154	.000000	
10 O	3.740099	4.420571	3.740099	4.420571	.000000
11 O	3.091299	3.541644	3.091299	3.541644	1.465281
	11				
11 O	.000000				

Interatomic angles:

Mn1-O2-H3=143.5582	Mn1-O4-O2= 70.2195	Mn1-O4-H3= 90.6343
H3-O2-O4=113.7665	Mn1-O2-H5= 90.6343	Mn1-H5-H3= 68.0061
H3-O2-H5= 88.1058	Mn1-O4-H5=143.5582	O2-O4-H5=113.7665
H3-O4-H5= 88.1058	O2-Mn1-O6=104.068	H3-Mn1-O6=115.1689
O4-Mn1-O6= 90.8034	H5-Mn1-O6= 99.8929	O2-Mn1-H7=115.1689
H3-Mn1-H7=126.2746	O4-Mn1-H7= 99.8929	H5-Mn1-H7=108.1282
Mn1-O6-H7=143.5582	O2-Mn1-O8= 90.8034	H3-Mn1-O8= 99.8929
O4-Mn1-O8=104.068	H5-Mn1-O8=115.1689	Mn1-O8-O6= 70.2195
Mn1-O8-H7= 90.6343	H7-O6-O8=113.7665	O2-Mn1-H9= 99.8929
H3-Mn1-H9=108.1282	O4-Mn1-H9=115.1689	H5-Mn1-H9=126.2746
Mn1-O6-H9= 90.6343	Mn1-H7-H9= 68.0061	H7-O6-H9= 88.1058
Mn1-O8-H9=143.5582	O6-O8-H9=113.7665	H7-O8-H9= 88.1058
O2-Mn1-O10=105.2038	H3-Mn1-O10= 94.1911	O4-Mn1-O10=105.2038
H5-Mn1-O10= 94.1911	O6-Mn1-O10=148.8778	H7-Mn1-O10=138.4445
O8-Mn1-O10=148.8778	H9-Mn1-O10=138.4445	O2-Mn1-O11=148.8778
H3-Mn1-O11=138.4445	O4-Mn1-O11=148.8778	H5-Mn1-O11=138.4445
O6-Mn1-O11=105.2038	H7-Mn1-O11= 94.1911	O8-Mn1-O11=105.2038

H9-Mn1-O11= 94.1911 Mn1-O11-O10= 65.3562
 Stoichiometry H4MnO6(1+)
 Framework group C2V[C2(Mn),SGV(O2),X(H4O4)]
 Deg. of freedom 8
 Full point group C2V NOp 4
 Largest Abelian subgroup C2V NOp 4
 Largest concise Abelian subgroup C2V NOp 4

Standard orientation:

Center Number	Atomic Number	Coordinates (Angstroms)		
		X	Y	Z
1	25	.000000	.000000	.280427
2	8	-.718810	1.512410	-1.026264
3	1	-1.104552	2.388008	-1.052247
4	8	.718810	1.512410	-1.026264
5	1	1.104552	2.388008	-1.052247
6	8	.718810	-1.512410	-1.026264
7	1	1.104552	-2.388008	-1.052247
8	8	-.718810	-1.512410	-1.026264
9	1	-1.104552	-2.388008	-1.052247
10	8	.000000	.732640	1.877423
11	8	.000000	-.732640	1.877423

Rotational constants (GHZ): 2.2513155 2.2292897 1.3468530
 Isotopes: Mn-55,O-16,H-1,O-16,H-1,O-16,H-1,O-16,H-1,O-16,O-16
 Leave Link 202 at Sun Apr 26 18:01:01 1998, MaxMem= 4000000 cpu: .1
 (Enter /apps/g94/l301.exe)
 Standard basis: 6-311G (5D, 7F)
 There are 46 symmetry adapted basis functions of A1 symmetry.
 There are 22 symmetry adapted basis functions of A2 symmetry.
 There are 27 symmetry adapted basis functions of B1 symmetry.
 There are 34 symmetry adapted basis functions of B2 symmetry.
 Crude estimate of integral set expansion from redundant integrals=1.083.
 Integral buffers will be 262144 words long.
 Raffennetti 1 integral format.
 Two-electron integral symmetry is turned on.
 129 basis functions 242 primitive gaussians
 38 alpha electrons 38 beta electrons
 nuclear repulsion energy 574.4437257083 Hartrees.

Dipole =-3.57685467D-15 4.79616347D-14-3.32118095D+00
 Polarizability= 3.24776086D+01 4.00524255D-05 3.81870529D+01
 5.03216819D-06-2.21695439D-07 3.47736420D+01
 HyperPolar = 3.95817632D-02-6.47307009D-03 1.71446744D-03
 -1.00281235D-04-6.55486267D+01 4.10543909D-05
 3.44830480D+01-1.29042523D-03 7.08366067D-05
 -6.41386067D+01

Full mass-weighted force constant matrix:
 Low frequencies --- -483.3751 -475.2478 -5.6993 -4.5988 -3.1598 -.0326
 Low frequencies --- .0697 .8496 71.0572
 ***** 2 imaginary frequencies (negative signs) *****
 Harmonic frequencies (cm**-1), IR intensities (KM/Mole),
 Raman scattering activities (A**4/AMU), Raman depolarization ratios,

reduced masses (AMU), force constants (mDyne/A) and normal coordinates:

	1	2	3
	A2	B1	A2
Frequencies --	-483.3751	-475.2478	71.0549
Red. masses --	1.1428	1.1327	6.4555
Frc consts --	.1573	.1507	.0192
IR Inten --	.0000	16.7579	.0001
Raman Activ --	.3370	1.6940	3.6172
Depolar --	.7500	.7500	.7500

Atom AN	X	Y	Z	X	Y	Z	X	Y	Z
1 25	.00	.00	.00	.01	.00	.00	.00	.00	.00
2 8	-.01	.01	-.05	.00	.00	-.04	-.02	-.07	.20
3 1	.04	.05	.49	.04	.04	.49	-.15	-.13	.35
4 8	-.01	-.01	.05	.00	.00	.04	-.02	.07	-.20
5 1	.04	-.05	-.49	.04	-.04	-.49	-.15	.13	-.35
6 8	.01	-.01	-.05	.00	.00	.04	.02	.07	.20
7 1	-.04	-.05	.49	.04	.04	-.49	.15	.13	.35
8 8	.01	.01	.05	.00	.00	-.04	.02	-.07	-.20
9 1	-.04	.05	-.49	.04	-.04	.49	.15	-.13	-.35
10 8	.00	.00	.00	-.01	.00	.00	.30	.00	.00
11 8	.00	.00	.00	-.01	.00	.00	-.30	.00	.00

	4	5	6
	?A	?A	B2
Frequencies --	123.0636	133.3785	145.9094
Red. masses --	6.9608	5.4583	4.5027
Frc consts --	.0621	.0572	.0565
IR Inten --	.0001	45.6444	31.4429
Raman Activ --	5.3113	1.3164	.9447
Depolar --	.7500	.5187	.7500

Atom AN	X	Y	Z	X	Y	Z	X	Y	Z
1 25	.00	.00	.00	.00	.00	-.11	.00	.10	.00
2 8	-.09	.20	.19	.00	.20	.13	.00	.01	-.12
3 1	.16	.31	.17	.00	.21	.37	-.02	.00	-.44
4 8	-.09	-.21	-.19	.00	.20	.13	.00	.01	-.12
5 1	.16	-.31	-.17	.00	.21	.37	.02	.00	-.44
6 8	.09	-.20	.19	.00	-.20	.13	.00	.01	.12
7 1	-.16	-.31	.17	.00	-.21	.37	-.02	.00	.44
8 8	.09	.20	-.19	.00	-.20	.13	.00	.01	.12
9 1	-.16	.31	-.17	.00	-.21	.37	.02	.00	.44
10 8	-.17	.00	.00	.00	.00	-.11	.00	-.20	.18
11 8	.17	.00	.00	.00	.00	-.11	.00	-.20	-.18

	7	8	9
	B1	A2	B1
Frequencies --	167.0152	215.0846	251.5734
Red. masses --	4.4252	7.2738	5.6815
Frc consts --	.0727	.1983	.2119
IR Inten --	34.1393	.0001	5.8566
Raman Activ --	.5184	.0152	4.0353
Depolar --	.7500	.7500	.7500

Atom AN	X	Y	Z	X	Y	Z	X	Y	Z
1 25	-.08	.00	.00	.00	.00	.00	-.06	.00	.00
2 8	.04	.21	.0	.16	-.15	.12	.10	-.10	.23

3	1	.30	.32	.06	-.07	-.25	.28	-.08	-.17	.37
4	8	.04	-.21	-.07	.16	.15	-.12	.10	.10	-.23
5	1	.30	-.32	-.06	-.07	.25	-.28	-.08	.17	-.37
6	8	.04	.21	-.07	-.16	.15	.12	.10	-.10	-.23
7	1	.30	.32	-.06	.07	.25	.28	-.08	-.17	-.37
8	8	.04	-.21	.07	-.16	-.15	-.12	.10	.10	.23
9	1	.30	-.32	.06	.07	-.25	-.28	-.08	.17	.37
10	8	.02	.00	.00	-.28	.00	.00	-.09	.00	.00
11	8	.02	.00	.00	.29	.00	.00	-.09	.00	.00

		10			11			12		
		A1			B2			B2		
Frequencies	--	299.5081			333.7216			391.0308		
Red. masses	--	3.3000			12.9739			1.3196		
Frc consts	--	.1744			.8513			.1189		
IR Inten	--	100.1339			44.6353			1.3715		
Raman Activ	--	10.9168			.2802			4.9317		
Depolar	--	.3861			.7500			.7500		
Atom AN		X	Y	Z	X	Y	Z	X	Y	Z
1	25	.00	.00	.07	.00	.29	.00	.00	.02	.00
2	8	.01	.15	-.08	-.01	-.26	.21	-.01	-.01	-.06
3	1	.00	.13	-.44	-.05	-.28	.16	.04	.03	.49
4	8	-.01	.15	-.08	.01	-.26	.21	.01	-.01	-.06
5	1	.00	.13	-.44	.05	-.28	.16	-.04	.03	.49
6	8	-.01	-.15	-.08	-.01	-.26	-.21	-.01	-.01	.06
7	1	.00	-.13	-.44	-.05	-.28	-.16	.04	.03	-.49
8	8	.01	-.15	-.08	.01	-.26	-.21	.01	-.01	.06
9	1	.00	-.13	-.44	.05	-.28	-.16	-.04	.03	-.49
10	8	.00	-.01	.09	.00	.05	.15	.00	-.02	.04
11	8	.00	.01	.09	.00	.05	-.15	.00	-.02	-.04
		13			14			15		
		A1			B2			?B		
Frequencies	--	453.0543			549.7225			633.8096		
Red. masses	--	1.5365			17.0188			21.2854		
Frc consts	--	.1858			3.0302			5.0379		
IR Inten	--	978.4782			21.8422			7.6676		
Raman Activ	--	1.7067			2.8394			26.1029		
Depolar	--	.5061			.7500			.7500		
Atom AN		X	Y	Z	X	Y	Z	X	Y	Z
1	25	.00	.00	-.03	.00	.22	.00	.45	.00	.00
2	8	.01	-.02	.08	-.01	-.02	-.04	-.17	.13	.15
3	1	-.05	-.06	-.49	.00	.00	.11	-.04	.20	.04
4	8	-.01	-.02	.08	.01	-.02	-.04	-.17	-.13	-.15
5	1	.05	-.06	-.49	.00	.00	.11	-.04	-.20	-.04
6	8	-.01	.02	.08	-.01	-.02	.04	-.17	.13	-.15
7	1	.05	.06	-.49	.00	.00	-.11	-.04	.20	-.04
8	8	.01	.02	.08	.01	-.02	.04	-.17	-.13	.15
9	1	-.05	.06	-.49	.00	.00	-.11	-.04	-.20	.04
10	8	.00	.01	-.05	.00	-.34	-.58	-.42	.00	.00
11	8	.00	-.01	-.05	.00	-.34	.58	-.42	.00	.00
		16			17			18		
		?B			A1			B2		
Frequencies	--	707.9048			1006.3073			1020.0688		

Red. masses	--	19.7809		16.8103		12.7980
Frc consts	--	5.8404		10.0297		7.8460
IR Inten	--	44.0176		174.1432		.0924
Raman Activ	--	27.5595		31.3562		.0894
Depolar	--	.6618		.4876		.7500

Atom	AN	X	Y	Z	X	Y	Z	X	Y	Z
1	25	.00	.00	.33	.00	.00	-.17	.00	.01	.00
2	8	.00	.03	-.03	.06	.00	.00	.44	.00	.00
3	1	.03	.04	.07	-.05	-.04	-.03	.16	-.15	.08
4	8	.00	.03	-.03	-.06	.00	.00	-.44	.00	.00
5	1	-.03	.04	.07	.05	-.04	-.03	-.16	-.15	.08
6	8	.00	-.03	-.03	-.06	.00	.00	.44	.00	.00
7	1	-.03	-.04	.07	.05	.04	-.03	.16	-.15	-.08
8	8	.00	-.03	-.03	.06	.00	.00	-.44	.00	.00
9	1	.03	-.04	.07	-.05	.04	-.03	-.16	-.15	-.08
10	8	.00	.40	-.52	.00	.62	.29	.00	.00	.00
11	8	.00	-.40	-.52	.00	-.62	.29	.00	.00	.00

		19		20		21
		A1		B2		A1
Frequencies	--	1020.7730		1408.8709		1418.9319
Red. masses	--	12.7382		1.0226		1.0233
Frc consts	--	7.8202		1.1960		1.2139
IR Inten	--	1.5932		21.7386		.7032
Raman Activ	--	84.9842		.0212		4.4513
Depolar	--	.2924		.7500		.5414

Atom	AN	X	Y	Z	X	Y	Z	X	Y	Z
1	25	.00	.00	-.01	.00	.00	.00	.00	.00	.00
2	8	-.44	.00	.00	-.01	-.01	.01	-.01	-.01	.01
3	1	-.16	.15	-.07	.46	.18	-.04	.46	.18	-.04
4	8	.44	.00	.00	.01	-.01	.01	.01	-.01	.01
5	1	.16	.15	-.07	-.46	.18	-.04	-.46	.18	-.04
6	8	.44	.00	.00	-.01	-.01	-.01	.01	.01	.01
7	1	.16	-.15	-.07	.46	.18	.04	-.46	-.18	-.04
8	8	-.44	.00	.00	.01	-.01	-.01	-.01	.01	.01
9	1	-.16	-.15	-.07	-.46	.18	.04	.46	-.18	-.04
10	8	.00	.06	.03	.00	.00	.00	.00	.00	.00
11	8	.00	-.06	.03	.00	.00	.00	.00	.00	.00

		22		23		24
		A2		B1		A2
Frequencies	--	1502.4299		1510.2491		3911.8584
Red. masses	--	1.2449		1.2398		1.0703
Frc consts	--	1.6557		1.6661		9.6501
IR Inten	--	.0000		141.5768		.0000
Raman Activ	--	11.7515		.0346		54.6491
Depolar	--	.7500		.7500		.7500

Atom	AN	X	Y	Z	X	Y	Z	X	Y	Z
1	25	.00	.00	.00	.00	.00	.00	.00	.00	.00
2	8	-.03	-.06	.01	-.03	-.05	.01	.01	-.03	.00
3	1	.47	.15	-.04	.47	.16	-.04	-.20	.46	-.02
4	8	-.03	.06	-.01	-.03	.05	-.01	.01	.03	.00
5	1	.47	-.15	.04	.47	-.16	.04	-.20	-.46	.02
6	8	.03	.06	.01	-.03	-.05	-.01	-.01	.03	.00

7	1	-.47	-.15	-.04	.47	.16	.04	.20	-.46	-.02
8	8	.03	-.06	-.01	-.03	.05	.01	-.01	-.03	.00
9	1	-.47	.15	.04	.47	-.16	-.04	.20	.46	.02
10	8	.00	.00	.00	.00	.00	.00	.00	.00	.00
11	8	.00	.00	.00	.00	.00	.00	.00	.00	.00

		25			26			27		
		B1			B2			A1		
Frequencies	--	3913.0568			3950.8138			3954.1780		
Red. masses	--	1.0707			1.0708			1.0711		
Frc consts	--	9.6595			9.8476			9.8669		
IR Inten	--	409.3127			641.7429			15.3550		
Raman Activ	--	.5754			15.5497			150.4685		
Depolar	--	.7500			.7500			.1534		
Atom AN		X	Y	Z	X	Y	Z	X	Y	Z
1	25	.00	.00	.00	.00	.00	.00	.00	.00	.00
2	8	.01	-.03	.00	.01	-.03	.00	.01	-.03	.00
3	1	-.20	.46	-.02	-.19	.46	-.02	-.19	.46	-.02
4	8	.01	.03	.00	-.01	-.03	.00	-.01	-.03	.00
5	1	-.20	-.46	.02	.19	.46	-.02	.19	.46	-.02
6	8	.01	-.03	.00	.01	-.03	.00	-.01	.03	.00
7	1	-.20	.46	.02	-.19	.46	.02	.19	-.46	-.02
8	8	.01	.03	.00	-.01	-.03	.00	.01	.03	.00
9	1	-.20	-.46	-.02	.19	.46	.02	-.19	-.46	-.02
10	8	.00	.00	.00	.00	.00	.00	.00	.00	.00
11	8	.00	.00	.00	.00	.00	.00	.00	.00	.00

- Thermochemistry -

Temperature 298.150 Kelvin. Pressure 1.00000 Atm.

Atom 1 has atomic number 25 and mass 54.93805
Atom 2 has atomic number 8 and mass 15.99491
Atom 3 has atomic number 1 and mass 1.00783
Atom 4 has atomic number 8 and mass 15.99491
Atom 5 has atomic number 1 and mass 1.00783
Atom 6 has atomic number 8 and mass 15.99491
Atom 7 has atomic number 1 and mass 1.00783
Atom 8 has atomic number 8 and mass 15.99491
Atom 9 has atomic number 1 and mass 1.00783
Atom 10 has atomic number 8 and mass 15.99491
Atom 11 has atomic number 8 and mass 15.99491

Molecular mass: 154.93883 amu.

Principle axes and moments of inertia in atomic units:

	1	2	3
EIGENVALUES --	801.63850	809.55884	1339.96893
X	.00000	.00000	1.00000
Y	.00000	1.00000	.00000
Z	1.00000	.00000	.00000

THIS MOLECULE IS AN ASYMMETRIC TOP.

ROTATIONAL SYMMETRY NUMBER 2.

WARNING-- ASSUMPTION OF CLASSICAL BEHAVIOR FOR ROTATION
MAY CAUSE SIGNIFICANT ERROR

ROTATIONAL TEMPERATURES (KELVIN) .10805 .10699 .06464

ROTATIONAL CONSTANTS (GHZ) 2.25132 2.22929 1.34685

2 IMAGINARY FREQUENCIES IGNORED.

Zero-point vibrational energy 174017.0 (Joules/Mol)
41.59106 (Kcal/Mol)

WARNING-- EXPLICIT CONSIDERATION OF 12 DEGREES OF FREEDOM AS
VIBRATIONS MAY CAUSE SIGNIFICANT ERROR

VIBRATIONAL TEMPERATURES:	102.23	177.06	191.90	209.93	240.30
(KELVIN)	309.46	361.96	430.92	480.15	562.60
	651.84	790.92	911.91	1018.51	1447.84
	1467.64	1468.66	2027.04	2041.51	2161.65
	2172.90	5628.26	5629.98	5684.31	5689.15

Zero-point correction=	.066280
(Hartree/Particle)	
Thermal correction to Energy=	.075503
Thermal correction to Enthalpy=	.076448
Thermal correction to Gibbs Free Energy=	.032313
Sum of electronic and zero-point Energies=	-1600.382600
Sum of electronic and thermal Energies=	-1600.373376
Sum of electronic and thermal Enthalpies=	-1600.372431
Sum of electronic and thermal Free Energies=	-1600.416566

	E	CV	S
	KCAL/MOL	CAL/MOL-KELVIN	CAL/MOL-KELVIN
TOTAL	47.379	29.619	92.888
ELECTRONIC	.000	.000	.000
TRANSLATIONAL	.889	2.981	41.023
ROTATIONAL	.889	2.981	26.878
VIBRATIONAL	45.602	23.657	24.987
VIBRATION 1	.598	1.968	4.124
VIBRATION 2	.610	1.930	3.052
VIBRATION 3	.613	1.920	2.897
VIBRATION 4	.617	1.907	2.725
VIBRATION 5	.624	1.883	2.469
VIBRATION 6	.645	1.818	2.000
VIBRATION 7	.664	1.760	1.720
VIBRATION 8	.692	1.675	1.420
VIBRATION 9	.715	1.608	1.242
VIBRATION 10	.759	1.489	.996
VIBRATION 11	.812	1.354	.787
VIBRATION 12	.905	1.140	.545
	Q	LOG10(Q)	LN(Q)
TOTAL BOT	.137070D-14	-14.863057	-40.028376
TOTAL V=0	.419978D+16	15.623227	30.168887
VIB (BOT)	.108333D-27	-27.965238	-64.392341
VIB (BOT) 1	.290218D+01	.462724	1.065462
VIB (BOT) 2	.165940D+01	.219951	.506456
VIB (BOT) 3	.152717D+01	.183887	.423416
VIB (BOT) 4	.139132D+01	.143426	.330251
VIB (BOT) 5	.120780D+01	.081997	.188804
VIB (BOT) 6	.921536D+00	-.035488	-.081713
VIB (BOT) 7	.775228D+00	-.110570	-.254598
VIB (BOT) 8	.635143D+00	-.197129	-.453905
VIB (BOT) 9	.558604D+00	-.252896	-.582315

VIB (BOT) 10	.458786D+00	-.338389	-.779171
VIB (BOT) 11	.377576D+00	-.422995	-.973982
VIB (BOT) 12	.285554D+00	-.544312	-1.253324
VIB (V=0)	.331929D+03	2.521046	5.804922
VIB (V=0) 1	.344494D+01	.537181	1.236905
VIB (V=0) 2	.223309D+01	.348907	.803387
VIB (V=0) 3	.210694D+01	.323651	.745235
VIB (V=0) 4	.197843D+01	.296321	.682305
VIB (V=0) 5	.180721D+01	.257008	.591783
VIB (V=0) 6	.154844D+01	.189895	.437249
VIB (V=0) 7	.142249D+01	.153048	.352405
VIB (V=0) 8	.130834D+01	.116719	.268756
VIB (V=0) 9	.124969D+01	.096803	.222897
VIB (V=0) 10	.117859D+01	.071363	.164319
VIB (V=0) 11	.112655D+01	.051750	.119159
VIB (V=0) 12	.107580D+01	.031730	.073061
ELECTRONIC	.100000D+01	.000000	.000000
TRANSLATIONAL	.758055D+08	7.879701	18.143682
ROTATIONAL	.166909D+06	5.222480	12.025205

***** Axes restored to original set *****

Center Number	Atomic Number	Forces (Hartrees/Bohr)		
		X	Y	Z
1	25	.000000000	.000000000	.000141627
2	8	-.000023996	-.000067844	-.000009795
3	1	-.000009823	.000005000	-.000018850
4	8	-.000023996	.000067844	-.000009795
5	1	-.000009823	-.000005000	-.000018850
6	8	.000023996	.000067844	-.000009795
7	1	.000009823	-.000005000	-.000018850
8	8	.000023996	-.000067844	-.000009795
9	1	.000009823	.000005000	-.000018850
10	8	.000029715	.000000000	-.000013522
11	8	-.000029715	.000000000	-.000013522

Cartesian Forces: Max .000141627 RMS .000037008
Internal Forces: Max .000049898 RMS .000013419

Force constants in Cartesian coordinates:

	1	2	3	4	5
1	.187395D+00				
2	-.108202D-04	.442748D+00			
3	.000000D+00	-.142637D-04	.555828D+00		
4	-.235351D-01	-.447998D-01	-.195915D-01	.617777D+00	
5	-.734312D-02	-.532092D-01	-.172933D-02	.170722D+00	.451316D+00
6	-.779906D-02	.361124D-01	-.282063D-01	.483912D-01	-.515941D-02
7	-.183254D-02	.407688D-02	.142773D-02	-.497093D+00	-.201548D+00
8	-.448943D-02	.942585D-03	-.572912D-02	-.130280D+00	-.122521D+00
9	-.315323D-02	-.785416D-03	.462168D-02	-.216788D-01	-.998894D-03
10	-.235350D-01	.448726D-01	-.195914D-01	-.106063D+00	.583503D-01
11	.734306D-02	-.531789D-01	.172931D-02	-.583503D-01	-.292865D+00
12	-.779896D-02	-.361147D-01	-.282064D-01	-.755363D-02	.929413D-02
13	-.183272D-02	-.414118D-02	.142774D-02	.149956D-01	-.201295D-01

14	.448943D-02	.962642D-03	.572912D-02	.415297D-01	-.216505D-01
15	-.315331D-02	.795086D-03	.462169D-02	.349697D-02	-.101562D-02
16	-.235352D-01	-.448100D-01	.195915D-01	.871053D-03	.253185D-02
17	-.734315D-02	-.531807D-01	.172930D-02	.253185D-02	.577642D-02
18	.779917D-02	-.361259D-01	-.282064D-01	.264123D-02	.333523D-02
19	-.183250D-02	.410746D-02	-.142773D-02	.333864D-03	.142644D-03
20	-.448939D-02	.940320D-03	.572912D-02	-.104691D-04	-.394861D-03
21	.315327D-02	.780661D-03	.462168D-02	-.128925D-03	.454596D-04
22	-.235352D-01	.447907D-01	.195914D-01	-.624435D-02	-.345110D-02
23	.734318D-02	-.531885D-01	-.172930D-02	.345110D-02	.654878D-02
24	.779897D-02	.361071D-01	-.282063D-01	-.163745D-02	-.266064D-02
25	-.183247D-02	-.409227D-02	-.142775D-02	-.324811D-05	-.616470D-04
26	.448931D-02	.940176D-03	-.572913D-02	-.107739D-02	-.890226D-03
27	.315320D-02	-.764901D-03	.462169D-02	-.529536D-03	-.431082D-03
28	-.429611D-01	.573358D-04	.103055D+00	.299026D-02	.220260D-02
29	.368956D-05	-.116912D+00	.466453D-05	.655354D-02	.112529D-01
30	.557248D-01	.000000D+00	-.230748D+00	.259126D-03	-.202050D-03
31	-.429611D-01	-.509913D-04	-.103055D+00	-.403193D-02	-.141408D-02
32	.372592D-05	-.116876D+00	-.468843D-05	.974094D-02	.166230D-01
33	-.557249D-01	.931992D-05	-.230748D+00	-.366158D-02	-.479386D-03
	6	7	8	9	10
6	.290680D-01				
7	-.256741D-01	.476088D+00			
8	.769595D-02	.176300D+00	.148198D+00		
9	-.201809D-03	.190741D-01	.146645D-02	.731757D-05	
10	-.755363D-02	.149956D-01	-.415297D-01	.349697D-02	.617777D+00
11	-.929413D-02	.201295D-01	-.216505D-01	.101562D-02	-.170722D+00
12	.137224D-01	.395307D-02	-.424555D-02	-.105345D-01	.483912D-01
13	.395307D-02	.724460D-02	-.116038D-02	.213753D-03	-.497093D+00
14	.424555D-02	.116038D-02	-.150787D-02	-.333155D-03	.130280D+00
15	-.105345D-01	.213753D-03	.333155D-03	.639099D-02	-.216788D-01
16	-.264123D-02	.333864D-03	-.104691D-04	.128925D-03	-.624435D-02
17	-.333523D-02	.142644D-03	-.394861D-03	-.454596D-04	-.345110D-02
18	-.650160D-02	-.144393D-03	-.597160D-03	-.944623D-03	-.163745D-02
19	.144393D-03	-.388672D-04	-.142723D-03	-.313315D-04	-.324811D-05
20	.597160D-03	-.142723D-03	-.919335D-04	-.765913D-04	.107739D-02
21	-.944623D-03	.313315D-04	.765913D-04	.232917D-03	-.529536D-03
22	.163745D-02	-.324811D-05	.107739D-02	.529536D-03	.871053D-03
23	-.266064D-02	.616470D-04	-.890226D-03	-.431082D-03	-.253185D-02
24	.102411D-01	-.176975D-04	.457559D-04	-.350839D-03	.264123D-02
25	.176975D-04	-.257956D-03	.761820D-04	-.294548D-04	.333864D-03
26	.457559D-04	-.761820D-04	.592958D-03	.153497D-03	.104691D-04
27	-.350839D-03	.294548D-04	.153497D-03	.380187D-03	-.128925D-03
28	-.364269D-02	-.239662D-03	-.147465D-02	.139818D-02	.299014D-02
29	-.166936D-01	-.285560D-03	-.117657D-02	-.146439D-03	-.657926D-02
30	-.740666D-03	.548702D-03	.499384D-03	.792289D-03	.259224D-03
31	-.683411D-02	.805366D-03	.163499D-02	.517718D-04	-.403191D-02
32	-.115605D-01	.159416D-03	-.150083D-02	.177656D-03	-.973425D-02
33	-.555314D-02	.551785D-03	.299333D-03	-.391610D-03	-.366154D-02
	11	12	13	14	15
11	.451316D+00				
12	.515941D-02	.290680D-01			
13	.201548D+00	-.256741D-01	.476088D+00		
14	-.122521D+00	-.769595D-02	-.176300D+00	.148198D+00	

15	.998894D-03	-.201809D-03	.190741D-01	-.146645D-02	.731757D-05
16	.345110D-02	.163745D-02	-.324811D-05	-.107739D-02	.529536D-03
17	.654878D-02	.266064D-02	-.616470D-04	-.890226D-03	.431082D-03
18	.266064D-02	.102411D-01	-.176975D-04	-.457559D-04	-.350839D-03
19	.616470D-04	.176975D-04	-.257956D-03	-.761820D-04	-.294548D-04
20	-.890226D-03	-.457559D-04	.761820D-04	.592958D-03	-.153497D-03
21	.431082D-03	-.350839D-03	.294548D-04	-.153497D-03	.380187D-03
22	-.253185D-02	-.264123D-02	.333864D-03	.104691D-04	.128925D-03
23	.577642D-02	.333523D-02	-.142644D-03	-.394861D-03	.454596D-04
24	-.333523D-02	-.650160D-02	-.144393D-03	.597160D-03	-.944623D-03
25	-.142644D-03	.144393D-03	-.388672D-04	.142723D-03	-.313315D-04
26	-.394861D-03	-.597160D-03	.142723D-03	-.919335D-04	.765913D-04
27	-.454596D-04	-.944623D-03	.313315D-04	-.765913D-04	.232917D-03
28	-.220257D-02	-.364270D-02	-.239590D-03	.147466D-02	.139822D-02
29	.112411D-01	.166943D-01	.308264D-03	-.118348D-02	.142912D-03
30	.202050D-03	-.740705D-03	.548657D-03	-.499414D-03	.792260D-03
31	.141406D-02	-.683412D-02	.805356D-03	-.163495D-02	.517442D-04
32	.166256D-01	.115539D-01	-.164749D-03	-.150070D-02	-.172073D-03
33	.479393D-03	-.555306D-02	.551762D-03	-.299305D-03	-.391630D-03
	16	17	18	19	20
16	.617777D+00				
17	.170722D+00	.451316D+00			
18	-.483912D-01	.515941D-02	.290680D-01		
19	-.497093D+00	-.201548D+00	.256741D-01	.476088D+00	
20	-.130280D+00	-.122521D+00	-.769595D-02	.176300D+00	.148198D+00
21	.216788D-01	.998894D-03	-.201809D-03	-.190741D-01	-.146645D-02
22	-.106063D+00	.583503D-01	.755363D-02	.149956D-01	-.415297D-01
23	-.583503D-01	-.292865D+00	.929413D-02	.201295D-01	-.216505D-01
24	.755363D-02	-.929413D-02	.137224D-01	-.395307D-02	.424555D-02
25	.149956D-01	-.201295D-01	-.395307D-02	.724460D-02	-.116038D-02
26	.415297D-01	-.216505D-01	-.424555D-02	.116038D-02	-.150787D-02
27	-.349697D-02	.101562D-02	-.105345D-01	-.213753D-03	-.333155D-03
28	-.403193D-02	-.141408D-02	.683411D-02	.805366D-03	.163499D-02
29	.974094D-02	.166230D-01	.115605D-01	.159416D-03	-.150083D-02
30	.366158D-02	.479386D-03	-.555314D-02	-.551785D-03	-.299333D-03
31	.299026D-02	.220260D-02	.364269D-02	-.239662D-03	-.147465D-02
32	.655354D-02	.112529D-01	.166936D-01	-.285560D-03	-.117657D-02
33	-.259126D-03	.202050D-03	-.740666D-03	-.548702D-03	-.499384D-03
	21	22	23	24	25
21	.731757D-05				
22	-.349697D-02	.617777D+00			
23	-.101562D-02	-.170722D+00	.451316D+00		
24	-.105345D-01	-.483912D-01	-.515941D-02	.290680D-01	
25	-.213753D-03	-.497093D+00	.201548D+00	.256741D-01	.476088D+00
26	.333155D-03	.130280D+00	-.122521D+00	.769595D-02	-.176300D+00
27	.639099D-02	.216788D-01	-.998894D-03	-.201809D-03	-.190741D-01
28	-.517718D-04	-.403191D-02	.141406D-02	.683412D-02	.805356D-03
29	-.177656D-03	-.973425D-02	.166256D-01	-.115539D-01	-.164749D-03
30	-.391610D-03	.366154D-02	-.479393D-03	-.555306D-02	-.551762D-03
31	-.139818D-02	.299014D-02	-.220257D-02	.364270D-02	-.239590D-03
32	.146439D-03	-.657926D-02	.112411D-01	-.166943D-01	.308264D-03
33	.792289D-03	-.259224D-03	-.202050D-03	-.740705D-03	-.548657D-03
	26	27	28	29	30
26	.148198D+00				

```

27 .146645D-02 .731757D-05
28 -.163495D-02 -.517442D-04 .288303D+00
29 -.150070D-02 .172073D-03 -.198104D-04 .395248D-01
30 .299305D-03 -.391630D-03 -.878358D-01 .000000D+00 .183743D+00 31
.147466D-02 -.139822D-02 -.244391D+00 .177866D-04 .242766D-01
32 -.118348D-02 -.142912D-03 .177866D-04 .269912D-01 .283865D-05
33 .499414D-03 .792260D-03 -.242766D-01 -.283865D-05 .587947D-01
      31          32          33
31 .288303D+00
32 -.198104D-04 .395248D-01
33 .878358D-01 .000000D+00 .183743D+00

```

Population analysis using the SCF density.

Orbital Symmetries:

```

Occupied (A1) (A1) (B1) (B2) (A1) (B2) (A1) (A2) (B1) (A1)
          (B2) (A1) (A1) (B1) (B2) (A1) (B2) (A1) (B1) (A2)
          (B2) (A1) (B2) (A1) (B2) (A1) (B1) (A1) (B2) (A2)
          (A1) (B1) (A2) (B1) (A1) (A1) (B2) (A2)
Virtual  (B1) (A1) (B2) (A2) (A2) (B1) (B2) (A1) (B1) (A2)
          (B2) (A1) (A1) (B2) (B1) (A2) (B1) (A1) (B2) (B1)
          (A1) (A1) (A2) (B2) (A2) (B1) (B2) (B1) (B2) (A1)
          (A2) (A1) (B2) (A1) (B2) (A1) (A2) (B1) (A2) (B1)
          (B2) (A1) (B1) (A2) (A1) (B2) (A1) (B2) (B2) (B1)
          (A1) (A2) (A1) (A1) (B2) (A1) (B2) (A1) (B1) (A2)
          (B1) (A1) (B1) (A2) (A1) (B2) (B2) (A2) (A1) (A2)
          (B1) (B2) (B1) (A2) (A1) (B2) (B1) (B2) (A1) (A1)
          (B1) (B2) (A1) (B2) (B1) (A1) (A2) (B2) (A1) (A1)
          (A1)

```

The electronic state is 1-A1.

```

α occ. eigenvalues-- -240.86394 -29.44742 -25.17268 -25.16199 -25.16090
α occ. eigenvalues -- -20.90234 -20.90234 -20.90206 -20.90205 -20.74324
α occ. eigenvalues -- -20.74293 -4.12770 -2.79927 -2.78952 -2.78728
α occ. eigenvalues -- -1.77093 -1.76805 -1.57391 -1.50058 -1.49868
α occ. eigenvalues -- -1.26000 -1.08050 -1.06647 -.93242 -.91336
α occ. eigenvalues -- -.87851 -.87528 -.85780 -.85719 -.85449
α occ. eigenvalues -- -.81676 -.75123 -.74218 -.74080 -.68818
α occ. eigenvalues -- -.65678 -.62276 -.56754
α virt. eigenvalues -- -.07743 -.07570 -.06989 -.06611 -.05487
α virt. eigenvalues -- -.05444 -.00986 .01484 .06737 .07162
α virt. eigenvalues -- .12332 .15460 .33227 .33318 .38362
α virt. eigenvalues -- .39735 .59408 .59941 .62551 .73532
α virt. eigenvalues -- .79374 .79735 .80601 .82882 .85452
α virt. eigenvalues -- .85870 .87854 .90431 .90611 .93897
α virt. eigenvalues -- .97598 .99803 1.01303 1.03785 1.10719
α virt. eigenvalues -- 1.17165 1.18624 1.22456 1.26188 1.31324
α virt. eigenvalues -- 1.37674 1.48205 1.55902 1.59530 1.64135

```

α virt. eigenvalues -- 1.69498 1.71170 1.76380 2.22199 2.24761
 α virt. eigenvalues -- 2.25113 2.26188 2.66660 4.68723 4.70211
 α virt. eigenvalues -- 4.84098 4.92756 4.96843 5.05892 5.09581
 α virt. eigenvalues -- 5.11351 5.14509 5.14926 5.24951 5.25416
 α virt. eigenvalues -- 5.28005 5.32224 5.39770 5.52943 5.53043
 α virt. eigenvalues -- 5.53086 5.58543 5.63660 5.66707 5.68578
 α virt. eigenvalues -- 5.94870 7.29485 7.50908 7.66557 24.01692
 α virt. eigenvalues -- 31.50772 31.68207 31.79044 51.11159 51.12748
 α virt. eigenvalues -- 51.13629 51.14021 51.26910 51.30499 136.13644
 α virt. eigenvalues -- 718.97058

Condensed to atoms (all electrons):

		1	2	3	4	5	6
1 Mn		23.003478	.002211	-.000390	.002211	-.000390	.002211
2 O		.002211	8.299543	.249293	-.059634	-.020327	.000147
3 H		-.000390	.249293	.255695	-.020327	-.000822	-.000060
4 O		.002211	-.059634	-.020327	8.299543	.249293	-.000221
5 H		-.000390	-.020327	-.000822	.249293	.255695	.000137
6 O		.002211	.000147	-.000060	-.000221	.000137	8.299543
7 H		-.000390	-.000060	.000004	.000137	-.000011	.249293
8 O		.002211	-.000221	.000137	.000147	-.000060	-.059634
9 H		-.000390	.000137	-.000011	-.000060	.000004	-.020327
10 O		.131454	.000121	.000657	.000121	.000657	-.000823
11 O		.131454	-.000823	.000003	-.000823	.000003	.000121

		7	8	9	10	11
1 Mn		-.000390	.002211	-.000390	.131454	.131454
2 O		-.000060	-.000221	.000137	.000121	-.000823
3 H		.000004	.000137	-.000011	.000657	.000003
4 O		.000137	.000147	-.000060	.000121	-.000823
5 H		-.000011	-.000060	.000004	.000657	.000003
6 O		.249293	-.059634	-.020327	-.000823	.000121
7 H		.255695	-.020327	-.000822	.000003	.000657
8 O		-.020327	8.299543	.249293	-.000823	.000121
9 H		-.000822	.249293	.255695	.000003	.000657
10 O		.000003	-.000823	.000003	8.376250	-.053591
11 O		.000657	.000121	.000657	-.053591	8.376250

Total atomic charges:

		1
1 Mn		1.726330
2 O		-.470389
3 H		.515822
4 O		-.470389
5 H		.515822
6 O		-.470389
7 H		.515822
8 O		-.470389
9 H		.515822
10 O		-.454029
11 O		-.454029

Sum of Mulliken charges= 1.00000

Atomic charges with hydrogens summed into heavy atoms:

		1
1 Mn		1.726330

```

2 O      .045432
3 H      .000000
4 O      .045432
5 H      .000000
6 O      .045432
7 H      .000000
8 O      .045432
9 H      .000000
10 O     -.454029
11 O     -.454029
Sum of Mulliken charges= 1.00000
Electronic spatial extent (au): <R**2>= 870.5663
Charge= 1.0000 electrons
Dipole moment (Debye):
  X=      .0000      Y=      .0000      Z=     -8.4417      Tot=      8.4417
Quadrupole moment (Debye-Ang):
  XX=   -37.6092      YY=    -6.2904      ZZ=   -58.3188
  XY=      .0000      XZ=      .0000      YZ=      .0000
Octapole moment (Debye-Ang**2):
  XXX=      .0000      YYY=      .0000      ZZZ=   -28.8798      XYY=      .0000
  XXY=      .0000      XXZ=   -8.5652      XZZ=      .0000      YZZ=      .0000
  YYZ=   -51.5741      XYZ=      .0000
Hexadecapole moment (Debye-Ang**3):
  XXXX=  -90.1173      YYYY=  -106.5795      ZZZZ=  -486.3951      XXXY=      .0000
  XXXZ=      .0000      YYYY=      .0000      YYYZ=      .0000      ZZZX=      .0000
  ZZZY=      .0000      XYY=   -25.4013      XXZZ=  -84.9327      YYZZ=  -107.1034
  XXYZ=      .0000      YYXZ=      .0000      ZZXY=      .0000
N-N= 5.744437257083D+02 E-N=-4.937608502222D+03 KE= 1.601183396169D+03
Symmetry A1  KE= 1.038742289247D+03
Symmetry A2  KE= 8.012342937114D+01
Symmetry B1  KE= 2.064309394224D+02
Symmetry B2  KE= 2.758867381286D+02
Exact polarizability: 32.478      .000 38.187      .000      .000 34.774
Approx polarizability: 27.631      .000 33.140      .000      .000 30.614

Change starts when someone sees the next step.
-- William Drayton
Job cpu time: 0 days 1 hours 10 minutes 26.9 seconds.
File lengths (MBytes): RWF= 44 Int= 0 D2E= 0 Chk= 3 Scr= 1
Normal termination of Gaussian 94

```

APPENDIX B. ENTROPY CALCULATION FOR THE PEROXIDE SPECIES

B.1. TRANSLATIONAL ENTROPY

If we assume the adsorbed peroxide species is totally mobile on the manganese oxide surface, it can be approximated as a two-dimensional ideal gas and its translational entropy can be expressed as:

$$St^2 = R \ln \left[\frac{A(2\pi mkT)}{Nh^2} \right] + 2R \quad (\text{B.1})$$

Here $a = \frac{A}{N}$ is the area of the adsorbed species, m is its mass of. Since a is the area per species, it can be approximated as

$$(V)^{\frac{2}{3}} = \left(\frac{kT}{p} \right)^{\frac{2}{3}} \quad (\text{B.2})$$

So for a O_2^{2-} species at 300 K,

$$\begin{aligned} St^2/J \text{ mol}^{-1} \text{ K}^{-1} &= R \ln \left[\frac{(2\pi mkT) \left(\frac{kT}{p} \right)^{\frac{2}{3}}}{h^2} \right] + 2R \\ &= 8.314 \times \ln \left[\frac{\left(2 \times 3.142 \times \frac{32.0 \times 10^{-3}}{6.02 \times 10^{23}} \times 1.38 \times 10^{-23} \times 300 \right) \left(\frac{1.38 \times 10^{-23} \times 300}{1.01 \times 10^5} \right)^{\frac{2}{3}}}{(6.626 \times 10^{-34})^2} \right] + 2 \times 8.314 \\ &= 104.2 \end{aligned}$$

Hence the translational entropy of the adsorbed peroxide species is $104.2 \text{ J mol}^{-1} \text{ K}^{-1}$.

B.2. ROTATIONAL ENTROPY

If the adsorbed peroxide can be approximated as a one-dimensional rotor (Figure B1), the 1-d moment of inertia can be calculated as $I = m_0 d^2/2$. Here m_0 is the mass of an oxygen atom

and d is the bond distance between the oxygen atoms. The MO calculations showed the bond distance d equals 0.146 nm. So

$$I = \left(\frac{16.02 \times 10^{-3} \text{ kg}}{6.02 \times 10^{23}} \right) \frac{(0.146 \times 10^{-9} \text{ m})^2}{2}$$

$$= 2.836 \times 10^{-46} \text{ kg m}^2$$

Rotational entropy can then be calculated as

$$S_r^1 = R \ln \left[\frac{(8\pi^2 kT)^{1/2} I^{1/2}}{\sigma h} \right] + \frac{1}{2} R \quad (\text{B.3})$$

For the peroxide species, $\sigma = 2$. So at 300 K,

$$S_r^1 / J \text{ mol}^{-1} \text{ K}^{-1} = 8.134 \times \ln \left[\frac{(8(3.142)^2 (1.381 \times 10^{-23}) (300))^{1/2} (2.836 \times 10^{-46})^{1/2}}{2 \times 6.626 \times 10^{-34}} \right] + \frac{1}{2} \times 8.314$$

$$= 20.6$$

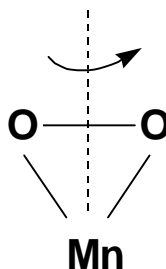


Figure B1 Schematic of the peroxide species as a 1-D rigid rotor.

APPENDIX C. STEADY STATE AND TRANSIENT KINETIC RESULTS FOR OZONE DECOMPOSITION

Table C.1 Transient data (For Figures 3.7 and 3.8)

Ozone Adsorption and Desorption Kinetics on a 10%MnO ₂ /Al ₂ O ₃ Catalyst					
281 K	Adsorption(P _{O₃} /g m ⁻³)			Desorption	
time/s	2.12	4.63	10.03	21098	33637
0	3506	5529	7233	22505	32254
30	8934	11429	12157	17147	31123
60	11963	14738	16827	16053	28448
90	12569	18909	17566	14477	25093
120	14814	15926	19437	11871	23190
150	14823	16331	19726	10843	22838
180	14604	16638	18979	9353	20614
210	14232	18131	20149	9751	20664
240	15836	17674	20861	9424	16203
270	13781	18706	22217	6310	15958
300	16245	19342	21606	7873	15620
360	15007	20380	21316	5889	16298
420	17071	20010	22502	6865	14595
480	16308	19412	22234	3364	13494
540	15376	19785	23918	4587	12599
600	16220	22555	22501	3285	12316
720	18470	22562	22575	4468	9522
840	15329	23240	23082	5810	11752
960	19297	21157	24719	2944	10775
1080	19343	23938	24550	2960	8382
1200	18753	21797	24372	3149	10248
1320	18245		25033		9027
1440	17784		24511		6404
1560	17884		24677		7244
1680	19897		25490		7554
1800					5326
1920					5927
2040					5288
2160					5258

296 K	Adsorption($P_{O_3}/g\ m^{-3}$)			Desorption	
time/s	1.55	4.20	8.50	23212	29801
0	0	5874	4381	23691	29276
30	4201	9942	12432	24352	25126
60	7415	12309	12942	21103	26168
90	9376	14601	16520	18604	
120	10017	15779	16384	16908	20081
150	11708	16594	18795	14515	18528
180	10122	17393	18398	12452	16209
210	12974	17413	19964	13493	13896
240	13107	20157	20343	12388	12854
270	14996	19375	23228	11087	13903
300	14527	20868	20444	10096	13984
360	16551	22489	22639	10582	12674
420	16563	21996	22242	8252	9732
480	18052	23073	23780	9727	9348
540	16049	22038	26091	9202	8634
600	19349	23516	24199	8361	8114
720	18312	23962	25770	5572	6553
840	21617	25505	28302	5690	7393
960	20370	26457	26292	5658	5290
1080	22176	25965	28858	4458	5941
1200	20975	26643	28887	4362	3220
1320	20487	27751	26804	4595	4574
1440	21057	26553	28611	3589	4627
1560	22857	26935	27146	2743	4547
1680	22098	26229	28911	3510	2097
318 K	Adsorption($P_{O_3}/g\ m^{-3}$)			Desorption	
time/s	2.05	5.13	11.29	20840	31438
0	1848	5393	7712	19589	31591
30	6634	11903	18864	17010	30914
60	8629	15899	21690	16493	22892
90	9443	16132	23627	12098	20695
120	9272	18845	24607	12949	17473
150	12067	20479	24645	9730	14408
180	12995	20170	23929	10048	12897
210	12832	20385	26733	9095	11573
240	12312	20566	25809	6494	12079
270	13752	20150	27745	6991	10073
300	13864	20741	27749	7103	10289

360	14306	21538	27872	6986	8513
420	15090	23671	28645	7033	8703
480	13366	23281	29036	6349	6435
540	14463	23397	27263	3971	6603
600	15558	22747	29794	3570	5654
720	15627	22890	28141	3725	5206
840	16919	24066	30860	2789	4679
960	18303	24540	31277	3068	3196
1080	17289				3653
1200	17043				2268
1320	18810				
1440	17920				
1560	18217				
1680	19091				
340 K	Adsorption($P_{O_3}/g\ m^{-3}$)			Desorption	
time/s	0.92	2.04	4.99	15380	16002
0	3791	2983	4314	13677	18068
30	7899	9384	12669	13143	15084
60	7530	11585	12383	9806	9944
90		13158	15273	8683	9724
120	9751	13181	15311	7014	8008
150	12110	11932	14111	6298	6082
180	10593	14534	16757	7029	4557
210	10868	14254	17680	5469	7125
240	11768	13493	16861	4406	3877
270	9410	15216	19047	4220	4435
300	11645	14558	17024	3173	3391
360	10613	14998	15596		3329
420	12858	15560	17394		3154
480	10733	14274	20091		
540	11445	14171	17659		
600	10428	13523	19062		
720	10685	14016	17475		

Ozone Adsorption and Desorption Kinetics on a 10%MnO₂/Al₂O₃ Catalyst					
281 K	Adsorption(P_{O_3}/Pa)			Desorption	
time/s	100	218	472	0.6272	1.0000
0	0.1042	0.1644	0.2150	0.6691	0.9589
30	0.2656	0.3398	0.3614	0.5098	0.9253

60	0.3557	0.4382	0.5003	0.4772	0.8457
90	0.3737	0.5622	0.5222	0.4304	0.7460
120	0.4404	0.4735	0.5778	0.3529	0.6894
150	0.4407	0.4855	0.5864	0.3224	0.6790
180	0.4342	0.4946	0.5642	0.2781	0.6128
210	0.4231	0.5390	0.5990	0.2899	0.6143
240	0.4708	0.5254	0.6202	0.2802	0.4817
270	0.4097	0.5561	0.6605	0.1876	0.4744
300	0.4830	0.5750	0.6423	0.2341	0.4644
360	0.4461	0.6059	0.6337	0.1751	0.4845
420	0.5075	0.5949	0.6690	0.2041	0.4339
480	0.4848	0.5771	0.6610	0.1000	0.4012
540	0.4571	0.5882	0.7111	0.1364	0.3746
600	0.4822	0.6705	0.6689	0.0977	0.3661
720	0.5491	0.6708	0.6711	0.1328	0.2831
840	0.4557	0.6909	0.6862	0.1727	0.3494
960	0.5737	0.6290	0.7349	0.0875	0.3203
1080	0.5751	0.7117	0.7299	0.0880	0.2492
1200	0.5575	0.6480	0.7246	0.0936	0.3047
1320	0.5424		0.7442		0.2684
1440	0.5287		0.7287		0.1904
1560	0.5317		0.7336		0.2154
1680	0.5915		0.7578		0.2246
1800					0.1583
1920					0.1762
2040					0.1572
2160					0.1563
296 K	Adsorption(P_{O_2}/Pa)			Desorption	
time/s	73	198	400	0.4384	0.5628
0	0.0000	0.1109	0.0827	0.4474	0.5529
30	0.0793	0.1878	0.2348	0.4599	0.4745
60	0.1400	0.2325	0.2444	0.3985	0.4942
90	0.1771	0.2757	0.3120	0.3513	0.0000
120	0.1892	0.2980	0.3094	0.3193	0.3792
150	0.2211	0.3134	0.3550	0.2741	0.3499
180	0.1912	0.3285	0.3475	0.2352	0.3061
210	0.2450	0.3289	0.3770	0.2548	0.2624
240	0.2475	0.3807	0.3842	0.2340	0.2428
270	0.2832	0.3659	0.4387	0.2094	0.2626
300	0.2743	0.3941	0.3861	0.1907	0.2641

360	0.3126	0.4247	0.4275	0.1998	0.2394
420	0.3128	0.4154	0.4200	0.1558	0.1838
480	0.3409	0.4357	0.4491	0.1837	0.1765
540	0.3031	0.4162	0.4927	0.1738	0.1631
600	0.3654	0.4441	0.4570	0.1579	0.1532
720	0.3458	0.4525	0.4867	0.1052	0.1238
840	0.4082	0.4817	0.5345	0.1075	0.1396
960	0.3847	0.4997	0.4965	0.1069	0.0999
1080	0.4188	0.4904	0.5450	0.0842	0.1122
1200	0.3961	0.5032	0.5455	0.0824	0.0608
1320	0.3869	0.5241	0.5062	0.0868	0.0864
1440	0.3977	0.5015	0.5403	0.0678	0.0874
1560	0.4317	0.5087	0.5127	0.0518	0.0859
1680	0.4173	0.4953	0.5460	0.0663	0.0396
318 K	Adsorption(PO3)			Desorption	
time/s	97	242	532	0.4021	0.6065
0	0.0357	0.1040	0.1488	0.3779	0.6095
30	0.1280	0.2296	0.3639	0.3282	0.5964
60	0.1665	0.3067	0.4185	0.3182	0.4417
90	0.1822	0.3112	0.4558	0.2334	0.3993
120	0.1789	0.3636	0.4748	0.2498	0.3371
150	0.2328	0.3951	0.4755	0.1877	0.2780
180	0.2507	0.3891	0.4617	0.1939	0.2488
210	0.2476	0.3933	0.5158	0.1755	0.2233
240	0.2375	0.3968	0.4979	0.1253	0.2330
270	0.2653	0.3888	0.5353	0.1349	0.1943
300	0.2675	0.4002	0.5354	0.1370	0.1985
360	0.2760	0.4155	0.5377	0.1348	0.1642
420	0.2911	0.4567	0.5527	0.1357	0.1679
480	0.2579	0.4492	0.5602	0.1225	0.1242
540	0.2790	0.4514	0.5260	0.0766	0.1274
600	0.3002	0.4389	0.5748	0.0689	0.1091
720	0.3015	0.4416	0.5429	0.0719	0.1004
840	0.3264	0.4643	0.5954	0.0538	0.0903
960	0.3531	0.4735	0.6034	0.0592	0.0617
1080	0.3336				0.0705
1200	0.3288				0.0438
1320	0.3629				
1440	0.3457				
1560	0.3515				

1680	0.3683				
340 K	Adsorption(P_{O_3}/Pa)			Desorption	
time/s	43	96	235	0.3195	0.3324
0	0.0788	0.0620	0.0896	0.2841	0.3753
30	0.1641	0.1949	0.2632	0.2730	0.3134
60	0.1564	0.2407	0.2572	0.2037	0.2066
90	0.0000	0.2733	0.3173	0.1804	0.2020
120	0.2026	0.2738	0.3181	0.1457	0.1664
150	0.2516	0.2479	0.2931	0.1308	0.1263
180	0.2201	0.3019	0.3481	0.1460	0.0947
210	0.2258	0.2961	0.3673	0.1136	0.1480
240	0.2445	0.2803	0.3503	0.0915	0.0805
270	0.1955	0.3161	0.3957	0.0877	0.0921
300	0.2419	0.3024	0.3537	0.0659	0.0704
360	0.2205	0.3116	0.3240		0.0692
420	0.2671	0.3232	0.3613		0.0655
480	0.2230	0.2965	0.4174		
540	0.2378	0.2944	0.3668		
600	0.2166	0.2809	0.3960		
720	0.2220	0.2912	0.3630		

Table C.2 Steady State Kinetic Data (For Figures 3.2 and 3.3)

Steady State Ozone Decomposition Data											
281 K			296 K			318 K			340 K		
PO3	Rate	Area	PO3	Rate	Area	PO3	Rate	Area	PO3	Rate	Area
0.375	0.075	17354	0.10	0.00	13334	0.42	0.017	14346	0.35	0.05	8137
0.960	0.125	19045	0.40	0.10	18563	1.13	0.23	17911	0.92	0.22	10993
2.12	0.30	19897	1.73	0.23	23184	2.05	0.25	19091	2.04	0.68	14418
4.63	0.58	21797	4.28	0.53	25872	5.13	0.99	24540	4.99	0.98	17789
10.03	1.08	25490	10.05	1.50	33068	11.29	1.85	29288	10.35	2.83	14917
19.78	2.78	25406	19.83	2.33	36564	22.35	4.53	29848	19.57	3.89	19372
31.49	3.84	29827	31.93	3.06	39895	33.93	5.28	28865	31.95	6.62	20479
40.00	5.02	32276	40.57	4.60	39698	41.40	7.20	30848	39.98	9.40	23345
44.45	5.85	32763							45.27	10.77	22231
281 K			296 K			318 K			340 K		
PO3/Pa	Rate/ μmols^{-1}	Area	PO3/Pa	Rate/ μmols^{-1}	Area	PO3/Pa	Rate/ μmols^{-1}	Area	PO3/Pa	Rate/ μmols^{-1}	Area
17.7	0.026	27319	4.7	0.000	13334	19.8	0.006	14656	16.5	0.017	8951
45.2	0.043	29981	18.8	0.035	18563	53.2	0.080	18298	43.3	0.076	12092
99.9	0.104	31322	81.5	0.080	23184	96.6	0.087	19503	96.1	0.234	15860
218.1	0.201	34313	201.6	0.184	25872	241.6	0.344	25070	235.0	0.340	19568
472.4	0.375	40126	473.4	0.521	33068	531.8	0.642	29921	487.5	0.982	16409
931.6	0.965	39994	934.0	0.809	36564	1052.7	1.572	30493	921.7	1.350	21309

1483.2	1.332	46954	1503.9	1.062	39895	1598.1	1.832	29488	1504.8	2.297	22527
1884.0	1.742	50809	1910.8	1.596	39698	1949.9	2.498	31514	1883.1	3.262	25680
2093.6	2.030	51576							2132.2	3.737	24454
281 K			296 K			318 K			340 K		
ln(P)	ln(R)	Theta									
2.871	-6.409	0.516	1.550	#NUM!	0.252	2.985	-7.893	0.277	2.802	-6.814	0.169
3.811	-5.898	0.566	2.936	-6.121	0.351	3.974	-5.288	0.346	3.769	-5.333	0.228
4.604	-5.022	0.592	4.400	-5.288	0.438	4.570	-5.205	0.368	4.565	-4.211	0.300
5.385	-4.363	0.648	5.306	-4.453	0.489	5.487	-3.828	0.473	5.460	-3.839	0.370
6.158	-3.741	0.758	6.160	-3.413	0.625	6.276	-3.203	0.565	6.189	-2.778	0.310
6.837	-2.796	0.755	6.839	-2.973	0.691	6.959	-2.308	0.576	6.826	-2.460	0.402
7.302	-2.473	0.887	7.316	-2.700	0.753	7.377	-2.155	0.557	7.316	-1.928	0.425
7.541	-2.205	0.960	7.555	-2.292	0.750	7.576	-1.844	0.595	7.541	-1.578	0.485
7.647	-2.052	0.974							7.665	-1.442	0.462
281 K			296 K			318 K			340 K		
1e3/P	R / s⁻¹	1/Theta									
56.62	0.0016	1.9383	212.31	0.0000	3.9711	50.55	0.0004	3.6130	60.66	0.0011	5.9159
22.12	0.0027	1.7662	53.08	0.0022	2.8525	18.79	0.0051	2.8938	23.08	0.0048	4.3789
10.01	0.0066	1.6905	12.27	0.0051	2.2839	10.36	0.0055	2.7150	10.41	0.0148	3.3387
4.59	0.0127	1.5432	4.96	0.0116	2.0467	4.14	0.0217	2.1121	4.25	0.0215	2.7060
2.12	0.0237	1.3196	2.11	0.0329	1.6013	1.88	0.0406	1.7697	2.05	0.0622	3.2270
1.07	0.0611	1.3240	1.07	0.0512	1.4482	0.95	0.0995	1.7365	1.08	0.0854	2.4849
0.67	0.0843	1.1277	0.66	0.0672	1.3273	0.63	0.1160	1.7957	0.66	0.1454	2.3506
0.53	0.1102	1.0422	0.52	0.1010	1.3338	0.51	0.1581	1.6802	0.53	0.2064	2.0620
0.48	0.1285	1.0267							0.47	0.2365	2.1653

Least Square Fitting for Steady State Coverage Data											
$10^3 T^{-1}/K^{-1}$	ln(P/Pa)	θ	$10^3 T^{-1}/K^{-1}$	ln(P/Pa)	θ	$10^3 T^{-1}/K^{-1}$	ln(P/Pa)	θ	$10^3 T^{-1}/K^{-1}$	ln(P/Pa)	θ
3.559	2.871	0.516	3.378	1.550	0.252	3.145	2.985	0.277	2.941	2.802	0.169
3.559	3.811	0.566	3.378	2.936	0.351	3.145	3.974	0.346	2.941	3.769	0.228
3.559	4.604	0.592	3.378	4.400	0.438	3.145	4.570	0.368	2.941	4.565	0.300
3.559	5.385	0.648	3.378	5.306	0.489	3.145	5.487	0.473	2.941	5.460	0.370
3.559	6.158	0.758	3.378	6.160	0.625	3.145	6.276	0.565	2.941	6.189	0.310
3.559	6.837	0.755	3.378	6.839	0.691	3.145	6.959	0.576	2.941	6.826	0.402
3.559	7.302	0.887	3.378	7.316	0.753	3.145	7.377	0.557	2.941	7.316	0.425
3.559	7.541	0.960	3.378	7.555	0.750	3.145	7.576	0.595	2.941	7.541	0.485
3.559	7.647	0.974							2.941	7.665	0.462
32.03	52.16	6.66	27.02	42.06	4.35	25.16	45.20	3.76	26.47	52.13	3.15
114.00	326.29	23.69	91.29	253.86	14.69	79.13	275.33	11.82	77.85	326.75	9.27
	185.62	40.85		142.09	25.69		142.17	22.65		153.32	19.69

110.68	191.56	17.91									
362.26	1182.2	59.46									
	623.20	108.88									
Least Square Fitting for Steady State Rate Data											
$10^3 T^{-1}/K^{-1}$	lnP	ln(R)	$10^3 T^{-1}/K^{-1}$	lnP	ln(R)	$10^3 T^{-1}/K^{-1}$	lnP	ln(R)	$10^3 T^{-1}/K^{-1}$	lnP	ln(R)
3.559	2.871	-3.649	3.378	2.936	-3.361	3.145	2.985	-5.133	2.941	2.802	-4.054
3.559	3.811	-3.138	3.378	4.400	-2.528	3.145	3.974	-2.528	2.941	3.769	-2.573
3.559	4.604	-2.262	3.378	5.306	-1.693	3.145	4.570	-2.445	2.941	4.565	-1.451
3.559	5.385	-1.603	3.378	6.160	-0.653	3.145	5.487	-1.068	2.941	5.460	-1.079
3.559	6.158	-0.981	3.378	6.839	-0.213	3.145	6.276	-0.443	2.941	6.189	-0.018
3.559	6.837	-0.036	3.378	7.316	0.060	3.145	6.959	0.452	2.941	6.826	0.300
3.559	7.302	0.287	3.378	7.555	0.468	3.145	7.377	0.605	2.941	7.316	0.832
3.559	7.541	0.555				3.145	7.576	0.916	2.941	7.541	1.182
3.559	7.647	0.708							2.941	7.665	1.318
32.03	52.16	-10.12	23.65	40.51	-7.92	25.16	45.20	-9.64	26.47	52.13	-5.54
114.00	326.29	-36.01	79.88	251.45	-26.75	79.13	275.33	-30.33	77.85	326.75	-16.30
	185.62	-36.07		136.85	-31.48		142.17	-30.63		153.32	-6.53
107.31	190.01	-33.23									
350.85	1179.8	-109.40									
	617.96	-104.72									

APPENDIX D. LEAST SQUARE FITTING OF THE STEADY STATE OZONE DECOMPOSITION KINETICS USING THE NON-UNIFORM SURFACE TREATMENT

As shown in chapter 3, the steady state coverage and rate can be expressed as follows using a non-uniform surface treatment.

$$\theta_{ss} = \frac{1}{g+h} \ln \left[\frac{k_a^0(O_3)}{k_d^0} \right] \quad (D.1)$$

$$r_{ss} = k_d^0 \left[\left(\frac{k_a^0}{k_d^0} \right) (O_3) \right]^{\frac{h}{g+h}} \quad (D.2)$$

Using these equations, a least square fitting was carried out using the data set given in appendix C, and this appendix describes the details of the fitting.

(a) For the steady state coverage data,

$$\Delta = \sum_{i=1}^n \left[\theta_i - \frac{1}{g+h} \ln \left(\frac{k_a^0(O_3)}{k_d^0} \right) \right]^2 \quad (D.3)$$

$$= \sum_{i=1}^n \left[\theta_i - \frac{1}{g+h} \ln \left(\frac{\left(A_a^0 \exp \left(-\frac{E_a^0}{RT} \right) \right)}{\left(A_d^0 \exp \left(-\frac{E_d^0}{RT} \right) \right)} P_{O_3} \right) \right]^2 \quad (D.4)$$

$$= \sum_{i=1}^n \left[\theta_i - \frac{1}{g+h} \ln \left(\frac{A_a^0}{A_d^0} \exp \left(-\frac{(E_a^0 - E_d^0)}{RT} \right) P_{O_3} \right) \right]^2 \quad (D.5)$$

Let

$$\left\{ \begin{array}{l} \frac{1}{g+h} = u \\ \ln(A_a^0/A_d^0) = v \\ \frac{E_a^0 - E_d^0}{R} = w \end{array} \right. \quad (D.6)$$

$$\text{This results in } \Delta = \sum_{i=1}^n \left[\theta_i - u \left(v - \frac{w}{T_i} + \ln(P_i) \right) \right]^2 \quad (\text{D.7})$$

$$\text{Let } 1/T_i = x_i, \text{ and } \ln(P_i) = y_i, \quad (\text{D.8})$$

$$\text{then } \Delta = \sum_{i=1}^n \left[\theta_i - u(v - wx_i + y_i) \right]^2 \quad (\text{D.9})$$

$$\text{Let } uv = a, uw = b, \text{ and } c=u, \quad (\text{D.10})$$

$$\text{then } \Delta = \sum_{i=1}^n \left[\theta_i - a + bx_i - cy_i \right]^2 \quad (\text{D.11})$$

$$\text{For the least square fit, } \frac{\partial \Delta}{\partial a} = \frac{\partial \Delta}{\partial b} = \frac{\partial \Delta}{\partial c} = 0 \quad (\text{D.12})$$

$$\frac{\partial \Delta}{\partial a} = 0 \Rightarrow \sum_{i=1}^n (\theta_i - a + bx_i - cy_i) = 0 \quad (\text{D.13})$$

$$\sum_{i=1}^n \theta_i + na + b \sum_{i=1}^n x_i - c \sum_{i=1}^n y_i = 0 \quad (\text{D.14})$$

$$\frac{\partial \Delta}{\partial b} = 0 \Rightarrow \sum_{i=1}^n [(\theta_i - a + bx_i - cy_i)(x_i)] = 0 \quad (\text{D.15})$$

$$\sum_{i=1}^n (\theta_i x_i) - a \sum_{i=1}^n x_i + b \sum_{i=1}^n x_i^2 - c \sum_{i=1}^n (x_i y_i) = 0 \quad (\text{D.16})$$

$$\frac{\partial \Delta}{\partial c} = 0 \Rightarrow \sum_{i=1}^n [(\theta_i - a + bx_i - cy_i)(-y_i)] = 0 \quad (\text{D.17})$$

$$\sum_{i=1}^n (\theta_i y_i) - a \sum_{i=1}^n y_i + b \sum_{i=1}^n (x_i y_i) - c \sum_{i=1}^n y_i^2 = 0 \quad (\text{D.18})$$

From the data set, the following can be obtained:

$$\sum_{i=1}^n x_i = 110.68 \quad \sum_{i=1}^n x_i^2 = 362.26 \quad \sum_{i=1}^n \theta_i = 17.91$$

$$\sum_{i=1}^n y_i = 191.56 \quad \sum_{i=1}^n y_i^2 = 1182.2 \quad \sum_{i=1}^n x_i y_i = 623.20$$

$$\sum_{i=1}^n \theta_i x_i = 59.46 \quad \sum_{i=1}^n \theta_i y_i = 108.88$$

So this results in

$$\begin{cases} 34a - 110.68b + 191.56c = 17.91 \\ 110.68a - 362.26b + 623.20 = 59.46 \\ 191.56a - 623.20b + 1182.2c = 108.88 \end{cases} \quad (\text{D.19})$$

Solving (Eq. 19),

$$\begin{cases} a = -1.8916 \\ b = -0.6050 \\ c = 0.07968 \end{cases} \quad (\text{D.20})$$

By substituting uv, uw, and u for a, b, and c respectively, the parameters are

$$\begin{cases} \frac{1}{g+h} = u = 0.07968 \\ \ln(A_a^0/A_d^0) = v = -23.74 \\ \frac{E_a^0 - E_d^0}{R} = w = -7.593 \end{cases} \quad (\text{D.21})$$

(b) Now for the steady state rate data, $r_{ss} = k_d^0 \left[(k_a^0/k_d^0)(O_3) \right]^{\frac{h}{g+h}}$. So

$$\ln(r_{ss}) = \ln k_d^0 + \frac{h}{g+h} \left[\ln(k_a^0/k_d^0) + \ln(P_{O_3}) \right] \quad (\text{D.22})$$

Since it is known that $\frac{1}{g+h} = 0.07968$, and

$$\ln(k_a^0/k_d^0) = \ln(A_a^0/A_d^0) - \frac{(E_a^0 - E_d^0)}{RT} = -23.74 - 7.593/T \quad (\text{D.23})$$

So

$$\Delta = \sum_{i=1}^n \left\{ \ln(r_i) - \left[(\ln A_d^0 - E_d^0/RT) + 0.07968h(-23.74 - 7.593/T_i + \ln P_i) \right] \right\}^2 \quad (\text{D.24})$$

$$\Delta = \sum_{i=1}^n \left\{ \ln(r_i) - \left[(\ln A_d^0 - 1.892h) + (-E_d^0/R - 0.605h)(1/T_i) + (0.07968h) \ln P_i \right] \right\}^2 \quad (\text{D.25})$$

Let

$$\begin{cases} a = \ln A_d^0 - 1.892h \\ b = -E_d^0/R - 0.605h \\ c = 0.07968h \end{cases} \quad (D.26)$$

Thus

$$\Delta = \sum_{i=1}^n \left\{ \ln(r_i) - [a + b(1/T_i) + c \ln P_i] \right\}^2 \quad (D.27)$$

Let $1/T_i = x_i$, and $\ln(P_i) = y_i$, we get

$$\Delta = \sum_{i=1}^n \left\{ \ln(r_i) - [a + bx_i + cy_i] \right\}^2 \quad (D.28)$$

$$\text{For the least square fit, } \frac{\partial \Delta}{\partial a} = \frac{\partial \Delta}{\partial b} = \frac{\partial \Delta}{\partial c} = 0 \quad (D.29)$$

$$\frac{\partial \Delta}{\partial a} = 0 \Rightarrow \sum_{i=1}^n (\ln r_i - a - bx_i - cy_i) = 0 \quad (D.30)$$

$$\sum_{i=1}^n \ln r_i - na - b \sum_{i=1}^n x_i - c \sum_{i=1}^n y_i = 0 \quad (D.31)$$

$$\frac{\partial \Delta}{\partial b} = 0 \Rightarrow \sum_{i=1}^n [(\ln r_i - a - bx_i - cy_i)(-x_i)] = 0 \quad (D.32)$$

$$\sum_{i=1}^n (x_i \ln r_i) - a \sum_{i=1}^n x_i - b \sum_{i=1}^n x_i^2 - c \sum_{i=1}^n (x_i y_i) = 0 \quad (D.33)$$

$$\frac{\partial \Delta}{\partial c} = 0 \Rightarrow \sum_{i=1}^n [(\ln r_i - a - bx_i - cy_i)(-y_i)] = 0 \quad (D.34)$$

$$\sum_{i=1}^n (y_i \ln r_i) - a \sum_{i=1}^n y_i - b \sum_{i=1}^n (x_i y_i) - c \sum_{i=1}^n y_i^2 = 0 \quad (D.35)$$

From the data set, the following is obtained:

$$\sum_{i=1}^n x_i = 107.31 \quad \sum_{i=1}^n x_i^2 = 350.85 \quad \sum_{i=1}^n \ln r_i = -33.23$$

$$\sum_{i=1}^n y_i = 190.01 \quad \sum_{i=1}^n y_i^2 = 1179.8 \quad \sum_{i=1}^n x_i y_i = 61.96$$

$$\sum_{i=1}^n x_i \ln r_i = -109.40 \quad \sum_{i=1}^n y_i \ln r_i = -104.72$$

The result is

$$\begin{cases} 33a + 107.31b + 190.01c = -33.23 \\ 107.31a + 350.85b + 617.96 = -109.40 \\ 191.01a + 617.96b + 1179.8c = -104.72 \end{cases} \quad (\text{D.36})$$

Solving (Eq. 19)

$$\begin{cases} a = -4.385 \\ b = -0.7510 \\ c = 0.940 \end{cases} \quad (\text{D.37})$$

Substituting h , A_d^0 , and E_d^0 back into a , b , and c (Eq.26),

$$\begin{cases} h = 0.75 \\ A_d^0/s^{-1} = 1.6 \times 10^7 \\ E_d^0/kJmol^{-1} = 69.0 \end{cases} \quad (\text{D.38})$$

Combining (Eq. 36) with (Eq. 21), the final result is:

$$\begin{cases} g = 11.8 \\ A_a^0/cm^3 s^{-1} = 3.1 \times 10^{-18} \\ E_a^0/kJmol^{-1} = 6.2 \end{cases} \quad (\text{D.39})$$

APPENDIX E. KINETIC DATA FOR ETHANOL OXIDATION USING OZONE

Data Set For Figures 4.3 – 4.6, 4.9 and 4.10

Effect of Ethanol Partial Pressure				Inlet O ₃ Conc.=48.1 g/m ³			
Ethanol=0.24cc/h				Ethanol=0.34cc/h			
Temp/K	CO	CO ₂	C ₂ H ₅ OH	Temp/K	CO	CO ₂	C ₂ H ₅ OH
363	4.24	5.53	35.36	363	4.8	8.92	74.7
393	6.54	4.22	27.93	393	6.76	9.88	80.98
423	11.22	5.91	31.86	423	11.09	9.58	70.16
453	16.83	2.58	22.45	453	15.71	6.93	62.62
Concentrations/ molm ⁻³				Concentrations/ molm ⁻³			
Temp/K	CO	CO ₂	C ₂ H ₅ OH	Temp/K	CO	CO ₂	C ₂ H ₅ OH
363	0.030104	0.035945	0.173264	363	0.03408	0.05798	0.36603
393	0.046434	0.02743	0.136857	393	0.047996	0.06422	0.396802
423	0.079662	0.038415	0.156114	423	0.078739	0.06227	0.343784
453	0.119493	0.01677	0.110005	453	0.111541	0.045045	0.306838
Conversion and Selectivities%				Conversion and Selectivities%			
Temp/K	Conv%	Sel% CO	Sel% CO ₂	Temp/K	Conv%	Sel% CO	Sel% CO ₂
363	16.00889	45.57828	54.42172	363	11.1707	37.01934	62.98066
393	21.25106	62.86418	37.13582	393	12.38833	42.77108	57.22892
423	27.4403	67.46614	32.53386	423	17.01821	55.8397	44.1603
453	38.24679	87.69292	12.30708	453	20.32893	71.23306	28.76694
Rate/s ⁻¹				Rate/s ⁻¹			
Temp/K	CO	CO ₂	Total	Temp/K	CO	CO ₂	Total
363	0.005966	0.007123	0.013089	363	0.004812	0.008186	0.012997

393	0.010923	0.006452	0.017375		393	0.006165	0.008249	0.014414
423	0.015136	0.007299	0.022435		423	0.011057	0.008744	0.019801
453	0.027422	0.003849	0.031271		453	0.016849	0.006804	0.023653
Ethanol=0.51cc/h					Ethanol=0.69cc/h			
Temp/K	CO	CO2	C2H5OH		Temp/K	CO	CO2	C2H5OH
363	4.33	12.75	107.37		363	4.09	17.65	139.72
393	6.94	11.93	100.67		393	6.68	17.99	155.32
423	9.85	14.24	107.75		423	9.57	20.74	159.32
453	14.2	12.36	89.65		453	13.45	20.3	146.85
	Concentrations/ molm⁻³				Concentrations/ molm⁻³			
Temp/K	CO	CO2	C2H5OH		Temp/K	CO	CO2	C2H5OH
363	0.030743	0.082875	0.526113		363	0.029039	0.114725	0.684628
393	0.049274	0.077545	0.493283		393	0.047428	0.116935	0.761068
423	0.069935	0.09256	0.527975		423	0.067947	0.13481	0.780668
453	0.10082	0.08034	0.439285		453	0.095495	0.13195	0.719565
	Conversion and Selectivities%				Conversion and Selectivities%			
Temp/K	Conv%	Sel% CO	Sel% CO2		Temp/K	Conv%	Sel% CO	Sel% CO2
363	9.745558	27.05821	72.94179		363	9.501791	20.19908	79.80092
393	11.3904	38.8538	61.1462		393	9.745811	28.85564	71.14436
423	13.33626	43.03825	56.96175		423	11.49356	33.51154	66.48846
453	17.09492	55.65246	44.34754		453	13.64745	41.98597	58.01403
	Rate/s⁻¹				Rate/s⁻¹			
Temp/K	CO	CO2	Total		Temp/K	CO	CO2	Total
363	0.004594	0.012384	0.016978		363	0.004527	0.017883	0.02241
393	0.00771	0.012134	0.019844		393	0.006633	0.016353	0.022985
423	0.009999	0.013234	0.023234		423	0.009084	0.018023	0.027107

453	0.016574	0.013207	0.029782		453	0.013514	0.018673	0.032187
Effect of Ozone Partial Pressure					Ethanol Injection Rate=.34 cc/h			
Inlet O3 Conc.=11.9 g/m3					Inlet O3 Conc.=22.9 g/m3			
Temp/K	CO	CO2	C2H5OH		Temp/K	CO	CO2	C2H5OH
363	1.3	6.08	79.39		363	2.31	7.02	74.66
393	1.48	3.26	58.6		393	3	6	58.25
423	2.46	5.36	83.46		423	4.33	6.17	77.38
453	6.18	5.95	65.7		453	7.28	6.14	74.63
	Concentrations/ molm⁻³					Concentrations/ molm⁻³		
Temp/K	CO	CO2	C2H5OH		Temp/K	CO	CO2	C2H5OH
363	0.00923	0.03952	0.389011		363	0.016401	0.04563	0.365834
393	0.010508	0.02119	0.28714		393	0.0213	0.039	0.285425
423	0.017466	0.03484	0.408954		423	0.030743	0.040105	0.379162
453	0.043878	0.038675	0.32193		453	0.051688	0.03991	0.365687
	Conversion and Selectivities%					Conversion and Selectivities%		
Temp/K	Conv%	Sel% CO	Sel% CO2		Temp/K	Conv%	Sel% CO	Sel% CO2
363	5.896426	18.93333	81.06667		363	7.815431	26.44001	73.55999
393	5.230883	33.15036	66.84964		393	9.553989	35.32338	64.67662
423	6.010705	33.39196	66.60804		423	8.544427	43.3929	56.6071
453	11.36447	53.15131	46.84869		453	11.13015	56.42918	43.57082
	Rate/s⁻¹					Rate/s⁻¹		
Temp/K	CO	CO2	Total		Temp/K	CO	CO2	Total
363	0.001299	0.005562	0.006861		363	0.002404	0.006689	0.009093
393	0.002018	0.004069	0.006086		393	0.003927	0.00719	0.011116
423	0.002335	0.004658	0.006994		423	0.004314	0.005628	0.009942
453	0.007028	0.006195	0.013223		453	0.007308	0.005642	0.01295

Inlet O3 Conc.=40.0 g/m3				Inlet O3 Conc.=48.1 g/m3			
Temp/K	CO	CO2	C2H5OH	Temp/K	CO	CO2	C2H5OH
363	4.1	9.61	82.02	363	4.8	8.92	74.7
393	6.04	11.61	76.28	393	6.76	9.88	80.98
423	10.26	10.86	66.98	423	11.09	9.58	70.16
453	14.45	10.78	61.9	453	15.71	6.93	62.62
Concentrations/ molm ⁻³				Concentrations/ molm ⁻³			
Temp/K	CO	CO2	C2H5OH	Temp/K	CO	CO2	C2H5OH
363	0.02911	0.062465	0.401898	363	0.03408	0.05798	0.36603
393	0.042884	0.075465	0.373772	393	0.047996	0.06422	0.396802
423	0.072846	0.07059	0.328202	423	0.078739	0.06227	0.343784
453	0.102595	0.07007	0.30331	453	0.111541	0.045045	0.306838
Conversion and Selectivities%				Conversion and Selectivities%			
Temp/K	Conv%	Sel% CO	Sel% CO2	Temp/K	Conv%	Sel% CO	Sel% CO2
363	10.2276	31.78815	68.21185	363	11.1707	37.01934	62.98066
393	13.66786	36.2352	63.7648	393	12.38833	42.77108	57.22892
423	17.93309	50.78641	49.21359	423	17.01821	55.8397	44.1603
453	22.15685	59.41853	40.58147	453	20.32893	71.23306	28.76694
Rate/s ⁻¹				Rate/s ⁻¹			
Temp/K	CO	CO2	Total	Temp/K	CO	CO2	Total
363	0.003783	0.008117	0.0119	363	0.004812	0.008186	0.012997
393	0.005762	0.01014	0.015903	393	0.006165	0.008249	0.014414
423	0.010597	0.010269	0.020866	423	0.011057	0.008744	0.019801
453	0.015318	0.010462	0.02578	453	0.016849	0.006804	0.023653

APPENDIX F. LEAST SQUARE FITTING OF ETHANOL OXIDATION KINETIC DATA

This appendix describes the procedure and calculation details of least square fitting of the ethanol oxidation kinetic data to a power law equation.

F.1. FITTING PROCEDURE

$$\text{Rate of ethanol conversion, } r = kC_{O_3}^\alpha C_{C_2H_5OH}^\beta = A \exp\left(-\frac{E}{RT}\right) C_{O_3}^\alpha C_{C_2H_5OH}^\beta \quad (F.1)$$

$$\text{So } \ln r = \ln A - \frac{E}{RT} + \alpha \ln C_{O_3} + \beta \ln C_{C_2H_5OH} \quad (F.2)$$

$$\text{Let } \Delta = \sum_i^N \left[\ln r_i - \left(\ln A - \frac{E}{RT_i} + \alpha \ln C_{O_3}^i + \beta \ln C_{C_2H_5OH}^i \right) \right]^2 \quad (F.3)$$

Here A, E, α , and β are variables, and N is the total number of kinetic data points.

$$\left\{ \begin{array}{l} \frac{\partial \Delta}{\partial A} = \sum_i^N \left[\left(\ln r_i - \ln A + \frac{E}{RT_i} - \alpha \ln C_{O_3}^i - \beta \ln C_{C_2H_5OH}^i \right) \frac{1}{A} \right] = 0 \\ \frac{\partial \Delta}{\partial E} = \sum_i^N \left[\left(\ln r_i - \ln A + \frac{E}{RT_i} - \alpha \ln C_{O_3}^i - \beta \ln C_{C_2H_5OH}^i \right) \frac{1}{RT_i} \right] = 0 \\ \frac{\partial \Delta}{\partial \alpha} = \sum_i^N \left[\left(\ln r_i - \ln A + \frac{E}{RT_i} - \alpha \ln C_{O_3}^i - \beta \ln C_{C_2H_5OH}^i \right) \left(\ln C_{O_3}^i \right) \right] = 0 \\ \frac{\partial \Delta}{\partial \beta} = \sum_i^N \left[\left(\ln r_i - \ln A + \frac{E}{RT_i} - \alpha \ln C_{O_3}^i - \beta \ln C_{C_2H_5OH}^i \right) \left(\ln C_{C_2H_5OH}^i \right) \right] = 0 \end{array} \right. \quad (F.4)$$

So

$$\left\{ \begin{array}{l}
\sum_i^N \ln r_i - N \ln A + \frac{E}{R} \sum_i^N \left(\frac{1}{T_i} \right) - \alpha \sum_i^N \ln C_{O_3}^i - \beta \sum_i^N \ln C_{EtOH}^i = 0 \\
\sum_i^N \left(\frac{\ln r_i}{T_i} \right) - \ln A \sum_i^N \left(\frac{1}{T_i} \right) + \frac{E}{R} \sum_i^N \left(\frac{1}{T_i^2} \right) - \alpha \sum_i^N \left(\frac{\ln C_{O_3}^i}{T_i} \right) - \beta \sum_i^N \left(\frac{\ln C_{EtOH}^i}{T_i} \right) = 0 \\
\sum_i^N (\ln r_i \ln C_{O_3}^i) - \ln A \sum_i^N (\ln C_{O_3}^i) + \frac{E}{R} \sum_i^N \left(\frac{\ln C_{O_3}^i}{T_i} \right) - \alpha \sum_i^N (\ln C_{O_3}^i)^2 - \beta \sum_i^N (\ln C_{O_3}^i \ln C_{EtOH}^i) = 0 \\
\ln r_i \sum_i^N (\ln C_{EtOH}^i) - \ln A \sum_i^N (\ln C_{EtOH}^i) + \frac{E}{R} \sum_i^N \left(\frac{\ln C_{EtOH}^i}{T_i} \right) - \alpha \sum_i^N (\ln C_{O_3}^i \ln C_{EtOH}^i) - \beta \sum_i^N (\ln C_{EtOH}^i)^2 = 0
\end{array} \right. \quad (F.5)$$

Substituting all the terms (see attached Table F.1.),

$$\left\{ \begin{array}{l}
54.24a + 25.62b - 28c + 0.0691d - 115.4 = 0 \\
13.38a + 6.32b - 6.91c + 0.0172d - 28.68 = 0 \\
112.06a + 50.6b - 54.24c + 0.1338d - 230.45 = 0 \\
50.6a + 26.3b - 25.62c + 0.0632d - 108.72 = 0
\end{array} \right. \quad (F.6)$$

Solving (F.6)

$$\left\{ \begin{array}{l}
\alpha = 0.89 \\
\beta = 0.81 \\
\ln A = 1.826 \\
\frac{E}{R} = 1414.5
\end{array} \right. \quad (F.7)$$

$$\text{So the rate can be expressed as: } r = 6.2 \exp\left(-\frac{11.8 \text{kJ mol}^{-1}}{RT}\right) C_{O_3}^{0.89} C_{C_2H_5OH}^{0.81} \quad (F.8)$$

Table F.1. Calculation Details for the Least Square Fitting of the Ethanol Oxidation Kinetic Data.

$$C_1 = C_{O_3}; C_2 = C_{C_2H_5OH}$$

T/K	C ₁ /molm ⁻³	C ₂ /molm ⁻³	r/s-1	10 ³ /T	ln(C ₁)	ln(C ₂)	lnr	ln(C ₁)lnr
363	0.20	0.36	0.0130	2.7548	-1.6094	-1.0217	-4.3428	6.989
393	0.20	0.36	0.0144	2.5445	-1.6094	-1.0217	-4.2405	6.825
423	0.20	0.36	0.0198	2.3641	-1.6094	-1.0217	-3.9221	6.312
453	0.20	0.36	0.0237	2.2075	-1.6094	-1.0217	-3.7423	6.023
363	0.20	0.54	0.0170	2.7548	-1.6094	-0.6162	-4.0745	6.558
393	0.20	0.54	0.0198	2.5445	-1.6094	-0.6162	-3.9221	6.312
423	0.20	0.54	0.0232	2.3641	-1.6094	-0.6162	-3.7636	6.057
453	0.20	0.54	0.0298	2.2075	-1.6094	-0.6162	-3.5132	5.654
363	0.20	0.73	0.0224	2.7548	-1.6094	-0.3147	-3.7987	6.114
393	0.20	0.73	0.0230	2.5445	-1.6094	-0.3147	-3.7723	6.071
423	0.20	0.73	0.0271	2.3641	-1.6094	-0.3147	-3.6082	5.807
453	0.20	0.73	0.0322	2.2075	-1.6094	-0.3147	-1.1332	1.824
363	0.20	0.25	0.0131	2.7548	-1.6094	-1.3863	-4.3351	6.977
393	0.20	0.25	0.0174	2.5445	-1.6094	-1.3863	-4.0513	6.520
423	0.20	0.25	0.0224	2.3641	-1.6094	-1.3863	-3.7987	6.114
453	0.20	0.25	0.0313	2.2075	-1.6094	-1.3863	-3.4641	5.575
363	0.05	0.36	0.00686	2.7548	-2.9957	-1.0217	-4.982	14.925
393	0.05	0.36	0.00609	2.5445	-2.9957	-1.0217	-5.1011	15.282
423	0.05	0.36	0.00699	2.3641	-2.9957	-1.0217	-4.9633	14.869
453	0.05	0.36	0.0132	2.2075	-2.9957	-1.0217	-4.3275	12.964
363	0.095	0.36	0.00909	2.7548	-2.3539	-1.0217	-4.7006	11.065
393	0.095	0.36	0.0111	2.5445	-2.3539	-1.0217	-6.8034	16.014
423	0.095	0.36	0.00994	2.3641	-2.3539	-1.0217	-4.6112	10.854
453	0.095	0.36	0.0130	2.2075	-2.3539	-1.0217	-4.3428	10.222
363	0.17	0.36	0.0119	2.7548	-1.772	-1.0217	-4.4312	7.852
393	0.17	0.36	0.0159	2.5445	-1.772	-1.0217	-4.1414	7.338
423	0.17	0.36	0.0209	2.3641	-1.772	-1.0217	-3.868	6.854
453	0.17	0.36	0.0258	2.2075	-1.772	-1.0217	-3.6574	6.481
				69.0965	-54.237	-25.6152	-115.41	230.454

$\ln(C_2)\ln r$	$(\ln(C_1))^2$	$(\ln(C_2))^2$	$\ln(C_1)\ln(C_2)$	$(\ln r)^2$	$\ln(C_1)/T$	$\ln(C_2)/T$	$\ln r/T$	$(10^3/T)^2$
4.437	2.5903	1.044	1.6443	18.8600	-0.00443	-0.00281	-0.01196	7.5890
4.332	2.5903	1.044	1.6443	17.9821	-0.00410	-0.00260	-0.01079	6.4746
4.007	2.5903	1.044	1.6443	15.3827	-0.00380	-0.00242	-0.00927	5.5888
3.823	2.5903	1.044	1.6443	14.0047	-0.00355	-0.00226	-0.00826	4.8731
2.511	2.5903	0.380	0.9917	16.6019	-0.00443	-0.00170	-0.01122	7.5890
2.417	2.5903	0.380	0.9917	15.3827	-0.00410	-0.00157	-0.00998	6.4746
2.319	2.5903	0.380	0.9917	14.1647	-0.00380	-0.00146	-0.00890	5.5888
2.165	2.5903	0.380	0.9917	12.3429	-0.00355	-0.00136	-0.00776	4.8731
1.195	2.5903	0.099	0.5065	14.4301	-0.00443	-0.00087	-0.01046	7.5890
1.187	2.5903	0.099	0.5065	14.2300	-0.00410	-0.00080	-0.00960	6.4746
1.136	2.5903	0.099	0.5065	13.0193	-0.00380	-0.00074	-0.00853	5.5888
0.357	2.5903	0.099	0.5065	1.28415	-0.00355	-0.00069	-0.00250	4.8731
6.010	2.5903	1.922	2.2312	18.7935	-0.00443	-0.00382	-0.01194	7.5890
5.616	2.5903	1.922	2.2312	16.4129	-0.00410	-0.00353	-0.01031	6.4746
5.266	2.5903	1.922	2.2312	14.4301	-0.00380	-0.00328	-0.00898	5.5888
4.802	2.5903	1.922	2.2312	12.0002	-0.00355	-0.00306	-0.00765	4.8731
5.090	8.9744	1.044	3.0606	24.8208	-0.00825	-0.00281	-0.01372	7.5890
5.212	8.9744	1.044	3.0606	26.0213	-0.00762	-0.00260	-0.01298	6.4746
5.071	8.9744	1.044	3.0606	24.6341	-0.00708	-0.00242	-0.01173	5.5888
4.421	8.9744	1.044	3.0606	18.7276	-0.00661	-0.00226	-0.00955	4.8731
4.802	5.5407	1.044	2.4048	22.0955	-0.00648	-0.00281	-0.01295	7.5890
6.951	5.5407	1.044	2.4048	46.2862	-0.00599	-0.00260	-0.01731	6.4746
4.711	5.5407	1.044	2.4048	21.2631	-0.00556	-0.00242	-0.01090	5.5888
4.437	5.5407	1.044	2.4048	18.8600	-0.00520	-0.00226	-0.00959	4.8731
4.527	3.1398	1.044	1.8103	19.6357	-0.00488	-0.00281	-0.01221	7.5890
4.231	3.1398	1.044	1.8103	17.1515	-0.00451	-0.00260	-0.01054	6.4746
3.952	3.1398	1.044	1.8103	14.9615	-0.00419	-0.00242	-0.00914	5.5888
3.737	3.1398	1.044	1.8103	13.3764	-0.00391	-0.00226	-0.00807	4.8731
108.721	112.06	26.303	50.5977	497.155	-0.13384	-0.06321	-0.2868	171.7

Appendix G. Error Analysis

This section estimates the errors involved in the measurements during ozone decomposition. An example data set (See Table G1) was used to carry out the calculations. The relative standard deviation was calculated using the following equation:

$$\Delta = \frac{1}{N} \sum_{i=1}^N \sqrt{\left[\frac{(A - \bar{A})^2}{\bar{A}^2} \right]} \quad (\text{G.1})$$

Here N is the total number of data points, A is the raw data value and \bar{A} is the average value of the data point.

Table G.1. An example Data Set for Ozone Decomposition (WL02057)

Temperature / °C = 7.8, 7.9, 8.5, 9.0, 8.7, 8.7		
Peak Area	Initial O ₃ Conc. / g m ⁻³	Final O ₃ Conc. / g m ⁻³
16909, 17798	0.4, 0.4, 0.3, 0.4, 0.3, 0.4, 0.4, 0.4	0.3, 0.3, 0.3, 0.3, 0.3, 0.3
18943, 18507, 19641, 19087	0.9, 1.0, 1.0, 1.0, 1.0, 0.9, 1.0, 0.9	0.8, 0.8, 0.9, 0.8, 0.9, 0.8, 0.8, 0.9
25807, 25156, 25255	19.9, 19.5, 20.9, 19.4, 18.8, 19.5, 20.6, 19.4, 18.9, 19.6, 19.9, 21.0	17.1, 16.6, 16.7, 16.8, 16.9, 17.1, 17.5, 17.4, 17.2, 16.7, 16.7, 17.3
30810, 29559, 29111	31.2, 31.5, 31.0, 32.2, 31.5, 31.1, 31.3, 32.1	28.0, 28.0, 27.9, 27.5, 27.7, 27.5, 27.3, 27.3
32348, 31421, 33059	39.8, 39.3, 40.3, 40.5, 40.4, 39.6, 40.3, 39.8	34.9, 35.1, 35.0, 35.1, 35.1, 35.2, 34.8, 35.0, 34.9, 34.7
32229, 33981, 32080	45.0, 44.5, 44.1, 44.2, 44.6, 44.4, 44.4, 44.3, 44.7, 44.4, 44.6, 44.2	38.7, 38.6, 38.5, 38.7, 38.6, 38.7, 38.4, 38.6

RESULTS

For temperature measurements, the error was calculated as: $\Delta = 4.6 \%$.

For the measurements of the peak area, the error was calculated to be varying from 0.5 % to 5 %.

For the measurements of the reaction rate, the error was estimated to be from 1 % to 4 %.

So, in summary the error involved in this work is generally less than 5 %.

VITA

Wei Li was born on October 2nd, 1966 in Hangzhou, China. He graduated from The University of Science and Technology of China, Hefei, in 1988 with a Bachelor Degree of Sciences in Chemical Physics. Afterwards he went to Dalian, China, to work as a research associate at the State Key Laboratory of Catalysis, Dalian Institute of Chemical Physics. His research interest was in the kinetics and mechanism of the methane oxidative coupling reaction. Between 1991-1992, he was a visiting scholar at University of Hull, England, working on the application of microwave in the methane oxidative coupling reaction. In 1993 he joined Indiana University at Bloomington as a Ph. D. student in Department of Chemistry. His research work involved preparation of alkoxide precursors for chemical vapor deposition of high-temperature superconductors. In 1994 he transferred to Virginia Polytechnic Institute and State University to peruse a Doctorate of Philosophy in Materials Engineering and Science under the guidance of Dr. S. Ted Oyama in the Chemical Engineering Department. His dissertation deals with the kinetics and mechanism of ozone decomposition and ozone oxidation of ethanol on manganese oxide catalysts. This dissertation completes the requirements for his Ph. D. degree and he is expected to graduate May of 1998 from Virginia Polytechnic Institute and State University.